On single-crystal solid-state NMR based quantum information processing.

by

Osama Moussa

A thesis
presented to the University of Waterloo
in fulfillment of the
thesis requirement for the degree of
Doctor of Philosophy
in
Physics

Waterloo, Ontario, Canada, 2010

I hereby declare that I am the sole author of this thesis. This is a true copy of the thesis, including any required final revisions, as accepted by my examiners.

Osama Moussa

I understand that my thesis may be made electronically available to the public.

Osama Moussa

Abstract

Quantum information processing devices promise to solve some problems more efficiently than their classical counterparts. The source of the speedup is the structure of quantum theory itself. In that sense, the physical units that are the building blocks of such devices are its power. The quest then is to find or manufacture a system that behaves according to quantum theory, and yet is controllable in such a way that the desired algorithms can be implemented. Candidate systems are benchmarked against general criteria to evaluate their success. In this thesis, I advance a particular system and present the progress made towards each of these criteria. The system is a three-qubit ^{13}C solid-state nuclear magnetic resonance (NMR) based quantum processor. I report results concerning system characterization and control, pseudopure state preparation, and quantum error correction. I also report on using the system to test a central question in the foundation of quantum mechanics.

Acknowledgements

I am indebted to my parents, Mahmoud and Thoraia, for everything.

I bear much gratitude to Dr. Raymond Laflamme, for giving me the opportunity to be part of the Institute for Quantum Computing, for his timely and insightful comments, and for his constant support in scientific endeavors and otherwise.

I must thank the members of my advisory committee; Dr. Joseph Emerson, Dr. Frank Wilhelm, and Dr. William Powers for their interest in my research and for their support; and Dr. Lieven Vandersypen for agreeing to be on the defense committee. In addition, I would like to thank the unofficial members of the advisory committee; Dr. Jonathan Baugh for sharing his NMR knowledge, and for providing a live example of a great experimentalist; and Dr. David Cory for the creativity-laden interactions and unwavering encouragement.

In addition, I have had the fortune to collaborate with many good people. I am appreciative of having had Dr. Colm Ryan, Dr. Martin Laforest, Dr. Marcus Silva, and Gina Passante as comrades throughout this journey.

I am thankful to everyone at the IQC, faculty, staff, and students, who have made my experience a very pleasant and rich one. I am grateful for the financial support from the Natural Sciences and Engineering Council of Canada, which was timely and instrumental.

I must acknowledge my siblings–Muhammad, Omar, Asmaa, and Lina–and the little ones–Noah, Ayah, and Jude– for they are my inspiration.

Last, but not least, I would like to thank my good friends, Marcus, Moro, and Esseily, for the comradeship, the constant support, and the endless stimulating conversations; Gina, for seeing me through.

To those moments, few and far between, that make making science worthwhile.

Contents

List of Tables

List of Figures

Chapter 1

Introduction

1.1 Quantum Information Processing

Information processing devices that operate based on the laws of quantum physics are believed to be more powerful than their classical couterparts, in the sense that they can solve certain important problems –such as simulation of quantum systems [Fey82] and factoring of large numbers [Sho94]– more efficiently; that is to say without incurring an overhead in resources such as time or ancillary registers that grows unfavorably with the size of the problem. There has been much discussion about the source of this speed up. It has been quite often attributed to entanglement, or more generally to quantum correlations present in some special quantum states. It has also been argued that quantum dynamics [LCNV01] plays an important role. Whatever it may be, it is quite obvious that it is due to the particular mathematical structure of the underlying physical theory. The quest, then, is to build such a device from blocks that verifiably behave according to this structure.

1.2 The Physical Implementation of Quantum Computation

The heading of this section is adopted from the title of a paper by DiVincenzo [DiV00], in which he discusses, what are now, a widely accepted set of basic criteria for the physical implementation for quantum computation. These are recognized as the following 5 requirements:

- A scalable physical system with well characterized qubits.

- The ability to initialize the state of the qubits to a simple fiducial state, such as the ground state of some Hamiltonian.
- Long relevant decoherence times, much longer than the gate operation time.
- A universal set of quantum gates.
- A qubit-specific measurement capability.

Many systems have shown great strides in the quest for satisfying these criteria, and many more have been proposed. Liquid state nuclear magnetic resonance (NMR) for quantum information processing was introduced in [CFH97, GC97, CPH98, CLK+00], and has arguably been one of the most successful paradigms to date: with experiments implementing Deutsch's problem [JM98, CVZ+98, LBF98]; the Quantum Fourier Transform [WLC01]; Shor's factoring algorithm [VSB+01]; Quantum clock synchronization algorithm [ZLD+04]; Quantum search [ZLSD02]; Quantum walk [RLBL05]; quantum error correcting protocols [CPM+98, LVZ+99, SCS+00, KLMN01, BVFC05, LSB+07]; simulation of quantum systems [STH+99, TSS+00, NSO+05, CYC06]; and the largest demonstrated quantum processor with 12 qubits [NMR+06]. For detailed discussion of the techniques and results to date, see [CLK+00, LKC+02, VC05, BCC+07]

In this thesis, I present progress made towards the realization of a single crystal soild-state NMR based quantum information processor. The distinguishing features of a solid-state NMR system include:

- Higher couplings leading to faster multiqubit gates.
- Dynamic nuclear polarization can lead to highly purified quantum states.
- Long intrinsic decoherence times.
- Fast relaxing spin baths in the form of dipolar networks to facilitate a fresh supply of ancillas for quantum error correction.

This thesis is primarily about the experimental work; about importing and improving some of the tools developed elsewhere and applying them in a new paradigm.

Chapter 2

System characterization and control

2.1 Nuclear spins

The archetypal qubit is a spin-$\frac{1}{2}$ particle in a magnetic field. Spin-$\frac{1}{2}$ nuclear spins have been sought after because of their long coherence times, and relative insensitivity to the environment.

2.2 Malonic acid

In this work, we investigate an intermediate step towards the realization of the solid-state QIP proposed by Cory *et. al.* [CLK+00]. The system is a macroscopic single crystal of Malonic Acid, $C_3H_4O_4$ (shown in Figure 2.1), grown from aqueous solution. The unit cell contains two molecules related by an inversion symmetry, and are therefore magnetically equivalent. A small fraction (typically $\sim 1\% - 3\%$) of the molecules are triply labeled with ^{13}C to form an ensemble of processor molecules diluted in a computationally inert matrix of isotopomers of the same molecule. During computation, these processors are typically decoupled from the 100% abundant protons in the crystal. Natural abundance ^{13}C are present in the sample at a rate of $\sim 1\%$, and their contribution to the signal is easily identifiable and, if desired, can be eliminated. The fraction of molecules with two ^{13}C nuclei would be even less at $(1\%)^2$, and are therefore negligible.

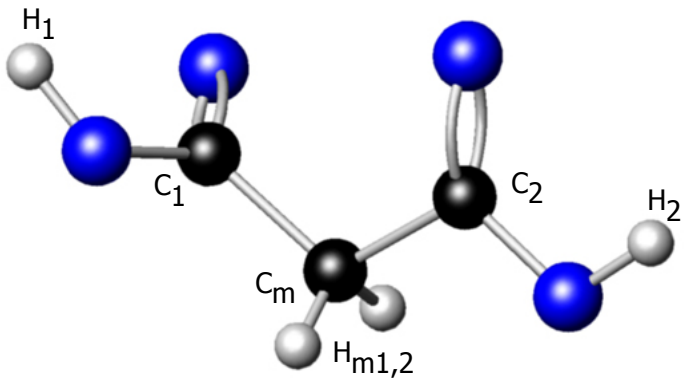

Figure 2.1: Schematic of the Malonic acid ($C_3H_4O_4$) molecule. The black spheres represent Carbon nuclei; the blue, Oxygen; and white, Hydrogen. The plane of the methylene group is perpendicular to the plane of the Carbons, and so is the plane of one Carboxyl group, while the other Carboxyl group is approximately parallel.

2.3 NMR Hamiltonian

A nucleus with intrinsic (spin) angular momentum $\boldsymbol{S}$ will possess a magnetic dipole moment, $\boldsymbol{\mu}$, given by

$$\boldsymbol{\mu} = \gamma \boldsymbol{S}\,, \tag{2.1}$$

where γ is called the *gyromagnetic ratio*, and depends on the nuclear isotope (e.g. $\gamma_{^1\mathrm{H}} = 42.58$ MHz/T and $\gamma_{^{13}\mathrm{C}} = 10.71$ MHz/T). This nuclear magnetic dipole will interact with a given local magnetic field, $\boldsymbol{B}$, via the Hamiltonian,

$$\mathcal{H} = -\boldsymbol{\mu} \cdot \boldsymbol{B}, \tag{2.2}$$

producing an energy splitting between the two states corresponding to the moment being aligned and anti-aligned with the direction of the field (In a field of 7 T, this splitting will be on the order of 300MHz for ^{1}H and 75MHz for ^{13}C).

The total Hamiltonian of the system, then, becomes a matter of accounting for the various sources for magnetic fields, internal and external, that affect the nuclei.

2.3.1 External (control) Hamiltonian

NMR relies on a strong static magnetic field to establish[1] the dominant terms in the internal Hamiltonian, and an oscillating transverse field to excite/induce the transitions. The static field, $\boldsymbol{B}_0 = B_0\hat{z}$, is usually taken to define the z-axis of the laboratory frame of reference. The interaction of a nuclear spin and the static field is described by the Zeeman Hamiltonian (2.2),

$$\mathcal{H}_Z = -\gamma B_0 Z = -\omega_0 Z, \tag{2.3}$$

where Z denotes the pauli operator, σ_z. (Similarly, X and Y denote the pauli operators σ_x and σ_y)

The transverse field, $\boldsymbol{B}_1(t)$, can be written as the sum of two counter rotating fields in the lab frame:

$$\begin{aligned}\boldsymbol{B}_1(t) &= B_1 \cos(\omega_{rf} t + \phi)\hat{x} \\ &= \tfrac{1}{2} B_1 \exp\left[i(\omega_{rf} t + \phi)\right]\hat{x} + \tfrac{1}{2} B_1 \exp\left[-i(\omega_{rf} t + \phi)\right]\hat{x}\,,\end{aligned} \tag{2.4}$$

where ϕ is the time independent phase of the transverse field, B_1 its amplitude, and ω_{rf} its angular frequency, or the slope of the phase at time t. The two counter rotating fields are separated by twice ω_{rf} in frequency, thus counting one of them irrelevant for NMR. Thus, the Hamiltonian describing the interaction between a nuclear spin and the transverse field can be written as

$$\mathcal{H}_1(\omega_1, \omega_{rf}, \phi, t) = e^{-i(\omega_{rf}\ t+\phi)Z}\ \omega_1 X\ e^{i(\omega_{rf}\ t+\phi)Z}\,. \tag{2.5}$$

The experiments reported in this thesis were performed in a static field of 7.1T using a purpose-built probe, whose dual-resonance tank circuit is designed to resonate at 300MHz and 75MHz, the Larmour frequencies of ^{1}H and ^{13}C, respectively.

2.3.2 Internal (Natural) Hamiltonian

The internal spin Hamiltonian contains the following relevant contributions:

1. **Chemical shift:** The static external magnetic field, $\boldsymbol{B}_0$, induces currents in the molecular electron clouds, which in turn induce a secondary magnetic field at the nucleus site, partially shielding the nuclear spin from the external magnetic field. In molecules where the electron distribution is not spherically

[1] Terms in the Hamiltonian that do not commute with the dominant Zeeman term, and whose magnitude is small compared to the dominant interaction, are dropped – this is known as the secular approximation. See Appendix A.6 in [Lev01].

symmetric, the electron cloud in general is not free to precess about the direction of the external field. Hence, the induced local field at a certain nuclear spin in general is not parallel to the applied field [Vee84]. This anisotropic shielding causes an anisotropic shift, *the chemical shift*, of the resonance frequency of a nuclear spin of a solid. In general, the magnetic field felt by the nucleus can be written as

$$\boldsymbol{B} = \boldsymbol{B}_0 + \boldsymbol{\delta} \cdot \boldsymbol{B}_0 \,, \tag{2.6}$$

where $\boldsymbol{\delta}$ is a dimensionless, second rank tensor that determines the magnitude and direction of the shielding, and is known as the *chemical shielding tensor*. In the lab-frame, $\boldsymbol{\delta}$ is given by

$$\boldsymbol{\delta} = \begin{pmatrix} \delta_{xx} & \delta_{xy} & \delta_{xz} \\ \delta_{yx} & \delta_{yy} & \delta_{yz} \\ \delta_{zx} & \delta_{zy} & \delta_{zz} \end{pmatrix} \,, \tag{2.7}$$

where δ_{jk} is interpreted as the shielding in direction j given the magnetic field in direction k. The chemical shielding tensor can be written as a sum of a symmetric tensor and an antisymmetric one. The antisymmetric part has been shown to affect the NMR line positions only in the second order, and therefore can be neglected. This information can be encoded in a diagonal tensor in one special axis system, called the *principal axes system*, and a rotation $\mathcal{R}(\boldsymbol{\theta})$, which maps this principal axes system to the lab-frame; i.e.

$$\boldsymbol{\delta} = \mathcal{R}(\boldsymbol{\theta}) \cdot \begin{pmatrix} \delta_{11} & 0 & 0 \\ 0 & \delta_{22} & 0 \\ 0 & 0 & \delta_{33} \end{pmatrix} \cdot \mathcal{R}(\boldsymbol{\theta})^{-1} \,, \tag{2.8}$$

where $\boldsymbol{\theta}$ are the Euler angles parametrizing the rotation; and, by convention, $\delta_{11} \geq \delta_{22} \geq \delta_{33}$. The values of these three *principal values* depend on the location of the nucleus within the molecule, and, if they are not equal (which is generally the case), then the value of the chemical shift is dependent on the orientation of the magnetic field with respect to the principal axes system. In a single crystal solid, all unit cells are in the same orientation with respect to the external magnetic field, and hence, corresponding nuclei on the molecules in different unit cells have the same chemical shift – barring external field inhomogeneities.

The two carbons, C_1 and C_2, in the carboxyl groups of Malonic acid 2.1, have approximately the same principal values, as shown in Table 2.1, but the two principal axes systems are rotated relative to each other allowing for the possibility of different chemical shift values for C_1 and C_2 in the same magnetic field. Figure 2.2 shows that, in fact, that difference could take on any value from 0 up to 100 ppm (8kHz in 7T field) for some orientations.

	δ_{11}	δ_{22}	δ_{33}
C_1	244	179	108
C_m	62	50	18
C_2	248	174	111

Table 2.1: Principal chemical shift values for Malonic acid in ppm (TMS) [TFRH80, Vee84].

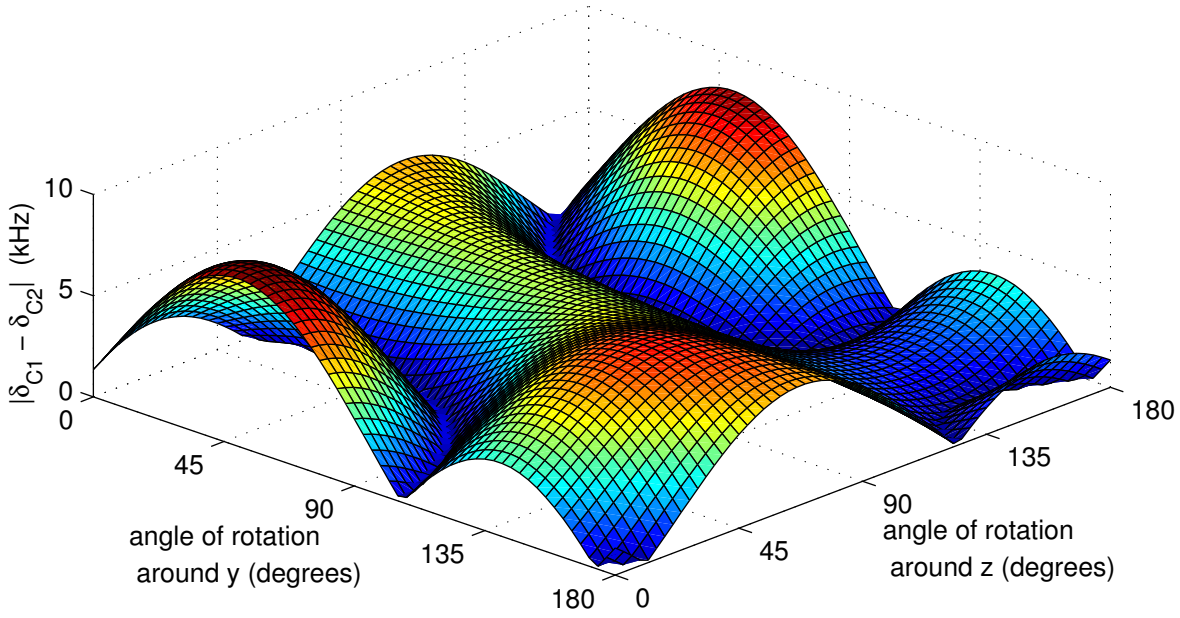

Figure 2.2: Variation of the chemical shift difference between the two Carboxyl Carbon nuclei, $|\delta_{C_1} - \delta_{C_2}|$, as a function of a composite rotation about two axes in the lab frame. The difference varies from zero to about 8kHz.

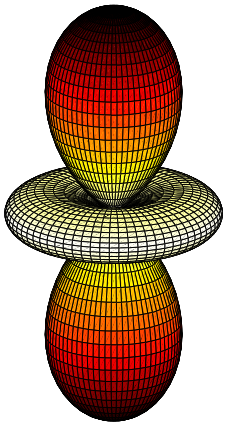

Figure 2.3: Spherical harmonic, $\mathrm{Y}_0^2(\theta, \phi)$; The angular dependance of the dipolar coupling.

2. **Direct dipole-dipole coupling:** This mutual through-space magnetic interaction between two nuclear magnetic moments can be understood as the magnetic moment of each spin interacting with the magnetic field caused at its site by the other. The form of this interaction, in the secular approximation, depends on whether the interacting spins, labeled i and j, belong to the same isotopic species (*homonuclear*), or not (*heteronuclear*), in the following way:

$$\text{Homonuclear:} \qquad \mathcal{H}_D = d_{ij}(2Z_iZ_j - X_iX_j - Y_iY_j)\,; \tag{2.9}$$

$$\text{Heteronuclear:} \qquad \mathcal{H}_D = d_{ij}\ 2Z_iZ_j\,, \tag{2.10}$$

where d_{ij} is the dipolar coupling constant, and is given by

$$d_{ij} = -\ \hbar\ \frac{\mu_0}{16\pi}\frac{\gamma_i\gamma_j}{r_{ij}^3}\frac{1}{2}(3\cos^2\theta_{ij} - 1)\,, \tag{2.11}$$

where μ_0 is the permeability of free space, the γs are the gyromagnetic ratios of the interacting spins, r_{ij} is the distance between them, and θ_{ij} is the angle between the external magnetic field and the vector connecting the two spins. Thus, the dipolar couplings are anisotropic, with angular dependance proportional to the zeroth degree second order spherical harmonic (shown in Figure 2.3). The *flip-flop* term in the homonuclear dipolar hamiltonian,

$$\begin{aligned} XX + YY &= \tfrac{1}{2}(\sigma_+ + \sigma_-)\tfrac{1}{2}(\sigma_+ + \sigma_-) + \tfrac{1}{2i}(\sigma_+ - \sigma_-)\tfrac{1}{2i}(\sigma_+ - \sigma_-) \\ &= \tfrac{1}{2}[\sigma_+\sigma_- + \sigma_-\sigma_+], \end{aligned} \tag{2.12}$$

renders the evolution more complex, and causes spin diffusion to dominate the dynamics.

3. **J-coupling** This electron mediated coupling is typically orders of magnitude weaker than the direct dipolar coupling, and is therefore typically ignored, but we found that including it in the description of the Hamiltonian provides more accurate estimates of the controls. There are two components to this coupling. First, an isotropic component with the form

$$\mathcal{H}_J = \pi J_{ij}(Z_iZ_j + X_iX_j + Y_iY_j)\,, \tag{2.13}$$

where J_{ij} is the isotropic, or scalar, J-coupling constant, and whose value can be measured in a straight forward manner from a liquid state experiment. There is also an anisotropic component to the J-coupling which is identical in form to the dipolar coupling, and is therefore absorbed in the dipolar coupling constant.

Using the above model, and the geometry of the molecule from X-ray [JRS94] and neutron scattering data [MK93] and chemical shift anisotropy [TFRH80, Vee84], one can map out the full intramolecular Hamiltonian as a function of orientation. We have developed a tool to quickly survey the possible Hamiltonians for a candidate system, or to quickly find an orientation with favourable properties for a particular experiment. This is presented in Appendix B.

However, for high-fidelity control, a precise intramolecular Hamiltonian for the homonuclear Carbon system is required. This is obtained by fitting a proton-decoupled ^{13}C spectrum – a process similar to that used in liquid state NMR, but is complicated by the presence of strong couplings which mix the eigenstates of the Zeeman Hamiltonian (so they are no longer good eigenstates – see Appendix A for details). A model Hamiltonian is constructed using an initial guess of the parameters,

$$\mathcal{H}_{lbl} = \sum_i -\omega_i Z_i + \sum_{j<i} d_{ij}(2Z_iZ_j - X_iX_j - Y_iY_j) + \sum_{j<i} \pi J_{ij}(Z_iZ_j + X_iX_j + Y_iY_j)\,, \tag{2.14}$$

and a free induction decay (FID) is computed for a state that contains equal amplitudes of all single coherences. Instead of simulating the full evolution, which is computationally expensive, only the contributions to the signal from the observable terms are tallied. In the eigenbasis of the Hamiltonian, the evolution is quite simple: each observable matrix element oscillates at a frequency equal to the difference

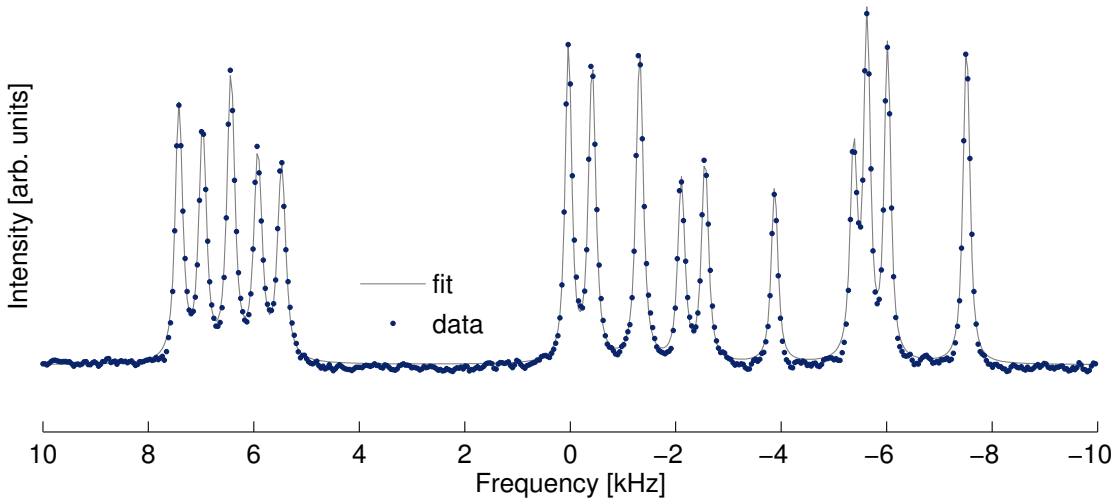

Figure 2.4: Real part of a proton-decoupled ^{13}C spectrum obtained (for some orientation of the crystal) after polarization transfer from the abundant protons in the crystal. The decoupling pulse sequence used here is SPINAL64 [FKE00]. Also shown (in solid gray) is the simulated spectrum produced by the fit Hamiltonian. For more details, see Appendix A.

between the two eigenvalues associated with the eigenvectors connecting the matrix element. Motivated by the observation of differential line-widths even amongst each set of transition lines, Lorentzian and Gaussian broadening are applied to each transition line separately. Similarly, an FID is computed under the evolution of the natural abundance Hamiltonian,

$$\mathcal{H}_{N.A.} = \sum_i -\omega_i Z_i \,, \tag{2.15}$$

where ω_i are the same as in (2.14). The total simulated FID is the weighted sum of both FIDs, where the ratio of the weights is determined by the dilution of the triply-labeled molecules, and is typically left as a parameter in the fit. The real part of the Fourier transform of the FID is then compared to the real part of the ^{13}C experimental spectrum obtained after polarization transfer from the abundant protons in the sample. Both spectra are normalized by the integral of the overall intensity, and a simplex optimization algorithm searches in the parameter space for values that minimize the squared sum of the residuals between them. A typical final fit is shown in Figure 2.4.

2.4 Relaxation

The line broadening extracted from the fit is typically around ~ 150Hz corresponding to free induction dephasing time, T_2^*, around $\sim$ 2ms. This is two orders of magnitude faster than the intrinsic dephasing time, T_2, which is on the order of ~ 100ms [BMR+06]. The major contribution to T_2^* is incoherent chemical shift dispersion resulting from inhomogeneity of the static field and susceptibility mismatch due to a non-spherical sample. Other contributions are from homonuclear intermolecular couplings and residual heteronuclear couplings (particularly C_m coupling to the methylene protons).

The spin lattice relaxation time, T_1, for the Carbon spins is on the order of 5 minutes, and is therefore irrelevant to the current experiments. The proton T_1 was measured by population inversion methods in different orientations and is typically about 50s. Since all experiments reported here start with polarization transfer from the abundant protons to the Carbon spins, we typically wait $\sim 5T_1$ between runs for the proton ensemble to relax to the thermal state. This presents a challenge for the experimentalist, and highlights an even more dire need to find ways to improve the signal-to-noise ratio without resorting to time averaging.

2.5 Control

2.5.1 Controllability

Even though we are operating in the regime where the computational basis differs from the eigenbasis of the Hamiltonian, the mixing is small enough that we can still approximately map spins to qubits. This addressability of single qubits, along with the two body Hamiltonian, is sufficient for universal control [DNBT02, NBD+02]. This answers the question of whether, in principal, the system is fully controllable. To actuate a desired evolution, we rely on two basic techniques: using multiple pulse sequences if the desired evolution is in Hamiltonian form; or numerically designed strongly modulating pulses for propagator design.

2.5.2 Pulse design

Given the time independent internal Hamiltonian, $\mathcal{H}_0$, and the form of the control Hamiltonians, $\{\mathcal{H}_j\}_{j=1\ldots r}$, the total Hamiltonian of the system can be written as

$$\mathcal{H}_s(t) = \mathcal{H}_0 + \sum_j u_j(t)\mathcal{H}_j \,, \tag{2.16}$$

where $u_j(t)$ are the *control parameters*. The evolution of the system is given by the propagator

$$U_s(\tau, u_j) = \mathcal{T} \exp\left[-i \int_0^\tau dt \left(\mathcal{H}_0 + \sum_j u_j(t)\mathcal{H}_j\right)\right] . \tag{2.17}$$

The central problem of pulse design is how to modulate the control parameters to realize a desired propagator U_d at some time τ. Or, formulated as an optimization problem, how to maximize some fitness function $\Phi(U_s, U_d)$ over the space of feasible parameters, u_j. This problem has proven to be much harder than the opposite problem: evaluating the propagator (2.17) given a particular sequence of control parameters. This naturally leads to the following approach to finding a solution to the original question:

- Start with an arbitrary choice for $u_j(t)$, then iterate the following steps until a satisfactory solution is found.
- Evaluate the propagator U_s using Equation (2.17).
- Knowing the desired unitary, U_d, calculate the fitness function Φ.
- Decide on a new set of parameters based on the history of the choice of parameters and the corresponding fitness functions.

The superiority of one scheme over another is in reducing the complexity of any of these steps to make the problem more tractable, but as it stands, all of the numerical schemes reduce to this search over the parameter space for a set of controls that optimize a given functional.

A common approach [FPB+02, KRK+05] is to parametrize the control Hamiltonian such that it is piecewise constant in some rotating frame. i.e. for $\mathcal{H}_1(\omega_1, \omega_{rf}, \phi, t)$ in Eq. (2.5), taking ω_{rf}, ω_1, and ϕ to be piecewise constant for periods of τ^m, the propagator (2.17) reduces to the product of the propagators for each period,

$$U(\tau) = \prod_m \exp\left\{-i\ \omega_{rf}^m\ \Sigma_Z\right\}\ \exp\left\{-i\left[\mathcal{H}_0 + \tilde{\mathcal{H}}_1(\omega_1^m, \phi^m)\right]\ \tau^m\right\} , \tag{2.18}$$

where $\tilde{\mathcal{H}}_1(\omega_1^m, \phi^m)$ is the time independent R.F. Hamiltonian in the rotating frame. Choosing the number of periods to be small greatly reduces the complexity of evaluating the propagator for the whole pulse sequence. With the fitness function defined as the gate fidelity (see Appendix D),

$$\Phi(U_s, U_d) := F_{HS}(U_s, U_d) = \frac{1}{d^2}\left|\mathrm{tr}(U_s^\dagger U_d)\right|^2 , \tag{2.19}$$

we were able to demonstrate high fidelity control in our system[BMR+05, BMR+06]. However, this scheme suffered a few drawbacks. First and foremost, the jumps in the amplitude and phase from one period to another caused phase transient effects that degraded the quality of the pulses. This is due [Laf08] to the limited bandwidth of the resonant probe circuit. Also, as the number of parameters expanded to accommodate a more demanding transformation or to reach for higher fidelities, the size of the optimization problem became highly taxing on the computational resources.

We then turn to another scheme [KRK+05] that saw success in liquid state NMR. The GRadient Ascent Pulse Engineering (GRAPE) algorithm, inspired by optimal control methods, explores the parameter space more purposefully. Again, the pulse is discretized into short periods Δt for which the control Hamiltonian is piecewise constant, and the propagators for each time step are simulated employing good knowledge of the Hamiltonians. It is easy to imagine that the local topology of the fitness function in the parameter space can provide a clue as to the best direction to move into for the next iteration to improve. The cleverness of the GRAPE algorithm is not that it evaluates the derivatives of the fitness function, but rather it is the *way* it evaluates them from quantities already calculated; namely the propagator of each time step. For a detailed and fluid explanation, see [Rya09].

We adapt the coded algorithm to find high fidelity implementations for the strong coupling regime. In addition, we supplement the code with a number of features, including

- The ability, with the same control fields, to simultaneously realize different pulses for different internal Hamiltonians. This is useful for example in the situation where the contribution to the signal from the natural abundance spins is to be averaged out.

- The ability to smooth pulses on the fly. The user has the option to smooth pulses every iteration as they are found. Pulses that are too jagged cannot be faithfully implemented due to the finite bandwidth of the resonant circuit. Figure 2.5 shows a pulse that has been found with the automatic smoothing turned on. The r.f. amplitude jumps are mostly less than $1\%/\mu s$.

- The ability to explicitly design pulses to be robust to variations in certain parameters. Figure 2.6 shows the fidelity profile of a typical pulse designed to be robust against r.f. power variations as well as chemical shift variations.

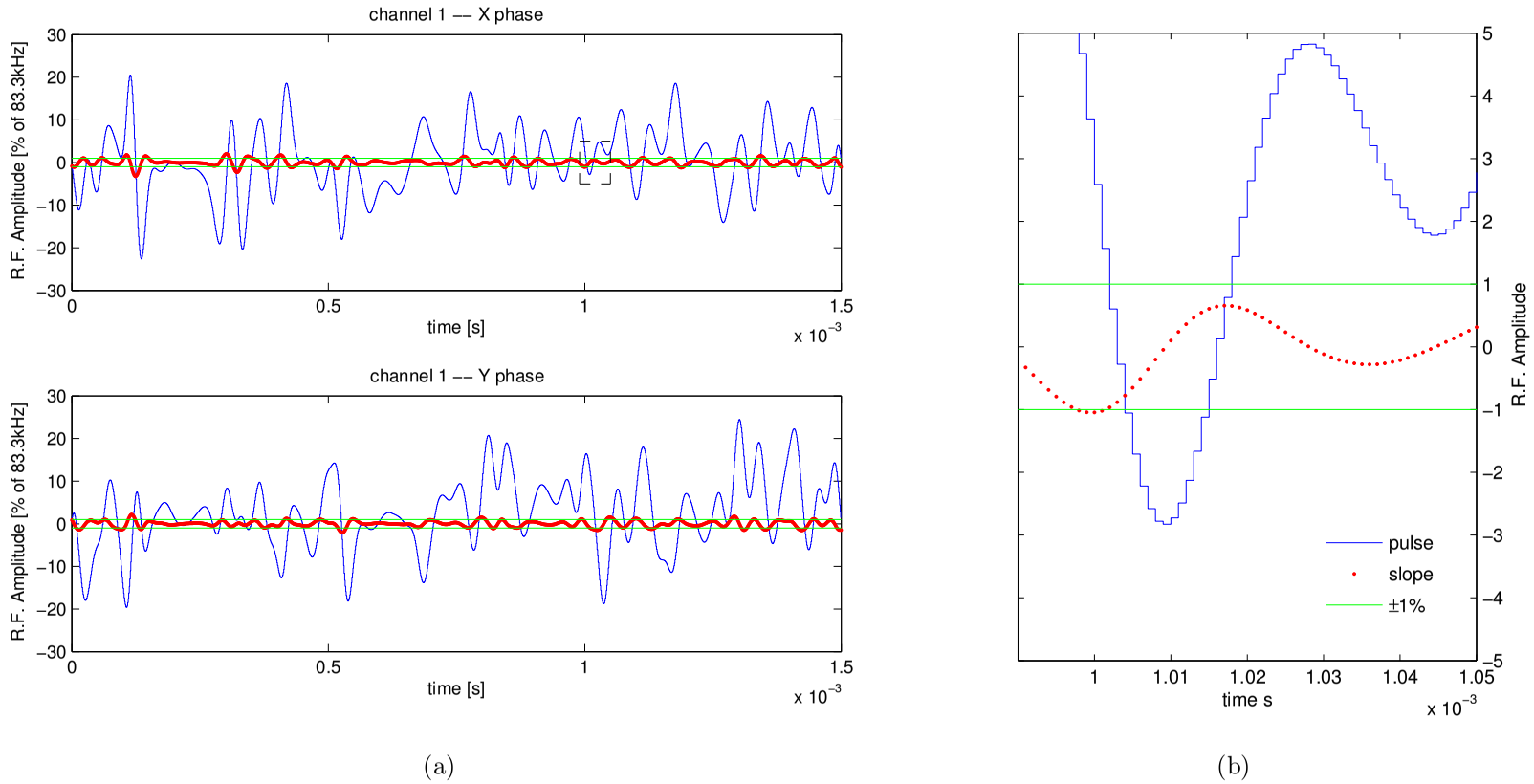

(a) (b)

Figure 2.5: Shown are (a) Typical pulse form found using the GRAPE algorithm, using the smooth-on-the-fly option, and (b) The discretization and slope of a portion of the pulse. The r.f. amplitude jumps are mostly within $\pm 1\%/\mu s$.

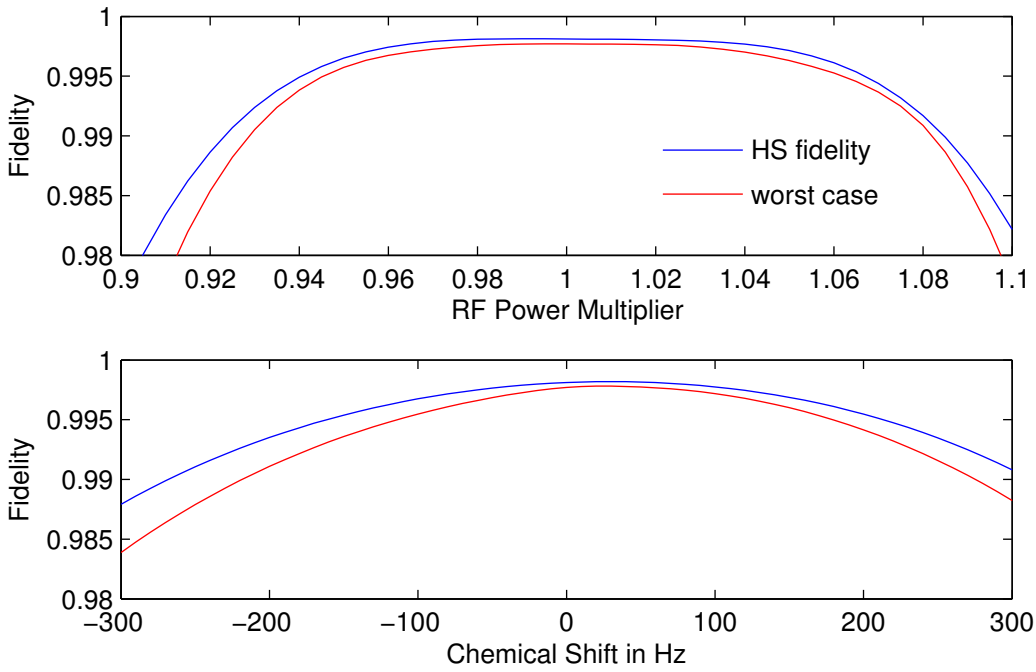

Figure 2.6: Typical fidelity profile for a robust pulse: shown is the fidelity as a function of RF multiplier and CS showing the robustness of the pulse form in Figure 2.5 to variations in these parameters. Shown are the gate fidelity (D.13) and worst case fidelity [Sil08].

2.5.3 Pulse Implementation Correction

Today's technology allows for very high precision pulse shaping, yet it is observed that the nominal fields in the vicinity of the sample do not match the pulse asked of the pulse generation unit. The discrepancy, typically in the range of 1%, is quite significant if one aims for high fidelity control. There are two components to this deviation; random fluctuations due to noise in the electronics responsible for signal generation, amplification, and detection; and a systematic portion that is primarily caused by residual (uncorrected for) non-linearities in the signal generation unit and the amplifiers, and by the limited bandwidth of the probe circuit.

To rectify [Rya09] these systematic imperfections, a pickup coil connected to the receiver unit in the spectrometer is used to measure the pulse at the sample space. This data is fed back for comparison with the original, 'ideal', pulse. A new pulse form that attempts to compensate for the imperfections is computed, and then sent back to the signal generation unit. This loop is repeated a number of times to reach a satisfactory, 'close enough', pulse form. Typically, the user would pick a number of feedback loops in advance –usually 4-8 is sufficient [Rya09].

Recent improvements to this scheme –to automate the decision making– start by defining a reasonably 'close enough' rectified pulse. First, the closeness of two pulses is defined as the sum of the squares of the residuals, normalized by the number of points in the (stroboscopic) observation. The normalization is to facilitate an overall comparison between pulses of different length. To estimate the contributions to the deviations that cannot be rectified by the implementation-correction scheme, the spectrometer is asked to produce the same original pulse a number of times, and statistics is collected for the discrepancies between the different implementations of the same pulse, thus establishing a realistic estimate of how well the pulses can be rectified, or how close is close enough.

In this version of the scheme, the feedback loop runs continuously, and is only interrupted when it reaches a maximum number of iterations, or, more favourably, if the figure of merit surpasses an appropriately chosen threshold based on the aforementioned realistic estimate of the random and systematic contributions to the deviation.

The pulse implementation imperfections depend on the pulse power. Therefore, it is important that the pulses are corrected at the power that they will be used at. However, this value might not be known beforehand since properly corrected pulses are needed for calibration purposes. One possible solution, which is currently part of the calibration process, is to correct the calibration pulse at the different powers in the calibration range, and only use each corrected pulse with the power at which it has been corrected.

Figure 2.7 shows the output of a typical pulse implementation correction procedure. Shown are the pulse forms of the successive attempts at pulse correction, as detected by the pickup coil near the sample space. Reported also are the figures of merit for all trials, and perhaps worth noting is the two orders of magnitude improvement from the first to the last attempts.

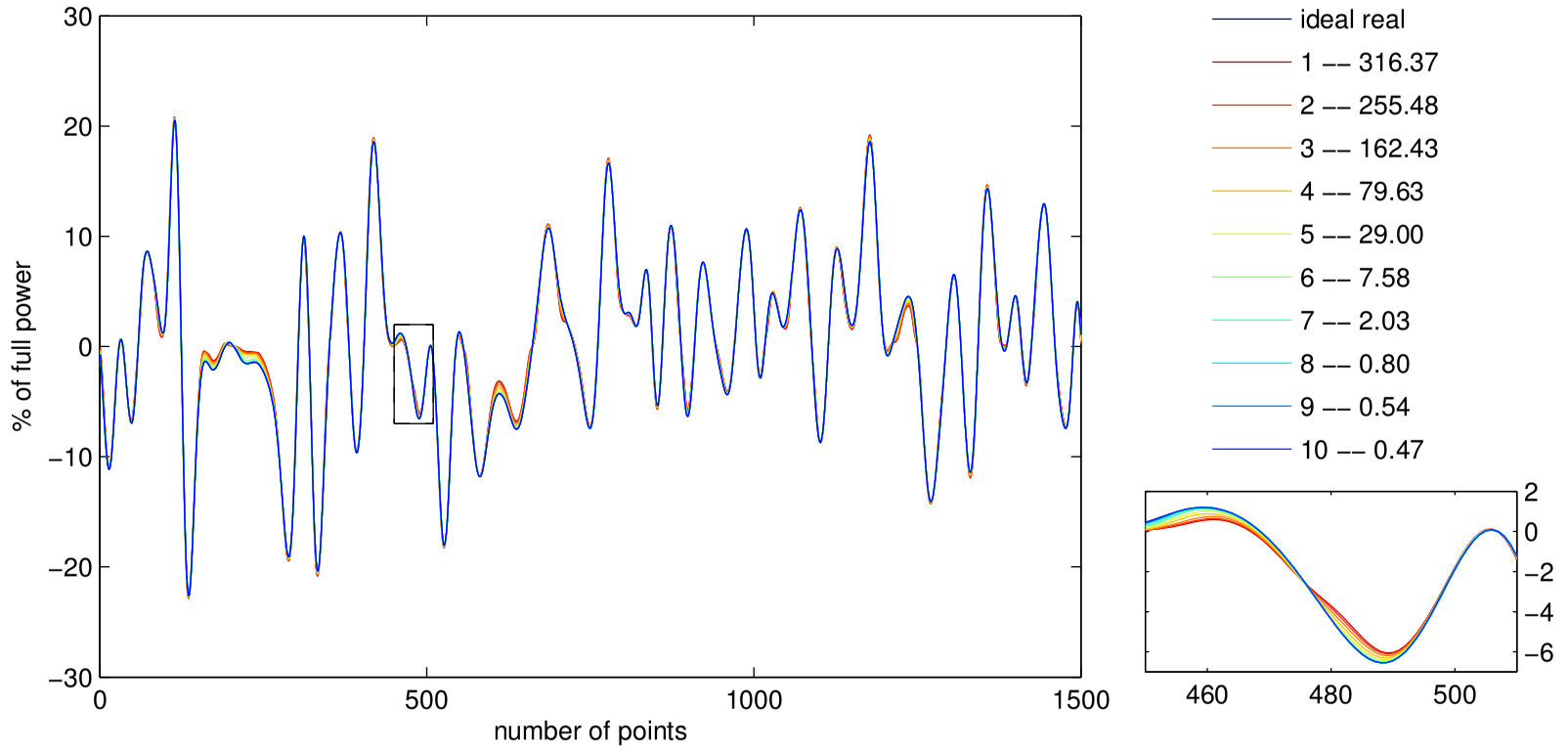

Figure 2.7: Measured (X-quadrature) pulse shapes by the pick up coil from successive tries to implement a given "ideal" pulse. a typical pulse implementation correction. The inset (southeast) expands the patch marked by the black rectangle in the main figure. The legend shows the color-code of the successive tries accompanied by the value of the figure of merit used to judge how close the measured pulse is to the ideal. Even though the red pulse is not far off, we can see orders of magnitude improvement in the figure of merit

Chapter 3

Quantum error correction

3.1 Introduction

One of the crucial requirements [DiV00] for quantum information processing is the ability to protect the fragile quantum information during computation; either by encoding the information in subspaces of the system's Hilbert space where it is not terribly degraded by the noise or by an active scheme that detects and rectifies errors from time to time, or by a hybrid system of both.

Active quantum error correction was first developed [Sho95, Ste96, CS96] in analogy to classical error correction. The basic idea being that the information is encoded redundantly in multiple copies such that a majority type poll after some of the data has been corrupted would reveal the correct value of the encoded information.

Possible points of contention arose in relation to this analogy, but clever responses quickly dispensed of them, culminating in theories of quantum error correction and fault tolerant quantum computing. A rough sketch of these arguments are presented below; the interested reader is referred to [Got97, NC00, KLP05] for more detailed and rigorous accounts.

- As mentioned, in classical error correction, redundancy is used so that if some bits are corrupted, the majority of the redundant copies remain intact, allowing for recovery; the problem is, this cannot be directly carried over to the quantum case for there is no universal cloner of quantum states. The solution can be gleamed in the observation that copying a classical bit amounts to correlating its value with another's. The answer, then, lies in employing *quantum* correlations to encode quantum coherences; that is to say in using entanglement to encode superpositions [Sho95, Ste96].

- In classical error correction it is assumed that it is possible to measure all the bits to extract the error syndrome, while in the quantum case, measurements would invariably disturb the state. This is cleverly circumvented [Sho95, DS96] by designing the syndrome measurement such that it would destroy the coherences between the syndrome subspaces, while the encoded coherences are preserved. In other words, the syndrome measurement reveals a global property about the overall state without distinguishing between the different encoded states. For example, as will be shown in the next section, the error syndrome for the 3-bit repetition code is revealed through measurements of qubit parities without measuring the qubits themselves.

- A classical computer only needs to preserve the bit values, while a quantum computer also needs to keep phase information. Fortunately, it is straight forward to make phase errors look like bit errors just by changing bases using the Hadamard gate. Interestingly, that same gate is all that is needed in addition to reversible classical computation for universal quantum computation [Shi02, Aha03].

- There is an infinite number of possible errors. However, by the linearity of quantum dynamics, if a code corrects for errors E and F, then it will correct $aE + bF$. Thus, when designing a code, we only need to consider whether the code can correct a basis of errors.

All of the above can be formalised in a theory of quantum error correction [KL97, BDSW96], the corner stone of which is the following necessary and sufficient condition for perfect recovery of an encoded state after being subjected to errors: A quantum code $\mathcal{C}$ with basis codewords $\{|\psi_i\rangle\}$ will correct for all errors in $span(\mathcal{E})$ if and only if

$$\langle\psi_j|E_a^\dagger E_b|\psi_k\rangle = c_{ab}\delta_{jk}, \tag{3.1}$$

where $|\psi_j\rangle$ and $|\psi_k\rangle$ run over all possible basis codewords, E_a and E_b run over all possible combinations of errors in $\mathcal{E}$, and c_{ab} is independent of j and k. If c_{ab} is equal to δ_{ab}, the code is a *nondegenerate* code [Got97]. That is to say, different errors are distinguishable.

Active quantum error correction techniques have been experimentally realized in the liquid-state-NMR [CPM+98, LVZ+99, KLMN01] and ion-traps [CLS+04] implementations of a quantum information processor. In each of these implementations, a quantum error-correction code (QECC) was used to protect against the particular errors present in the respective systems. In this Chapter, we report on the implementation of a three-qubit QECC that corrects phase errors induced by the environment, in a single-crystal solid-state NMR system.

3.2 3-bit code

The 3-bit repetition code was introduced by Shor [Sho95] as part of a 9-qubit code that is able to protect against an arbitrary single qubit error. The phase variant [Bra96] of the 3-bit repetition code encodes a single qubit in three qubits as follows:

$$|0\rangle \rightarrow |\bar{0}\rangle = |+++\rangle\,, \tag{3.2}$$

$$|1\rangle \rightarrow |\bar{1}\rangle = |---\rangle\,. \tag{3.3}$$

where $|\pm\rangle = |0\rangle \pm |1\rangle$ and the logical basis are denoted by $\{|\bar{0}\rangle, |\bar{1}\rangle\}$. In the stabilizer formalism [Got97, Pou05], the stabilizer group generators for this code are $\{XXI, IXX\}$. This code can be employed to correct for various sets of errors by choosing different decoding circuits, but first, we focus on the set $\mathcal{E} = \{ZII, IZI, IIZ, III\}$. It is straight forward to show that the conditions 3.1 are satisfied: first we evaluate the product $E_a^\dagger E_b$,

$$\{E_a^\dagger E_b : E_a, E_b \in \mathcal{E}\} = \begin{cases} \{ZII, IZI, IIZ, ZZI, ZIZ, IZZ\} & a \neq b \\ \{III\} & a = b\,, \end{cases} \tag{3.4}$$

and, noting that $Z|\pm\rangle = |\mp\rangle$, $\langle\psi_j|E_a^\dagger E_b|\psi_k\rangle$ evaluates to

- for the case $j \neq k$,

$$\langle\bar{0}|E_a^\dagger E_b|\bar{1}\rangle = \langle\bar{1}|E_a^\dagger E_b|\bar{0}\rangle = 0 \quad \forall a, b\,; \tag{3.5}$$

- and for the case $j = k$,

$$\langle\bar{0}|E_a^\dagger E_b|\bar{0}\rangle = \langle\bar{1}|E_a^\dagger E_b|\bar{1}\rangle = \begin{cases} 0 & a \neq b \\ 1 & a = b\,. \end{cases} \tag{3.6}$$

Thus, putting everything together, we get

$$\langle\psi_j|E_a^\dagger E_b|\psi_k\rangle = \delta_{ab}\delta_{jk}\,, \tag{3.7}$$

which means that the code will correct for any linear combination of errors in $\mathcal{E}$ (but not a product.) That is to say, it will correct a phase flip on any of the qubits; or the "nothing happened" operation; or the dephasing map,

$$\Lambda_\theta(\rho) = \cos^2(\theta) I\rho I + \sin^2(\theta) Z\rho Z\,, \tag{3.8}$$

on one of the qubits; or a selective phase rotation on any of the qubits, for e.g.

$$Z_1^\theta := e^{-i\ \theta/2\ ZII} = \cos(\theta/2)\ III - i\sin(\theta/2)\ ZII\,. \tag{3.9}$$

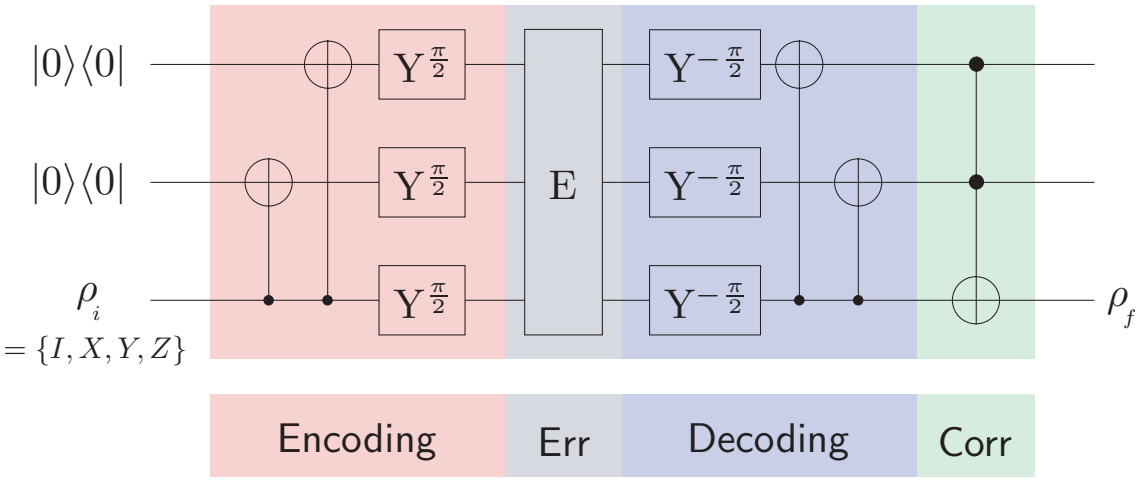

Figure 3.1: The quantum circuit of the phase variant of the three-qubit QECC, showing the encoding, decoding, and error-correction steps. The first two qubits, the ancillas, are initialized to the $|00\rangle$ state, and the third qubit carries the information to be encoded. After the decoding and correction operations, the third qubit is restored to its initial state, while the other two qubits carry information about which error had occured. The $Y^{\frac{\pi}{2}}$ gate is a $\frac{\pi}{2}$-rotation about the Y axis.

A quantum circuit that accomplishes [Bra96] the encoding, decoding, and error-correction steps is shown in Fig.3.1. The encoding process takes a qubit in the state $\alpha|0\rangle + \beta|1\rangle$, adds two ancilla qubits prepared in the $|00\rangle$ state, and outputs the 3-qubit encoded state $\alpha|+++\rangle + \beta|---\rangle$. After the error channel, the recovery process decodes the state on the information-carrying-qubit, and the ancilla qubits carry syndrome information about the errors that have occurred. The nondegeneracy of the code (by expression (3.7)) implies that each of the error basis will leave a particular signature. It is straightforward to show that syndromes 00, 10, 01, and 11 correspond to the occurrence of errors III, ZII, IZI, and IIZ, respectively.

Next, we examine the performance of the 3-bit code under different error models that might be encountered in our system. The figure of merit used herein to judge the performance of the code is the *entanglement fidelity*. In particular, we use the expression (D.22) in Appendix D for the single-qubit average entanglement fidelity, which is experimentally accessible by measuring the fraction of surviving signal given input states X, Y, and Z.

3.3 Error models

For the computational register under investigation, (dephasing) noise comes in the following forms:

- **Coherent phase errors** due to extraneous pulse implementation errors, phase transients, or superfluous evolution under the natural Hamiltonian (e.g. under the Zeeman term.) These are unitary errors (that cause no loss of coherence) and can therefore be inverted if tracked properly, but in case tracking that evolution is not possible, quantum error correction becomes a valuable tool. For example, an error in the form of the phase rotation Z_1^θ (Eq. (3.9)) can be easily inverted if the value of θ is known. However, a quantum error correcting code (the 3-bit phase code) will correct for that error for any value of θ, thus precluding the need to track its value.

- **Incoherent phase errors** due to chemical shift dispersion or other inhomogeneities. The loss of coherence is over the ensemble; each member of the ensemble sees a different value for some coupled classical degree of freedom. Errors of this nature have been dealt with using refocussing techniques (e.g. spin echo), or by carefully designing the control fields to generate the same evolution over the ensemble. Quantum error correction can be used with, or in lieu of, these other techniques to improve robustness to ensemble errors.

- **Decoherent phase errors** due to spin diffusion (via the flip-flop term). This is the picture typically conjured when thinking about quantum noise. The system of interest couples to an environment –an uncontrollable quantum degree of freedom initially in some mixed state– and loss of coherence occurs when this environment is traced over after the interaction.

3.3.1 Correlated phase rotations

Here, the performance of the 3-bit code is examined against a fully coherent error, whose form and magnitude are completely known. This allows for an analytic examination of the action of the code, which is a simple yet informative exercise. The coherent correlated phase rotation error operator (as shown in the quantum circuit, Fig. 3.2 (c)) is a symmetric three-fold tensor product of the single qubit

phase gate, Eq. (3.9), and can be expanded as

$$\begin{aligned}\mathcal{E}(\theta) =& \bigotimes_{j=1}^{3} Z^{\theta} \\ =&(\cos\tfrac{\theta}{2}\mathbb{1} - i\sin\tfrac{\theta}{2}Z_1)(\cos\tfrac{\theta}{2}\mathbb{1} - i\sin\tfrac{\theta}{2}Z_2)(\cos\tfrac{\theta}{2}\mathbb{1} - i\sin\tfrac{\theta}{2}Z_3) \\ =&\cos^3\tfrac{\theta}{2}\mathbb{1} \\ &- i\cos^2\tfrac{\theta}{2}\sin\tfrac{\theta}{2}(Z_1 + Z_2 + Z_3) \\ &- \cos\tfrac{\theta}{2}\sin^2\tfrac{\theta}{2}(Z_1Z_2 + Z_1Z_3 + Z_2Z_3) \\ &+ i\sin^3\tfrac{\theta}{2}(Z_1Z_2Z_3)\,.\end{aligned} \tag{3.10}$$

An arbitrary single-qubit input state $|\phi\rangle = \alpha|0\rangle + \beta|1\rangle$ is encoded as $|\psi\rangle = \alpha|+++\rangle + \beta|---\rangle$, which is mapped by the noise operator to

$$\begin{aligned}\mathcal{E}(\theta)|\psi\rangle =&\cos^3\tfrac{\theta}{2}(\alpha|+++\rangle + \beta|---\rangle) \\ &- i\cos^2\tfrac{\theta}{2}\sin\tfrac{\theta}{2}(\alpha|-++\rangle + \beta|+--\rangle + \alpha|+-+\rangle + \beta|-+-\rangle + \alpha|++-\rangle + \beta|--+\rangle) \\ &- \cos\tfrac{\theta}{2}\sin^2\tfrac{\theta}{2}(\alpha|--+\rangle + \beta|++-\rangle + \alpha|-+-\rangle + \beta|+-+\rangle + \alpha|+--\rangle + \beta|-++\rangle) \\ &+ i\sin^3\tfrac{\theta}{2}(\alpha|---\rangle + \beta|+++\rangle)\,,\end{aligned} \tag{3.11}$$

and after the decoding circuit, the 3 qubit state is

$$\begin{aligned}\mathcal{D}\circ\mathcal{E}(\theta)|\psi\rangle =&\cos^3\tfrac{\theta}{2}(\alpha|000\rangle + \beta|100\rangle) \\ &- i\cos^2\tfrac{\theta}{2}\sin\tfrac{\theta}{2}(\alpha|111\rangle + \beta|011\rangle + \alpha|010\rangle + \beta|110\rangle + \alpha|001\rangle + \beta|101\rangle) \\ &- \cos\tfrac{\theta}{2}\sin^2\tfrac{\theta}{2}(\alpha|101\rangle + \beta|001\rangle + \alpha|110\rangle + \beta|010\rangle + \alpha|011\rangle + \beta|111\rangle) \\ &+ i\sin^3\tfrac{\theta}{2}(\alpha|100\rangle + \beta|000\rangle) \\ =&\quad(\alpha|0\rangle + \beta|1\rangle)[\cos^3\tfrac{\theta}{2}|00\rangle + i\cos^2\tfrac{\theta}{2}\sin\tfrac{\theta}{2}(|10\rangle + |01\rangle) - \cos\tfrac{\theta}{2}\sin^2\tfrac{\theta}{2}|11\rangle] \\ &+ (\alpha|1\rangle + \beta|0\rangle)[i\cos^2\tfrac{\theta}{2}\sin\tfrac{\theta}{2}|11\rangle - \cos\tfrac{\theta}{2}\sin^2\tfrac{\theta}{2}(|01\rangle + |10\rangle) + i\sin^3\tfrac{\theta}{2}|00\rangle]\,.\end{aligned} \tag{3.12}$$

Taking the partial trace over the two rightmost qubits gives the state

$$\begin{aligned}\rho_d =&(\cos^6\tfrac{\theta}{2} + 2\cos^4\tfrac{\theta}{2}\sin^2\tfrac{\theta}{2} + \cos^2\tfrac{\theta}{2}\sin^4\tfrac{\theta}{2})|\phi\rangle\langle\phi| \\ &+ (\cos^4\tfrac{\theta}{2}\sin^2\tfrac{\theta}{2} + 2\cos^2\tfrac{\theta}{2}\sin^4\tfrac{\theta}{2} + \sin^6\tfrac{\theta}{2})|\phi'\rangle\langle\phi'| \\ =&\cos^2\tfrac{\theta}{2}(\cos^2\tfrac{\theta}{2} + \sin^2\tfrac{\theta}{2})^2|\phi\rangle\langle\phi| + \sin^2\tfrac{\theta}{2}(\cos^2\tfrac{\theta}{2} + \sin^2\tfrac{\theta}{2})^2|\phi'\rangle\langle\phi'|\,,\end{aligned} \tag{3.13}$$

where $|\phi'\rangle = \alpha|1\rangle + \beta|0\rangle$. The fidelity of the input state with the decoded state is

$$\langle\phi|\rho_d|\phi\rangle = \cos^2\tfrac{\theta}{2}\,|\langle\phi|\phi\rangle|^2 + \sin^2\tfrac{\theta}{2}\,|\langle\phi|\phi'\rangle|^2\,, \tag{3.14}$$

where the variable substitutions $x = \cos^2\frac{\theta}{2}$ and $y = \sin^2\frac{\theta}{2}$ were used to simplify the expression. Note that $\langle\phi|\phi'\rangle = (\alpha^*\langle 0| + \beta^*\langle 1|)(\alpha|1\rangle + \beta|0\rangle) = \alpha^*\beta + \beta^*\alpha$ is a

real quantity, which makes the second term in Eq. (3.14) always non-negative. The entanglement fidelity of this single-qubit map is given by Eq. (D.15),

$$\begin{aligned} F_e(\mathcal{D}\circ\mathcal{E}(\theta)) &= \tfrac{1}{4}\left[F_{|0\rangle}+F_{|1\rangle}+F_{|+\rangle}+F_{|-\rangle}+F_{|+i\rangle}+F_{|-i\rangle}\right]-\tfrac{1}{2} \\ &= \tfrac{1}{4}\left[6\cos^2\tfrac{\theta}{2}+2\sin^2\tfrac{\theta}{2}\right]-\tfrac{1}{2} \\ &= \cos^2\tfrac{\theta}{2} \\ &= \tfrac{1}{2}(1+\cos\theta)\,. \end{aligned} \tag{3.15}$$

If the correction step had been applied, the state would have been

$$\begin{aligned} \mathcal{C}\circ\mathcal{D}\circ\mathcal{E}(\theta)|\psi\rangle =& \cos^3\tfrac{\theta}{2}(\alpha|000\rangle+\beta|100\rangle) \\ &- i\cos^2\tfrac{\theta}{2}\sin\tfrac{\theta}{2}(\alpha|011\rangle+\beta|111\rangle+\alpha|010\rangle+\beta|110\rangle+\alpha|001\rangle+\beta|101\rangle) \\ &- \cos\tfrac{\theta}{2}\sin^2\tfrac{\theta}{2}(\alpha|101\rangle+\beta|001\rangle+\alpha|110\rangle+\beta|010\rangle+\alpha|111\rangle+\beta|011\rangle) \\ &+ i\sin^3\tfrac{\theta}{2}(\alpha|100\rangle+\beta|000\rangle) \\ =& \quad(\alpha|0\rangle+\beta|1\rangle)[\cos^3\tfrac{\theta}{2}|00\rangle+i\cos^2\tfrac{\theta}{2}\sin\tfrac{\theta}{2}(|10\rangle+|01\rangle)+i\cos^2\tfrac{\theta}{2}\sin\tfrac{\theta}{2}|11\rangle] \\ &+ (\alpha|1\rangle+\beta|0\rangle)[-\cos\tfrac{\theta}{2}\sin^2\tfrac{\theta}{2}|11\rangle-\cos\tfrac{\theta}{2}\sin^2\tfrac{\theta}{2}(|01\rangle+|10\rangle)+i\sin^3\tfrac{\theta}{2}|00\rangle]\,, \end{aligned} \tag{3.16}$$

and again, tracing out qubits 2 and 3,

$$\begin{aligned} \rho_c =& (\cos^6\tfrac{\theta}{2}+3\cos^4\tfrac{\theta}{2}\sin^2\tfrac{\theta}{2})|\phi\rangle\langle\phi| \\ &+ (3\cos^2\tfrac{\theta}{2}\sin^4\tfrac{\theta}{2}+\sin^6\tfrac{\theta}{2})|\phi'\rangle\langle\phi'| \\ =& \cos^4\tfrac{\theta}{2}(1+2\sin^2\tfrac{\theta}{2})\;|\phi\rangle\langle\phi|+\sin^4\tfrac{\theta}{2}(1+2\cos^2\tfrac{\theta}{2})\;|\phi'\rangle\langle\phi'|\,, \end{aligned} \tag{3.17}$$

and the fidelity with the input state is given by

$$\langle\phi|\rho_c|\phi\rangle = \cos^4\tfrac{\theta}{2}(1+2\sin^2\tfrac{\theta}{2})|\langle\phi|\phi\rangle|^2+\sin^4\tfrac{\theta}{2}(1+2\cos^2\tfrac{\theta}{2})|\langle\phi|\phi'\rangle|^2\,. \tag{3.18}$$

In this case, the entanglement fidelity is

$$\begin{aligned} F_e(\mathcal{C}\circ\mathcal{D}\circ\mathcal{E}(\theta)) &= \tfrac{1}{4}\left[F_{|0\rangle}+F_{|1\rangle}+F_{|+\rangle}+F_{|-\rangle}+F_{|+i\rangle}+F_{|-i\rangle}\right]-\tfrac{1}{2} \\ &= \tfrac{1}{4}\left[4\cos^4\tfrac{\theta}{2}(1+2\sin^2\tfrac{\theta}{2})+2\right]-\tfrac{1}{2} \\ &= \cos^4\tfrac{\theta}{2}(1+2\sin^2\tfrac{\theta}{2}) \\ &= \tfrac{1}{4}(2+3\cos\theta-\cos^3\theta)\,, \end{aligned} \tag{3.19}$$

clearly showing the gain from quantum error correction for $0<\theta<\pi/2$. This is illustrated in Figure 3.2 (a). Also shown in Figure 3.2 (b) are experimentally determined entanglement fidelities before and after the correction steps. The error operator was engineered by shifting the phase of all subsequent pulses as well as the receiver. Again, the advantage of corrections is clear.

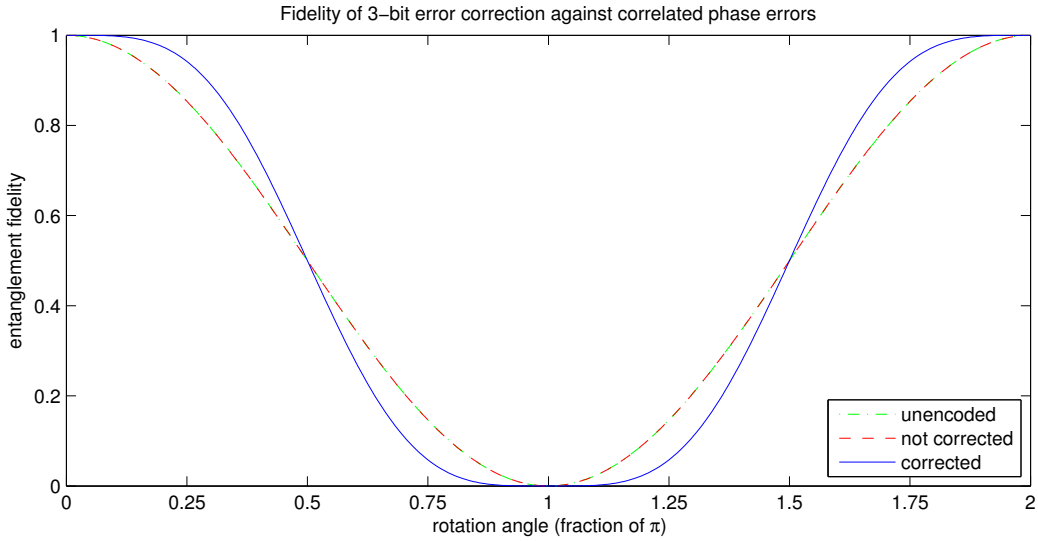

(a) Ideal simulation

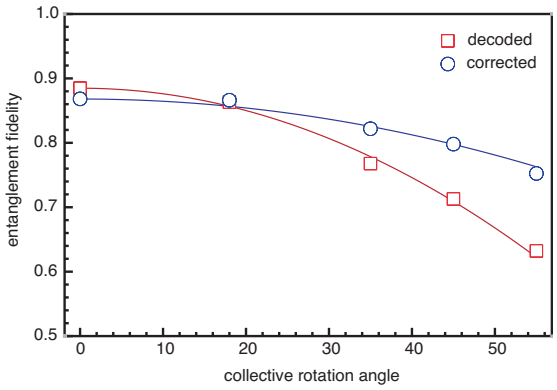

(b) Experimental results

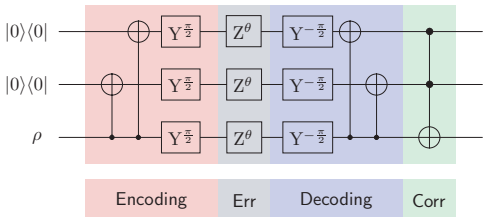

(c) Circuit

Figure 3.2: (c) The quantum circuit of the phase variant of the three-qubit QECC, showing the encoding, decoding, and error-correction steps. The error channel examined here is a correlated phase rotation on all qubits; (a) The entanglement fidelities of the 3-bit code correcting for a correlated phase error. The single qubit unencoded fidelity is shown in green, and in red and blue are the fidelities before and after the correction step, respectively; (b) The entanglement fidelities as measured before (red squares) and after (blue circles) the correction step. The correlated phase error was implemented by changing the reference frame of pulses subsequent to the noise.

3.3.2 Full Internal Hamiltonian

Here we examine the performance of the 3-bit phase code under the natural evolution of the system; Between the encoding and recovery operations, the system is left to evolve unobstructed under the full natural Hamiltonian, both homonuclear and heteronuclear parts. The experimentally determined entanglement fidelities are shown in Figure 3.3, demonstrating the advantage of quantum error correction. The syndrome information (see inset in Figure 3.3) indicate that the dominant phase error is on the methylene carbon, C_m. The troughs in the unencoded and decoded data indicate that the error is, at least partially, coherent. However, full simulation of the dynamics of the carbon subsystem (shown in Figure 3.4) suggest a longer timescale for the coherent effects. We conclude that the coherent effects are due to the strong coupling between C_m and (one of) the methylene protons. This conclusion is reaffirmed by the results reported in (the following) section 3.3.3.

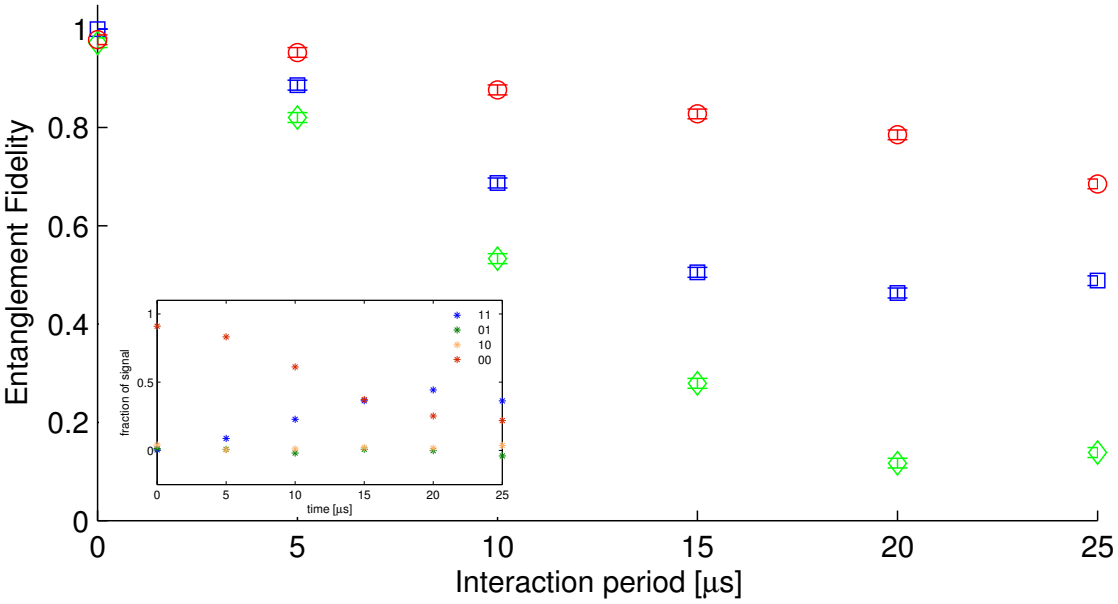

Figure 3.3: Experimentally determined entanglement fidelities for (blue squares) unencoded, (green diamonds) before, and (red circles) after the correction step. After encoding, a variable delay is implemented before the recovery process. During the delay, the system evolves unobstructed under the heteronuclear and homonuclear natural Hamiltonians. The troughs in the unencoded and decoded data are indicative of the presence of a coherent error. The inset shows the intensities measured for the different syndromes; the dominant error is a phase rotation on the bottom qubit (C_m).

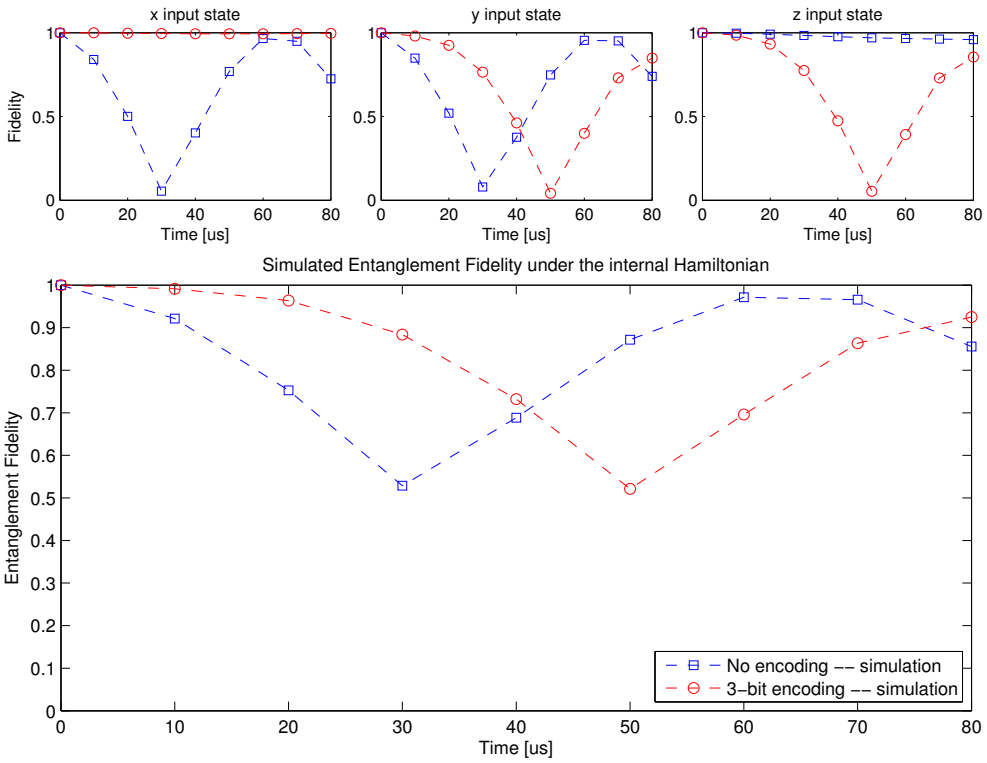

Figure 3.4: Shown are full-simulation results of (top) the fraction of surviving signal for input states X, Y, and Z; and (bottom) the resulting entanglement fidelity of the evolution map under the natural carbon subsystem Hamiltonian for various delays. As expected, the dominant contribution comes from the chemical shift evolution, as evidenced by the (almost) stabilization of the unencoded Z input state.

3.3.3 Partial decoupling

In this section, the 3-bit phase code is employed to protect a single qubit against errors from evolution under the natural Hamiltonian of the carbon subsystem as well as residual heteronuclear couplings between the carbons and protons due to partial decoupling of the protons using the SPINAL64 sequence [FKE00] at 70kHz. Figure 3.5 shows a summary of the experimental results. First, we note in comparison to results from the previous section, that the entanglement fidelity is sustained at higher values for all times. This is consistent with the picture that the heteronuclear interactions are the dominant interactions in the absence of decoupling. From the syndrome information shown in Figure 3.5 (a), the major contributions are from phase rotations on C_1 and C_m. This is to be expected, since, in this orientation, the chemical shifts of these two spins are the dominant terms in the internal carbon Hamiltonian.

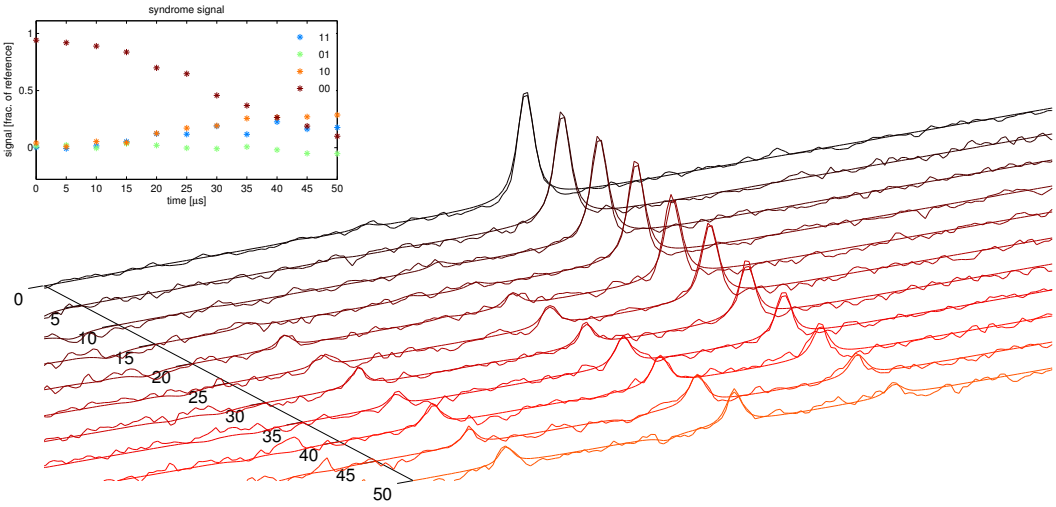

(a) Syndrome Information

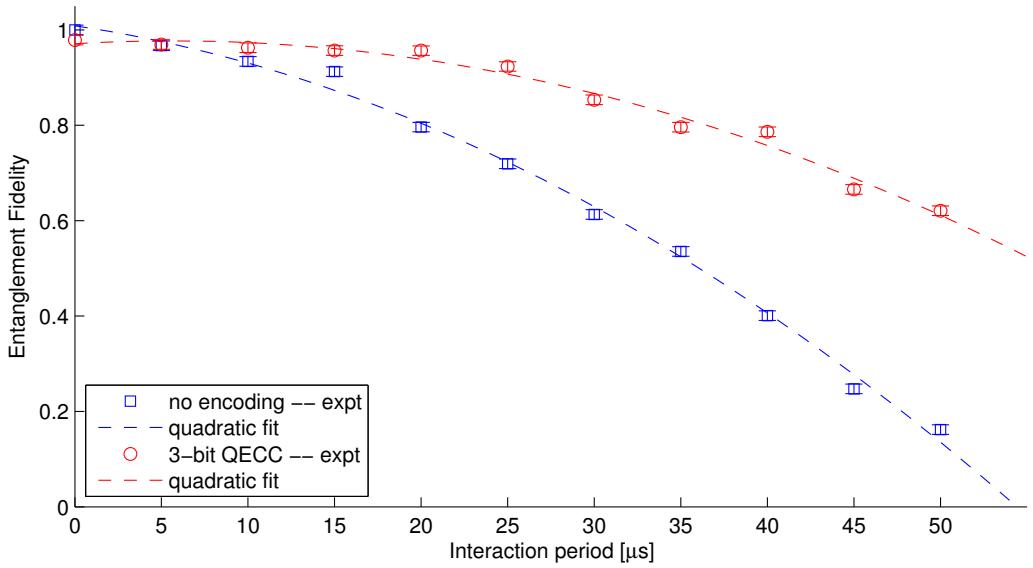

(b) Entanglement Fidelity

Figure 3.5: Summary of experimental results for the *partial decoupling* map: the system evolves under the natural Hamiltonian as well as 70khz decoupling fields that partially modulate the heteronuclear interactions (between the carbons and protons.) Shown are (b) the single-qubit entanglement fidelities in the cases where no encoding (blue squares) or the 3-bit code (red circles) are employed; and (a) syndrome information as extracted from the shown C_m spectra, which were obtained after the recovery process. The syndrome data shows almost equal contribution from phase errors on C_m and C_1.

3.4 Two rounds

In the previous sections, and indeed in previous experimental demonstrations of quantum error correction, it was shown that it is possible to correct for noise with noisy gates. Obviously, there is a limit to how much implementation errors can be tolerated before they overwhelm the error correction protocol. Thus, the ability to demonstrate error correction has become a benchmark of high-fidelity control. A natural question to ask is, whether we have high-enough-fidelity control to perform multiple rounds of error correction. Of course, to perform multiple rounds, one needs a fresh supply of pure (or pure enough) ancillas to ensure that entropy is flowing in the proper direction. However, *assuming* we have a fresh supply of ancillas, is it possible, with the current level of control, to perform meaningful multiple rounds of quantum error correction?

We devise a way to experimentally determine the entanglement fidelity of multiple rounds of error correction and use it to experimentally determine the entanglement fidelity of two rounds of the 3-bit phase code. The scheme requires a number of experiments that grows as s^{m-1}, where s is the number of possible nondegenerate syndromes of the code, and m is the number of rounds of correction performed. In this sense, the applicability of the scheme is very limited. For our purposes, after the first round of error correction, the surviving polarization from the various input states is distributed over the various subspaces of the Hilbert space corresponding to the various syndromes. For the second round, for each syndrome, we project into the subspace of the syndrome and perform error correction in that subspace, and then sum over all possible syndromes. The pulse sequence for this experiment is shown in Figure 3.6, and the experimental results are shown in Figure 3.7.

We demonstrate that beyond a certain error rate, there is an advantage to performing multiple rounds of error correction with our current level of control. The big initial drop in the experimentally determined two-round entanglement fidelity is due to the projection operation, which obviously would not be needed if pure ancillas are available.

3.5 Conclusion

We were able to demonstrate the advantage of performing quantum error correction to protect against phase errors –coherent, incoherent and decoherent– that arise naturally in the solid-state NMR system. We have shown that this is possible with the quality of control currently available. Moreover, we have shown that multiple rounds are also possible with current control levels. In addition to existing methods like decoupling and refocusing, this is a viable tool in the fight against decoherence.

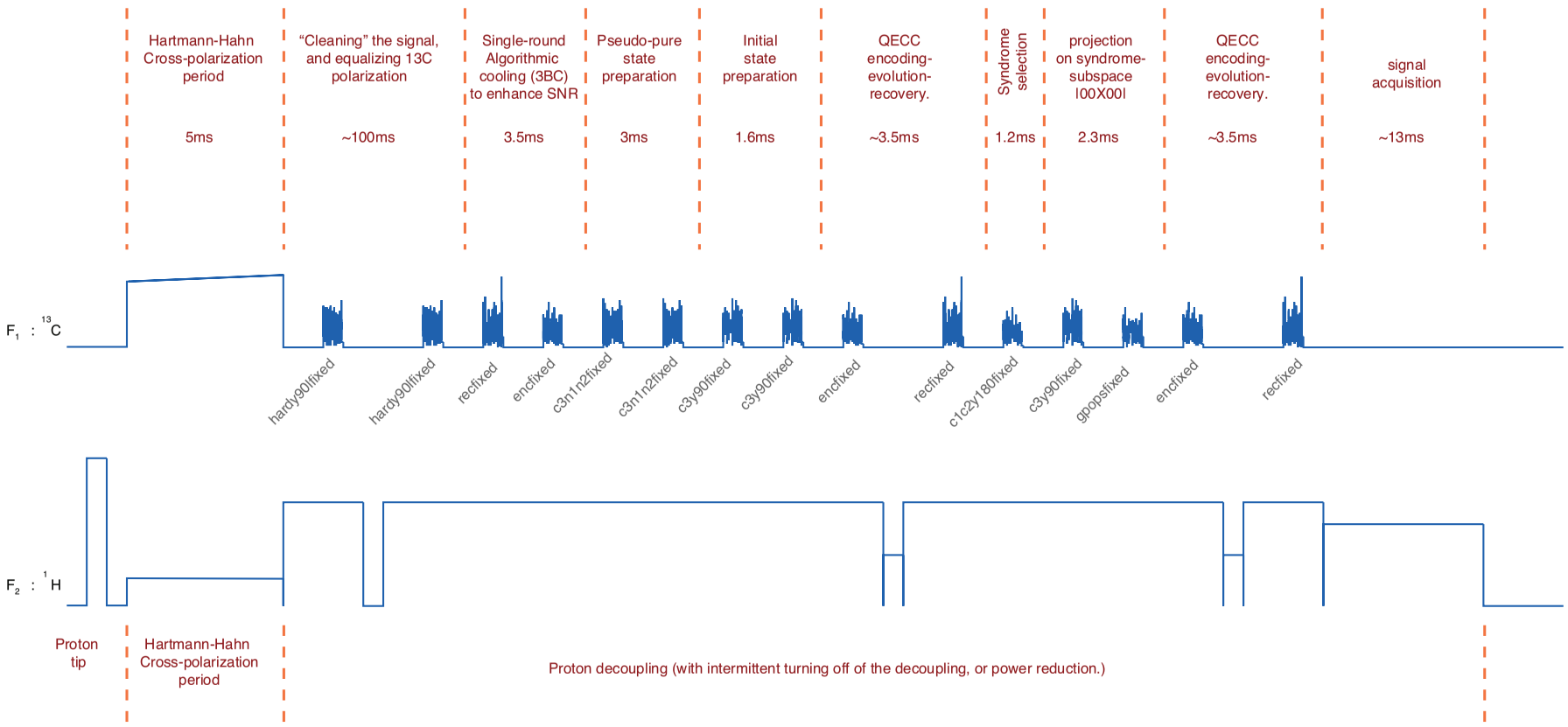

Figure 3.6: The pulse program for two rounds of error correction. The Carbon (Proton) pulses are sent on Channel F_1 (Channel F_2). Not shown in the figure are the phase cycles used to create pseudo-pure state and to select appropriate subspace for second round. Obviously, the time axis is not to scale.

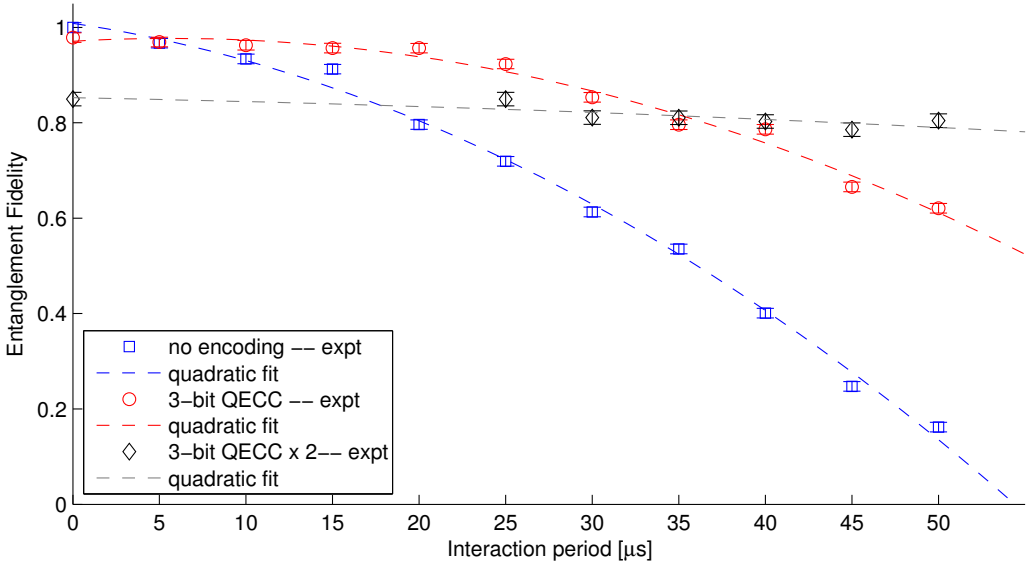

Figure 3.7: Summary of experimental results for the *partial decoupling* map: the system evolves under the natural Hamiltonian as well as 70khz decoupling fields that partially modulate the heteronuclear interactions (between the carbons and protons.) Shown are the single-qubit entanglement fidelities in the cases where no encoding is employed (blue squares); or one round of the 3-bit code (red circles); or two rounds of the 3-bit code (black diamonds).

Chapter 4

Application to foundational questions

4.1 Testing contextuality on quantum ensembles with one quantum bit.

4.1.1 Introduction

The Bell-Kochen-Specker (BKS) theorem [Spe60, Bel66, KS67, Mer93] states that *no* noncontextual hidden-variables (NCHV) theory can reproduce the predictions of quantum mechanics for correlations between measurement outcomes of some sets of observables. Any such set of observables constitutes a proof of the theorem. Recently, Cabello [Cab08] and others [BBCP09] used BKS proofs to derive a set of inequalities that are satisfied by any NCHV theory but are violated by quantum mechanics for *any* quantum state. These inequalities bound certain linear combinations of ensemble averages of correlations between measurement outcomes of compatible observables; thus creating a separation between the predicted outcomes of quantum mechanics, and the bound that is satisfied by NCHV theories.

This provides an opportunity to test noncontextuality with finite-precision experiments –which has been the subject of contention for many years [Mey99, Cab02, Mer99]– and without the need for the creation of special quantum states [SŻWZ00, HLZ+03, BKS+09]. Already, two experiments, on [KZG+09] a pair of trapped $^{40}Ca^{+}$ ions, and with single photons [ARBC09], have demonstrated this state-independent conflict with noncontextuality. In this Section, we examine the application of the techniques described in the previous chapters towards the problem of testing contextuality on quantum ensembles.

The rest of the chapter is organized as follows. First, we sketch the arguments

leading to one of the inequalities derived in [Cab08]. Then we present an algorithm to estimate the expectation value of the correlations of measurement outcomes for ensembles of quantum systems. And lastly, we report and discuss the result of experimentally implementing the algorithm.

4.1.2 BKSC Inequality

For a quantum system prepared according to some state, ρ, one can assign simultaneous outcomes $\{\nu(S_k)\}$ of measurements of a set $\{S_k\}$ of *coobservables* (i.e. *co*measureable; mutually *co*mpatible; *co*mmuting). In this case, the correlation between the measurement outcomes is given by

$$\pi_{\{S_k\}} = \prod_k \nu(S_k) = \nu(\prod_k S_k)\,, \tag{4.1}$$

irrespective of the product ordering. Repeating the preparation and measurement many times, and averaging over the outcomes, one obtains an estimate of the ensemble average of the correlation

$$\langle \pi_{\{S_k\}} \rangle_\rho = \langle \prod_k \nu(S_k) \rangle_\rho\,. \tag{4.2}$$

For the case where the coobservables $\{S_k\}$ are also dichotomic, with possible outcomes $\{\nu(S_k) = \pm 1\}$, the correlation (4.1) also takes on the possible values ± 1, and the ensemble average satisfies $-1 \leq \langle \pi_{\{S_k\}} \rangle_\rho \leq +1$. Note, that in this case, these operators are Hermitian and unitary (also known as Quantum Boolean Functions).

Consider *any* set of observables with possible outcomes ± 1 arranged in a 3×3 table such that the observables in each column and each row are coobservable (e.g. as in Table 4.1). It has been shown [Cab08] that, for any NCHV theory,

$$\beta = \langle \pi_{r_1} \rangle + \langle \pi_{r_2} \rangle + \langle \pi_{r_3} \rangle + \langle \pi_{c_1} \rangle + \langle \pi_{c_2} \rangle - \langle \pi_{c_3} \rangle \leq 4\,, \tag{4.3}$$

where $\langle \pi_{r_1} \rangle$ is the ensemble average of the correlation between outcomes of the observables listed in the first row, and so forth. The above inequality is independent of the preparation of the ensemble, provided all terms are estimated for the same preparation.

The inequality is verifiable by considering all possible configurations for the outcomes of all nine measurements. Let $\alpha = \pi_{r_1} + \pi_{r_2} + \pi_{r_3} + \pi_{c_1} + \pi_{c_2} - \pi_{c_3}$. By construction, one can assign simultaneous outcomes to observables listed in the same row or column. Thus, each term in α can be estimated on a single system. For a NCHV theory, each observable listed at the intersection of a column and a

row is assigned the same outcome for the same preparation, whether it is measured in a row or a column. The histogram in Figure 4.1 shows the distribution of α for all possible configurations of outcomes of all nine measurements, showing $\alpha \leq 4$. Hence, the ensemble average, with probablistic mixtures of α(s), has to satisfy $\beta \leq 4$.

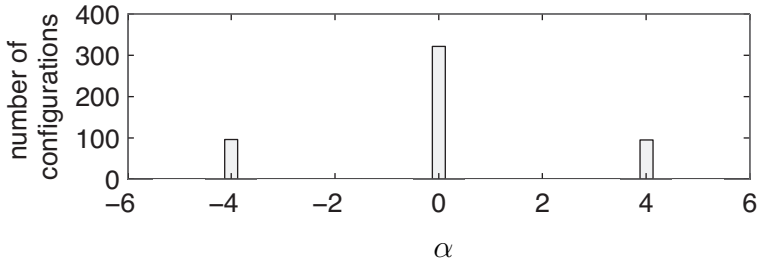

Figure 4.1: A histogram of $\alpha = \pi_{r_1} + \pi_{r_2} + \pi_{r_3} + \pi_{c_1} + \pi_{c_2} - \pi_{c_3}$ for all possible 2^9 configurations of ± 1 outcomes for observables arranged in a 3×3 table as described in the text.

	c_1	c_2	c_3	$\prod$
r_1	$Z\mathbb{1}$	$\mathbb{1}Z$	ZZ	$+\mathbb{1}$
r_2	$\mathbb{1}X$	$X\mathbb{1}$	XX	$+\mathbb{1}$
r_3	ZX	XZ	YY	$+\mathbb{1}$
$\prod$	$+\mathbb{1}$	$+\mathbb{1}$	$-\mathbb{1}$	

Table 4.1: List of the 2-qubit observables used to show that quantum mechanics violates inequality (4.3). This list has been used by Peres [Per90] and Mermin [Mer90] as a BKS proof for 4 dimensional systems. $\{\mathbb{1}, X, Z, Y\}$ are the single qubit Pauli operators, and, e.g. $ZX := Z \otimes X$ indicates a measurement of the Pauli-Z on the first qubit and Pauli-X on the second. The correlation between the outcomes of measurements of the observables in each row and column are indexed by r_i and c_j respectively. For example, the correlation between outcomes of observables listed in the first row, $\langle \pi_{r_1} \rangle = \langle Z\mathbb{1} \cdot \mathbb{1}Z \cdot ZZ \rangle$.

Now, consider a 2-qubit system (e.g. 2 spin-$\frac{1}{2}$ particles), and the set of observables listed in Table 4.1. For any NCHV theory, the inequality (4.3) holds for the correlations between measurement outcomes of the coobservables listed in each row and column, where, for e.g., $\langle \pi_{r_1} \rangle = \langle \pi_{\{Z\mathbb{1},\mathbb{1}Z,ZZ\}} \rangle = \langle Z\mathbb{1} \cdot \mathbb{1}Z \cdot ZZ \rangle$, and so forth.

On the other hand, according to quantum mechanics, the ensemble average $\langle \pi_{\{S_k\}} \rangle_\rho$ is given by $\mathrm{tr}(\rho \prod_k S_k)$. Thus, for a set of coobservables whose product is proportional to the unit operator –as is the case for all rows and columns of Table 4.1– the quantum mechanical prediction of the ensemble average of the correlation is equal to the proportionality constant, independent of the initial preparation of the system. Hence, the quantum mechanical prediction for β is 6, which violates inequality (4.3).

4.1.3 Algorithm

To measure the correlation between a set of coobservables, consider introducing an ancillary (probe) qubit, and applying a transformation U_{S_k} to the composite system for each observable S_k, in a manner reminiscent of coherent syndrome measurement in quantum error correction [DS96]. For an observable S with the spectral decomposition $S = P_+ - P_-$, where P_+ and P_- are the projectors on the $+1$ and -1 eigenspaces of S, the transformation U_S is defined as $U_S = \mathbb{1}_2 \otimes P_+ + Z \otimes P_-$. That is to say, if the system is in a -1 eigenstate of S, apply a phase flip (Pauli-Z) to the probe qubit, and if it is in a $+1$ eigenstate, do nothing. This transformation can also be expressed as a controlled operation dependent on the state of the probe qubit:

$$\begin{aligned} U_S &= \mathbb{1}_2 \otimes P_+ + Z \otimes P_- \\ &= \tfrac{1}{2}(\mathbb{1}_2 + Z) \otimes (P_+ + P_-) + \tfrac{1}{2}(\mathbb{1}_2 - Z) \otimes (P_+ - P_-) \\ &= |0\rangle\langle 0| \otimes \mathbb{1}_d + |1\rangle\langle 1| \otimes S\,, \end{aligned} \tag{4.4}$$

which is unitary for S unitary. If the system is initially prepared according to ρ, and the probe qubit in the $+1$ eigenstate of the Pauli-X operator, $|+\rangle = (|0\rangle + |1\rangle)/\sqrt{2}$, the possible outcomes of Pauli-X measurement on the probe qubit is ± 1, with probabilities $p(\pm 1)$ given by:

$$\begin{aligned} p(+1) =& \mathrm{tr}_{a+s}\left[U_S(|+\rangle\langle+| \otimes \rho)U_S^\dagger\,(|+\rangle\langle+| \otimes \mathbb{1}_d)\right] \\ =& \mathrm{tr}_s\left[\langle+|(\mathbb{1}_2 \otimes P_+ + Z \otimes P_-)(|+\rangle\langle+| \otimes \rho)(...)^\dagger|+\rangle\right] \\ =& \langle+|\mathbb{1}_2|+\rangle\langle+|\mathbb{1}_2|+\rangle\ \mathrm{tr}_s\left[P_+\rho P_+\right] \\ =& \mathrm{tr}_s\left[P_+\rho\ \right]\,, \end{aligned} \tag{4.5}$$

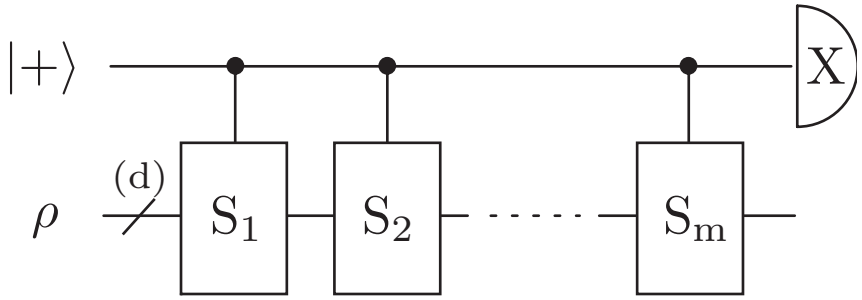

Figure 4.2: A quantum network to encode the correlation between the outcomes of measurements $\{S_k\}_{k=1\ldots m}$ on a d-dimensional system, in the phase of a probe qubit state. Repeating this procedure for the same preparation ρ and averaging the outcome of the measurement on the probe qubit gives the ensemble average $\langle S_1 S_2 \cdots S_m \rangle_\rho$. Alternatively, for an ensemble of quantum systems initially prepared according to ρ, on which operations are applied in parallel to the individual systems, an ensemble measurement readily produces $\langle S_1 S_2 \cdots S_m \rangle_\rho$.

and

$$\begin{aligned} p(-1) =& \mathrm{tr}_{a+s}\left[U_S(|+\rangle\langle+|\otimes\rho)U_S^\dagger\,(|-\rangle\langle-|\otimes\mathbb{1}_d)\right] \\ =& \mathrm{tr}_s\left[\langle-|(\mathbb{1}_2\otimes P_+ + Z\otimes P_-)(|+\rangle\langle+|\otimes\rho)(...)^\dagger|-\rangle\right] \\ =& \langle-|Z|+\rangle\langle+|Z|-\rangle\ \mathrm{tr}_s\left[P_-\rho P_-\right] \\ =& \mathrm{tr}_s\left[P_-\rho\ \right], \end{aligned} \tag{4.6}$$

and the ensemble average

$$\begin{aligned} \langle X\otimes\mathbb{1}_d\rangle &= +p(+1) - p(-1) \\ &= \mathrm{tr}_s\left[P_+\,\rho\,\right] - \mathrm{tr}_s\left[P_-\,\rho\,\right] \\ &= \mathrm{tr}_s\left[S\rho\,\right] \\ &= \langle S\rangle_\rho\,. \end{aligned} \tag{4.7}$$

Thus, to measure the ensemble average of the correlation between a set of coobservables, one prepares a probe qubit in the $+1$ eigenstate of X, and the system according to ρ. As shown in Figure 4.2, one then applies the unitaries S_k in succession to the system, controlled on the state of the probe qubit. Since, by definition, all S_k mutually commute, then the order of their application has no bearing on the measurement outcome. Repeating this procedure, and averaging the outcome of the measurement on the probe system produces the correlation between this set of observables.

Alternatively, one could prepare an ensemble of systems according to ρ; apply the transformations U_S in parallel to each member of the ensemble; and perform

a bulk ensemble measurement to estimate $\langle \pi_{\{S_k\}} \rangle_\rho$. This alleviates the need for isolation of single quantum systems, and the repeated application of single shot, projective measurement.

Since inequality (4.3) is valid for any preparation ρ, then one is free to choose to prepare the system according to the maximally mixed state. In which case, only one qubit –the probe system– is not maximally mixed. This corresponds to the model of computation known as Deterministic Quantum Computation with one qubit (DQC1) [KL98].

4.1.4 Fair Sampling

Suppose the measurement process on the probe qubit was ϵ-efficient, i.e. returning a faithful answer ϵ fraction of the time, and otherwise a uniformly distributed random outcome. The probabilities $p(\pm 1)$ of obtaining outcomes ± 1 will be modified to

$$p(\pm 1) = \tfrac{1-\epsilon}{2} + \epsilon \, \mathrm{tr}_s \left[P_\pm \rho \, \right] , \tag{4.8}$$

and the ensemble average to

$$\langle X \otimes \mathbb{1}_d \rangle = \epsilon \, \langle S \rangle_\rho \, . \tag{4.9}$$

One can then estimate the expectation value $\langle S \rangle_\rho$ under an assumption of fair sampling and knowing the value of ϵ, which can be established from $\epsilon \langle \mathbb{1} \rangle_\rho$.

This model is equivalent to one where the probe system is initially in the mixed state $(1-\epsilon)\frac{\mathbb{1}_2}{2} + \epsilon |+\rangle\langle +|$, provided the reduced dynamics on the probe qubit, from preparation to measurement, is represented by a unital map; i.e. a map that preserves the totally mixed state. To see this, suppose we prepare the probe qubit in some state ρ_a and then apply some transformation to the composite system, whose reduced dynamics on the probe qubit is described by a unital linear map Λ. Using equation (4.8), an ϵ-efficient measurement of $X = |+\rangle\langle +| - |-\rangle\langle -|$ has two possible outcomes ± 1 with probabilities

$$\begin{aligned} p(\pm 1) &= \tfrac{1-\epsilon}{2} + \epsilon \, \mathrm{tr} \left[\, |\pm\rangle\langle\pm| \, \Lambda(\rho_a) \, \right] \\ &= \tfrac{1-\epsilon}{2} \, \mathrm{tr} \left[\, |\pm\rangle\langle\pm| \, \right] + \epsilon \, \mathrm{tr} \left[\, |\pm\rangle\langle\pm| \, \Lambda(\rho_a) \, \right] \\ &= \tfrac{1-\epsilon}{2} \, \mathrm{tr} \left[\, |\pm\rangle\langle\pm| \, \Lambda(\mathbb{1}_2) \, \right] + \epsilon \, \mathrm{tr} \left[\, |\pm\rangle\langle\pm| \, \Lambda(\rho_a) \, \right] \\ &= \mathrm{tr} \left[\, |\pm\rangle\langle\pm| \, \Lambda \left((1-\epsilon)\tfrac{\mathbb{1}_2}{2} + \epsilon \, \rho_a \right) \, \right] , \end{aligned} \tag{4.10}$$

which are precisely the statistics one obtains in case the probe qubit is initially in the state $(1-\epsilon)\frac{\mathbb{1}_2}{2} + \epsilon \, \rho_a$, and the measurement process is faithful.

4.1.5 Experimental Implementation and Results

We implement the algorithm described in Section 4.1.3 to perform an experimental measurement of the correlations as described in inequality (4.3) for the observables listed in Table 4.1. Figure 4.3 shows the six experiments required to estimate the six terms in (4.3). The key point being that the pulse sequence implementing the measurement of some observable is the same whether it is being measured with the coobservables listed in its row or column.

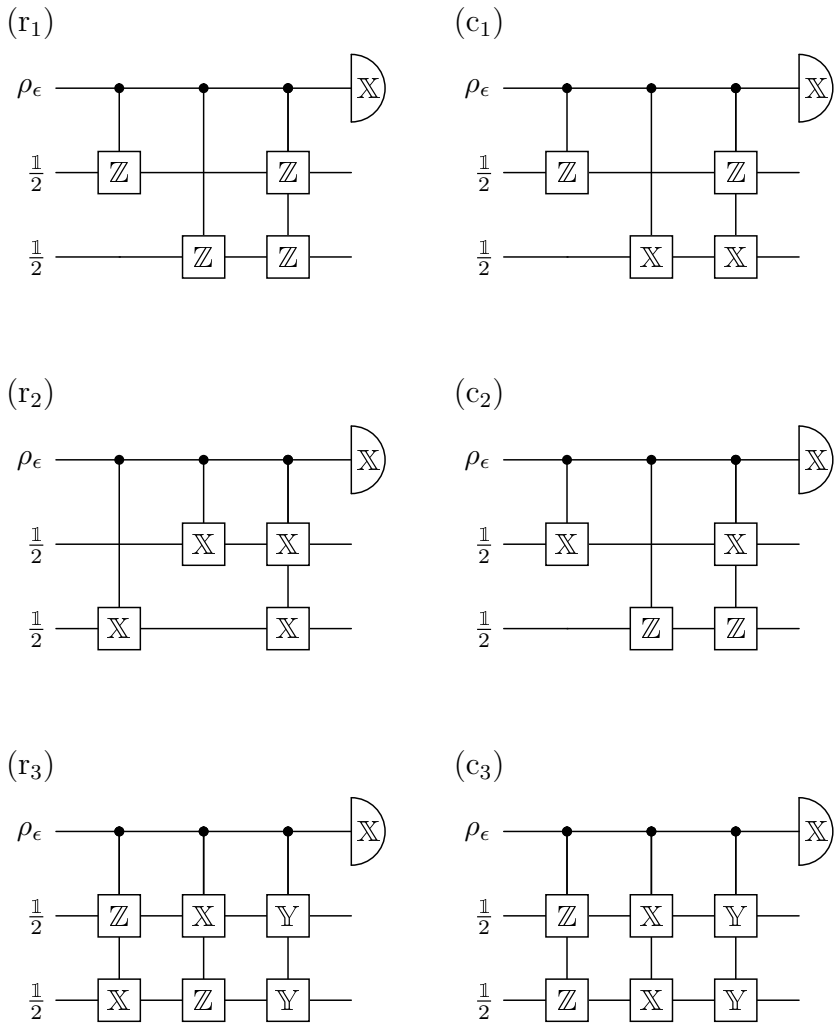

Figure 4.3: The quantum networks for the six experiments to estimate β as given in (4.3). The ensemble is initially prepared according to $\rho_\epsilon \otimes \frac{\mathbb{1}_2}{2} \otimes \frac{\mathbb{1}_2}{2}$, where $\rho_\epsilon = (1-\epsilon)\frac{\mathbb{1}_2}{2} + \epsilon|+\rangle\langle+|$, and $\frac{\mathbb{1}_2}{2}$ is the single-qubit maximally mixed state.

kHz	C_1	C_2	C_m
C_1	6.380	0.297	0.780
C_2	-0.025	-1.533	1.050
C_m	0.071	0.042	-5.650

Table 4.2: Malonic acid ($C_3H_4O_4$) Hamiltonian parameters (all values in kHz). Elements along the diagonal represent chemical shifts with respect to the transmitter frequency. Above the diagonal are dipolar coupling constants , and below are J coupling constants. See Chapter 2 for details of system and Hamiltonian.

The experiment is implemented on the 3-qubit system described in Chapter 2. The Hamiltonian in the particular orientation used in this experiment is shown in Table 4.2, and is extracted from a precise fit of a, proton-decoupled, ^{13}C spectrum. The spectrum and the fit are shown in subfigure (a) of Figure 4.4.

The two spin-$\frac{1}{2}$ nuclei C_1 and C_2, constituting the system on which the measurements are performed, are initially prepared according to the totally mixed state. C_m, representing the probe qubit, is initially prepared according to $\rho_\epsilon = (1-\epsilon)\frac{\mathbb{1}_2}{2} + \epsilon|+\rangle\langle+|$. Figure 4.4 shows the spectrum observed for the initial preparation, as well as the average of the spectra from the six experiments, representing the six terms in β of inequality (4.3) with the appropriate signs. Fitting the observable spectra, taking into consideration the effects of strong coupling, we estimate the value of β to be 5.2 ± 0.1, in violation of inequality (4.3). The uncertainty on β is propagated from the goodness-of-fit figure of merit ascribed to the spectral fitting process.

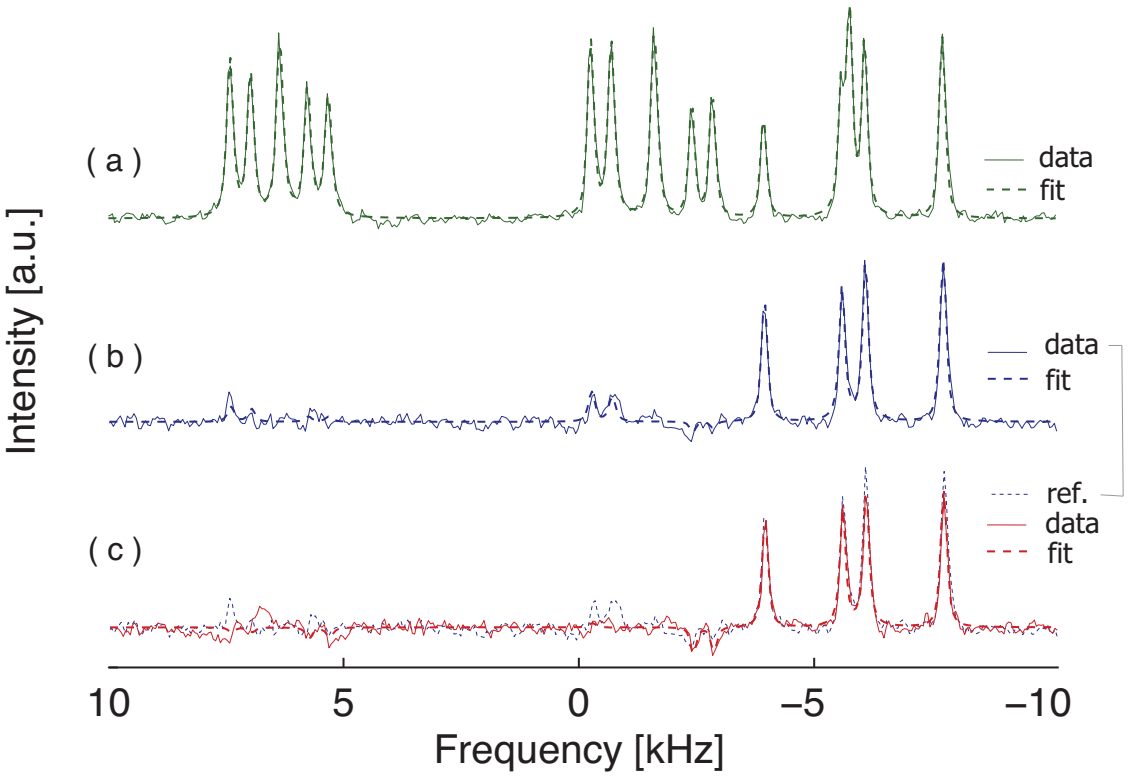

Figure 4.4: Summary of experimental results (solid lines) and the corresponding spectral fits (dashed lines). Shown are (a) (in green) a proton-decoupled ^{13}C spectrum following polarization-transfer from the abundant protons. The central peak in each quintuplet is due to natural abundance ^{13}C nuclei present in the crystal at $\sim 1\%$, and we denote them, from left to right, as C_1, C_2, and C_m (see Figure 2.1 for the labeling of the nuclei.) ; (b) (in blue) the spectrum produced by the initial preparation procedure, $\rho_\epsilon \otimes \frac{\mathbb{1}_2}{2} \otimes \frac{\mathbb{1}_2}{2}$, establishing a reference for ϵ; and (c) and (in red) the sum of the six spectra corresponding to the six terms in β of inequality (4.3) with the appropriate signs, scaled by $\frac{1}{6}$ for ease of comparison with the reference. Comparing the final spectrum (c) to the reference spectrum (b) produces a value of $\beta = 5.2 \pm 0.1$

4.1.6 Simulating decoherence

Decoherence, as it is wont to do, causes deviations from the idealized closed-system dynamics. To examine its effect, we numerically simulate the dynamics of a simple model (shown in Figure 4.5) in which each ideal transformation is followed by an error of a three-fold tensor product of single-qubit dephasing maps, $\Lambda(\rho)$, given by the operator sum representation

$$\rho \to \Lambda(\rho) = \sum_{\kappa} A_\kappa \rho A_\kappa^\dagger \,, \tag{4.11}$$

where

$$A_0 = \begin{pmatrix} 1 & 0 \\ 0 & \sqrt{1-\eta} \end{pmatrix} \,, \; A_1 = \begin{pmatrix} 1 & 0 \\ 0 & \sqrt{\eta} \end{pmatrix} \,, \tag{4.12}$$

and the parameter $\eta = 1 - \exp\left(-t/T_2\right)$ depends on the ratio of the pulse-length, t, to an effective dephasing time, T_2. Figure 4.5 shows that the dephasing of the probe qubit is most critical in observing the effect. Using appropriate estimates [BMR+06] of this dephasing time, one is able to largely explain the deviation of the experimental result from the prediction of quantum mechanics in ideal conditions, as shown in Figure 4.6.

4.1.7 Summary

We have presented a protocol to directly measure correlations between measurement outcomes, utilizing an ancillary (probe) two dimensional system, with the purpose of testing quantum contextuality. Conveniently, it can be used directly on ensembles of quantum systems, without the need for repeated projective measurement on single systems. Additionally, it can be straightforwardly extended to test similar inequalities on higher-dimensional systems. Our experimental results demonstrate –under the assumption of fair sampling– that a three-qubit deterministic quantum computer with one qubit reveals correlations between measurement outcomes that cannot be explained by any NCHV theory.

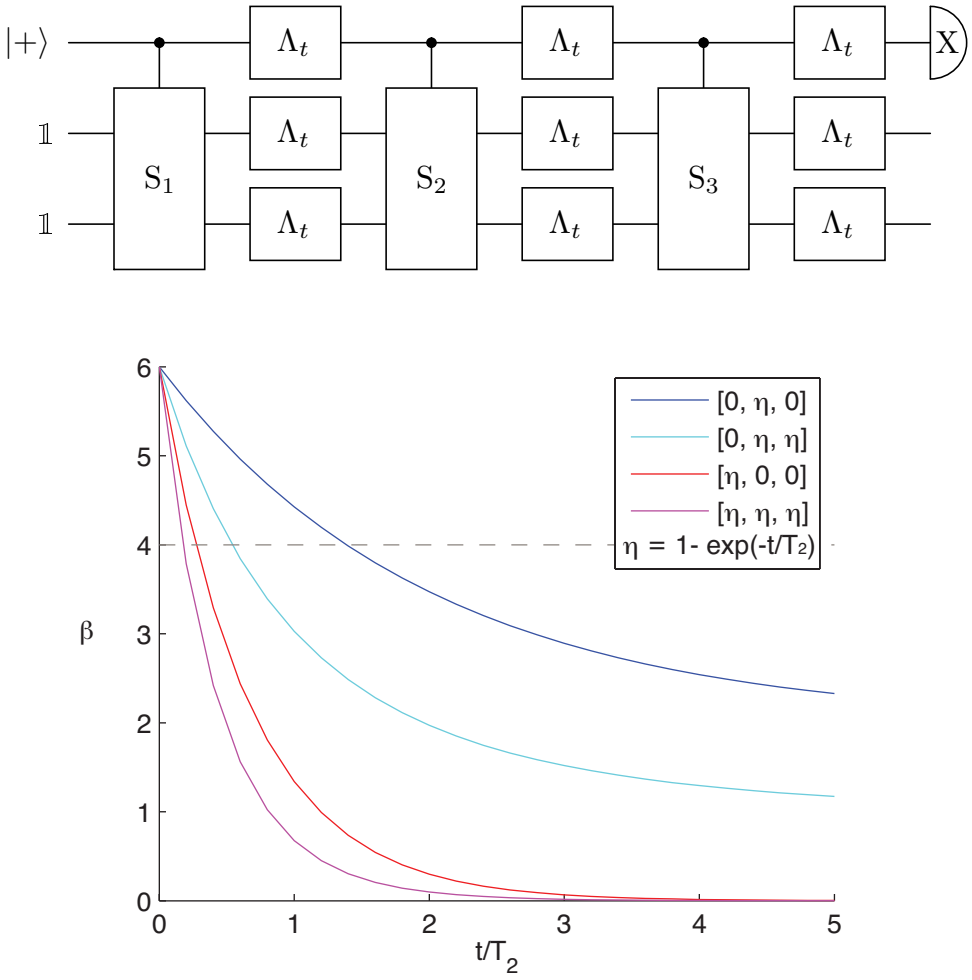

Figure 4.5: Numerical simulation results of a simple model of decoherence (inset) showing the expected variation of β as a function of the ratio of the pulse-length, t, to an effective dephasing time, T_2. The different curves are for different simulations. For example, the blue curve is for a simulation where only the second qubit was affected by the dephasing map. And so on. The dashed line indicates the bound on NCHV theories.

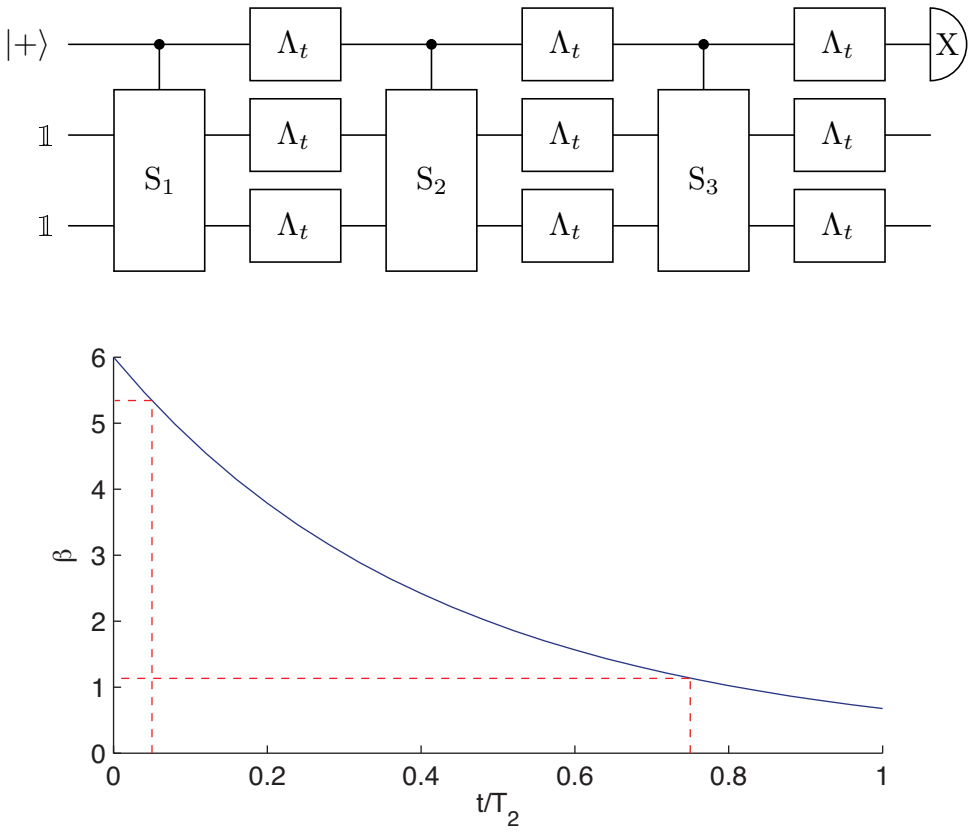

Figure 4.6: Numerical simulation results of a simple model of decoherence (inset) showing the expected variation of β as a function of the ratio of the pulse-length, t, to an effective dephasing time, T_2. The dashed lines indicate bounds on the expected performance of the current experiment; for pulse length of 1.5ms, and effective decoherence times of 2ms ($\sim T_2^*$) and 30ms ($\sim$ intrinsic coherence times [BMR+06]), the value of β is expected to be 1.1 and 5.3 respectively.

Chapter 5

Conclusions and outlook

Quantum Information processing (QIP) has the potential to revolutionize information processing by providing –for some problems– more efficient solutions than the best known classical algorithms. The quest is on to examine if there is, in principle, any roadblocks to the realization of quantum information devices on a large scale. All at the same while, a lot of effort is directed towards the improvement of the fidelity of control of small systems, as well as interesting questions relating to applications of small system quantum information processing.

Liquid state NMR has been one of the most successful implementations of QIP to date; in terms of the quality of control, the size of the quantum system manipulated, and the coherence times exhibited. However, it has also attracted certain criticism, mainly due to the highly mixed nature of the states manipulated in that architecture, and the inability to perform single shot measurement. The extension of liquid state NMR ideas to the solid state promises to circumvent at least the former of these problems. This is due to the ability to cool solid state systems to low temperatures thereby decreasing the thermal energy available to the spins; the observation of high nuclear polarization in solids after polarization transfer from electrons; as well as the presence of fast relaxing spin baths in the form of dipolar networks, which would facilitate a fresh supply of ancillas for quantum error correction. In addition, the survival of the stronger dipolar couplings in the solid state, coupled with the long intrinsic coherence times lead to faster multiqubit gates and lower error rates per gate due to decoherence.

The work in this thesis has promoted one particular device architecture that employs the magnetic resonance of an ensemble of molecular nuclei in a single crystal solid. We have shown that, in the strong coupling regime; we are able to achieve high fidelity control of small systems; we are able to prepare pseudo-pure states and improve their purity using heat-bath algorithmic cooling; we are able to show practical advantage from using quantum error correction to protect against

phase noise; and that the quality of control is sufficient to implement two rounds of error correction.

Pertaining to quantum control, we have confirmed the intuition that, in practice, tailoring pulses to have power and bandwidth limits that respect the resonant circuit's response enhances our ability to control the system. We have also observed that classical feedback –even the most straight forward of approaches, in which an antenna measures the driving fields in the vicinity of the sample– improves the quality of control significantly.

The methods of control and characterization, as described in Chapter 2 of this thesis, involve full simulations of the quantum dynamics over the entire Hilbert space of the computational register, and therefore do not scale favourably. As we move towards bigger systems, it is not clear whether this limitation can be overcome in principle without altering the architecture. In practice, I suspect that a strongly coupled network of eight spins or more is infeasible without improving the efficiency of the current methods.

One possible direction for improvement is to use the quantum device itself to simulate the evolution under given control fields. And, provided there is an efficient way to measure how well the actuated evolution compares to a desired one (which is currently not known to exist except if the desired evolution is the Identity) one can imagine varying the controls intelligently to maximize that measure. This would have the added benefit that the optimization of the control pulses is performed in the same circumstances that would be present during their application in an algorithm.

Another scheme, which has shown promise in liquid state NMR [RNL+08, Rya09], involves decomposing the system into subsystems that capture the dominant dynamics, and then simulating pairs of subsystems at a time to get rid of any extraneous evolution. The success of such schemes is system dependent since the coupling networks between the spins have to satisfy certain (physically reasonable) constraints.

Yet another attractive idea takes advantage of highly symmetric geometric arrangements of spins, e.g. in one dimensional chains [FXBJ07], and employs global control to perform universal quantum information processing. This would circumvent the scalability problem of pulse-design altogether, but at the moment it is not clear whether these schemes permit a fault tolerant implementation.

As for the promise of high polarization, we have taken a number of concrete steps to demonstrate that the current level of control is sufficient to implement heat bath algorithmic cooling fiducially for multiple rounds to incrementally increase the polarization of one of the computationally active qubits (see Section E.1). For the model of heat bath algorithmic cooling in which one spin is brought to contact

with the spin bath at opportune times, one distinguishes two regimes – where the heat bath spin polarization is much larger than or much smaller than $\frac{1}{2^n}$. In the former, low temperature regime, algorithmically, one can get very close to pure states. On the other hand, in the high temperature regime, the maximum achievable polarization is 2^{n-2} times the heat bath polarization.

In our experiments, with three qubits at room temperature, where the maximum achievable polarization of one qubit is twice that of the heat bath, we have accumulated 1.7 times the heat bath polarization in multiple rounds of algorithmic cooling. In these experiments, the carbon spins of Malonic acid formed the computational register, while the abundant protons served as the spin bath. The transfer of polarization from one of the mythelene protons to one of the carbon spins constituted the heath bath contact, and spin diffusion via the dipolar coupling of the proton spins refreshed the heat bath between the contact operations.

In future experiments, we imagine using electron spins as the source of polarization. The thermal bias of electron spins at cryogenic temperatures and typical fields of a few Tesla is sufficient to place the experiments in the regime where it is possible to boost the polarization of nuclear spins to approach unity. As it stands, boosting the polarization in the high temperature regime is already of practical importance as it reduces the time required to average the signal for good statistics. It is perhaps appropriate at this point to mention that the practicality of signal averaging is hindered mostly by long relaxation times of the polarization source, which, in this case, is the proton bath.

In Chapter 3, we demonstrated the advantage of performing quantum error correction to protect against phase errors –coherent, incoherent and decoherent– that arise naturally in the solid-state NMR system. We have shown that this is possible with the quality of control currently available. Moreover, we have shown that two rounds are also possible with current control levels. In addition to existing methods like decoupling and refocusing, this is a valuable tool in the fight against decoherence.

For this program, the next major milestone on the road to truly useful quantum information processing devices is to combine the techniques of quantum error correction with algorithmic cooling, in the low temperature regime, perhaps in a system with a few more distinguishable spins.

The lessons learnt from NMR as a testbed for ideas of quantum information processing are already being applied in other implementations (e.g. superconducting qubits.) This work expands the region of feasibility of these ideas to include the strong coupling regime.

Along the way, the current work implicitly affirms the stance that ideas from Quantum Information Processing will help (directly and indirectly) shed some light

on the fundamental questions of Physics.

In Section 4.1, the main question at hand is whether nature is fundamentally contextual; that is to say, whether the outcome of some measurement depends on the context in which it is measured. A number of recent results have tackled this question in different settings, and herein we have addressed an important, hitherto unexplored, piece of the puzzle; proposing and demonstrating a protocol to experimentally test contextuality without recourse to the isolation of individual quantum systems nor strong measurement.

Moreover, the work presented in this thesis adds an important contribution to the crucial question of the source of speed up in quantum computing. Whilst it is commonly assumed that entanglement is a key resource, the deterministic model of quantum computation with one qubit (DQC1) is a computational model that shows a quantum advantage where the role of entanglement is questioned. Demonstrating that quantum contextuality can be revealed using a DQC1 model, as reported in Section 4.1, stresses the role of the dynamics in providing this quantum speed up.

Appendix A

Weak and strong coupling

In this appendix, we motivate the NMR spectrum observed for the physical system described in Secition 2.3.2.

A.0.8 Hamiltonian

First, consider the internal-spin hamiltonian, $\mathcal{H}^{jk}$, of two homonuclear spins with chemical shift frequencies of ν_j and ν_k in the rotating frame, interacting via the dipolar coupling given in Equation (2.9). The matrix representation of the Hamiltonian in the Zeeman bases is

$$\begin{aligned}\mathcal{H}^{jk} &= \nu_j Z_j + \nu_k Z_k + d_{jk}(2Z_jZ_k - X_jX_k - Y_jY_k) \\ &= \frac{1}{2}\begin{pmatrix} \nu_\Sigma + d_{jk} & & & \\ & \nu_\Delta - d_{jk} & -d_{jk} & \\ & d_{jk} & -\nu_\Delta - d_{jk} & \\ & & & -\nu_\Sigma + d_{jk} \end{pmatrix},\end{aligned} \tag{A.1}$$

where $\nu_\Sigma = \nu_j + \nu_k$ and $\nu_\Delta = \nu_j - \nu_k$. The eigenvalues of this hamiltonian are solutions to the characteristic equation given by $\det(\mathcal{H}^{jk} - \lambda_n \mathbb{1}) = 0$. Two eigenvalues are obvious,

$$\lambda_{\substack{4\\1}} = \frac{1}{2}(\pm\nu_\Sigma + d_{jk}), \tag{A.2}$$

corresponding to the eigenvectors:

$$|v_4\rangle = \begin{pmatrix} 1 \\ 0 \\ 0 \\ 0 \end{pmatrix}, \text{ and } \; |v_1\rangle = \begin{pmatrix} 0 \\ 0 \\ 0 \\ 1 \end{pmatrix}. \tag{A.3}$$

Thus, the characteristic equation reduces to:

$$\frac{1}{2}\begin{vmatrix} \nu_\Delta - d_{jk} - 2\lambda & -d_{jk} \\ -d_{jk} & -\nu_\Delta - d_{jk} - 2\lambda \end{vmatrix} = 0\,, \tag{A.4}$$

which is a quadratic equation, whose solutions are the other two eigenvalues:

$$\lambda_{\substack{2\\3}} = \frac{1}{2}\left(-d_{jk} \pm \sqrt{d_{jk}^2 + \nu_\Delta^2}\right). \tag{A.5}$$

The eigenvectors, $|v_{\substack{2\\3}}\rangle$, corresponding to $\lambda_{\substack{2\\3}}$ are the null spaces of $\mathcal{H}^{jk} - \lambda_{\substack{2\\3}}\mathbb{1}$. Thus, we wish to solve:

$$\begin{aligned}\begin{pmatrix}0\\0\end{pmatrix} &= \frac{1}{2}\begin{pmatrix} \nu_\Delta - d_{jk} - (-d_{jk} \pm \sqrt{d_{jk}^2 + \nu_{jk}^2}) & -d_{jk} \\ -d_{jk} & -\nu_\Delta - d_{jk} - (-d_{jk} \pm \sqrt{d_{jk}^2 + \nu_{jk}^2}) \end{pmatrix} |v'_{\substack{2\\3}}\rangle \\ &= \frac{1}{2}\begin{pmatrix} \nu_\Delta \mp \sqrt{d_{jk}^2 + \nu_{jk}^2}) & -d_{jk} \\ -d_{jk} & -\nu_\Delta \mp \sqrt{d_{jk}^2 + \nu_{jk}^2}) \end{pmatrix} |v'_{\substack{2\\3}}\rangle\,. \end{aligned} \tag{A.6}$$

Making the substitution:

$$\tan\phi = \frac{-d_{jk}}{\nu_\Delta} \tag{A.7}$$

reduces Equation (A.6) to:

$$\begin{aligned}\begin{pmatrix}0\\0\end{pmatrix} &= \frac{1}{2}\sqrt{d_{jk}^2 + \nu_\Delta^2}\begin{pmatrix} \cos\phi \mp 1 & \sin\phi \\ \sin\phi & -\cos\phi \mp 1 \end{pmatrix} |v'_{\substack{2\\3}}\rangle \\ &= \frac{\sin\phi}{2}\sqrt{d_{jk}^2 + \nu_\Delta^2}\begin{pmatrix} \frac{\cos\phi\mp 1}{\sin\phi} & 1 \\ 1 & \frac{-\cos\phi\mp 1}{\sin\phi} \end{pmatrix} |v'_{\substack{2\\3}}\rangle \\ &= \frac{\sin\phi}{2}\sqrt{d_{jk}^2 + \nu_\Delta^2}\begin{pmatrix} \frac{-\tan\phi/2}{\cot\phi/2} & 1 \\ 1 & \frac{-\cot\phi/2}{\tan\phi/2} \end{pmatrix} |v'_{\substack{2\\3}}\rangle. \end{aligned} \tag{A.8}$$

Therefore, the eigenvectors, $|v_{\substack{2\\3}}\rangle$, are:

$$|v_2\rangle = \begin{pmatrix} 0 \\ \cos\frac{\phi}{2} \\ \sin\frac{\phi}{2} \\ 0 \end{pmatrix}, \text{ and } \; |v_3\rangle = \begin{pmatrix} 0 \\ -\sin\frac{\phi}{2} \\ \cos\frac{\phi}{2} \\ 0 \end{pmatrix}. \tag{A.9}$$

A.0.9 Spectra

The observable (-)single-quantum-transitions operator is given by:

$$I_-^j + I_-^k = \begin{pmatrix} 0 & 0 \\ 1 & 0 \end{pmatrix} \otimes \begin{pmatrix} 1 & 0 \\ 0 & 1 \end{pmatrix} + \begin{pmatrix} 1 & 0 \\ 0 & 1 \end{pmatrix} \otimes \begin{pmatrix} 0 & 0 \\ 1 & 0 \end{pmatrix} = \begin{pmatrix} 0 & 0 & 0 & 0 \\ 1 & 0 & 0 & 0 \\ 1 & 0 & 0 & 0 \\ 0 & 1 & 1 & 0 \end{pmatrix}, \quad \text{(A.10)}$$

which has the following form in the eigenbasis of the Hamiltonian:

$$\begin{aligned} M_- &= \sum_{n,m} \langle v_n | I_-^j + I_-^k | v_m \rangle | \nu_n \rangle\langle \nu_m | \\ &= \begin{pmatrix} & & & 1 \\ & \cos\frac{\phi}{2} & \sin\frac{\phi}{2} & \\ & -\sin\frac{\phi}{2} & \cos\frac{\phi}{2} & \\ 1 & & & \end{pmatrix} \begin{pmatrix} 0 & 0 & 0 & 0 \\ 1 & 0 & 0 & 0 \\ 1 & 0 & 0 & 0 \\ 0 & 1 & 1 & 0 \end{pmatrix} \begin{pmatrix} & & & 1 \\ & \cos\frac{\phi}{2} & -\sin\frac{\phi}{2} & \\ & \sin\frac{\phi}{2} & \cos\frac{\phi}{2} & \\ 1 & & & \end{pmatrix} \\ &= \begin{pmatrix} 0 & \cos\frac{\phi}{2} + \sin\frac{\phi}{2} & \cos\frac{\phi}{2} - \sin\frac{\phi}{2} & 0 \\ & & & \cos\frac{\phi}{2} + \sin\frac{\phi}{2} \\ & & & \cos\frac{\phi}{2} - \sin\frac{\phi}{2} \\ & & & 0 \end{pmatrix}, \end{aligned} \quad \text{(A.11)}$$

giving only four transitions with non-zero amplitude, whose frequencies are given by the difference between the eigenvalues labeling the transition:

$$\begin{aligned} \sigma_{\substack{43 \\ 42}} &= \lambda_4 - \lambda_{\substack{3 \\ 2}} \\ &= \frac{1}{2}(\nu_\Sigma + d_{jk}) - \frac{1}{2}\left(-d_{jk} \mp \sqrt{d_{jk}^2 + \nu_\Delta^2}\right) \\ &= \frac{\nu_\Sigma}{2} + d_{jk} \pm \frac{1}{2}\sqrt{d_{jk}^2 + \nu_\Delta^2}, \text{ and} \\ \sigma_{\substack{21 \\ 31}} &= \lambda_{\substack{2 \\ 3}} - \lambda_1 \\ &= \frac{1}{2}\left(-d_{jk} \pm \sqrt{d_{jk}^2 + \nu_\Delta^2}\right) - \frac{1}{2}(-\nu_\Sigma + d_{jk}) \\ &= \frac{\nu_\Sigma}{2} - d_{jk} \pm \frac{1}{2}\sqrt{d_{jk}^2 + \nu_\Delta^2}. \end{aligned} \quad \text{(A.12)}$$

If the (-)single-quantum-coherences are equally excited, say by tipping the thermal polarization along the x-direction, then the observed signal will have four peaks,

with intensities

$$\begin{aligned} s_{\substack{42,21\\43,31}} &= (\cos\frac{\phi}{2} \pm \sin\frac{\phi}{2})^2 \\ &= 1 \pm 2\cos\frac{\phi}{2}\sin\frac{\phi}{2} \\ &= 1 \mp \frac{d_{jk}}{\sqrt{d_{jk}^2+\nu_\Delta^2}}\,. \end{aligned} \tag{A.13}$$

Perhaps this is a good spot to make the following remark. It might seem from Eq. (A.13) that one can extract the sign of the coupling from the peak heights. Alas, Eq. (A.12) shows that when the coupling switches sign, so do the peaks' relative positions, resulting in the outer peak always having higher intensity regardless of the sign of the coupling.

For non-interacting spins, i.e. for $d_{jk} = 0$, we recover the two peaks –with equal intensity– at the chemical shift frequencies of the two spins:

$$\sigma_{\substack{43,21\\42,31}} = \frac{1}{2}(\nu_\Sigma \pm \nu_\Delta) = \nu_{\substack{j\\k}}\,. \tag{A.14}$$

In the weak regime, $d_{jk} << \nu_\Delta$, the transition frequencies are:

$$\begin{aligned} \sigma^w_{\substack{43\\21}} &= \nu_j \pm d_{jk}\,, \text{ and} \\ \sigma^w_{\substack{42\\31}} &= \nu_k \pm d_{jk}\,, \end{aligned} \tag{A.15}$$

and the corresponding peak heights are approximately

$$s_{\substack{42,21\\43,31}} = 1 \mp \frac{d_{jk}}{\nu_\Delta}\,. \tag{A.16}$$

Again, there is a doublet separated by $2d_{jk}$ but in the case of the strong coupling there is a second order chemical shift. The correction term is:

$$\begin{aligned} \sigma_{\substack{43,21\\42,31}} - \sigma^w_{\substack{43,21\\42,31}} &= \frac{\nu_\Sigma}{2} \pm \frac{1}{2}\sqrt{d_{jk}^2+\nu_\Delta^2} - \nu_{\substack{j\\k}} \\ &= \frac{1}{2}\left(\nu_\Sigma \pm \sqrt{d_{jk}^2+\nu_\Delta^2}\right) - \nu_{\substack{j\\k}} \\ &= \frac{1}{2}\left(\nu_\Sigma \pm \nu_\Delta\sqrt{\frac{d_{jk}^2}{\nu_\Delta^2}+1}\right) - \nu_{\substack{j\\k}} \\ &\approx \frac{1}{2}\left(\nu_\Sigma \pm \nu_\Delta(\frac{d_{jk}^2}{2\nu_\Delta^2}+1)\right) - \nu_{\substack{j\\k}} \\ &\approx \pm\frac{1}{4}\frac{d_{jk}^2}{\nu_\Delta}\,, \end{aligned} \tag{A.17}$$

showing that the two doublets are "moving away" from each other. Figure A.1 illustrates this point visually. This shift is quite substantial (e.g. for $\nu_\Delta = 10$kHz and $d_{jk} = 1$kHz, shift$\approx \frac{1}{40} d_{jk} = 25$ Hz) and is therefore important to account for when determining the system's Hamiltonian.

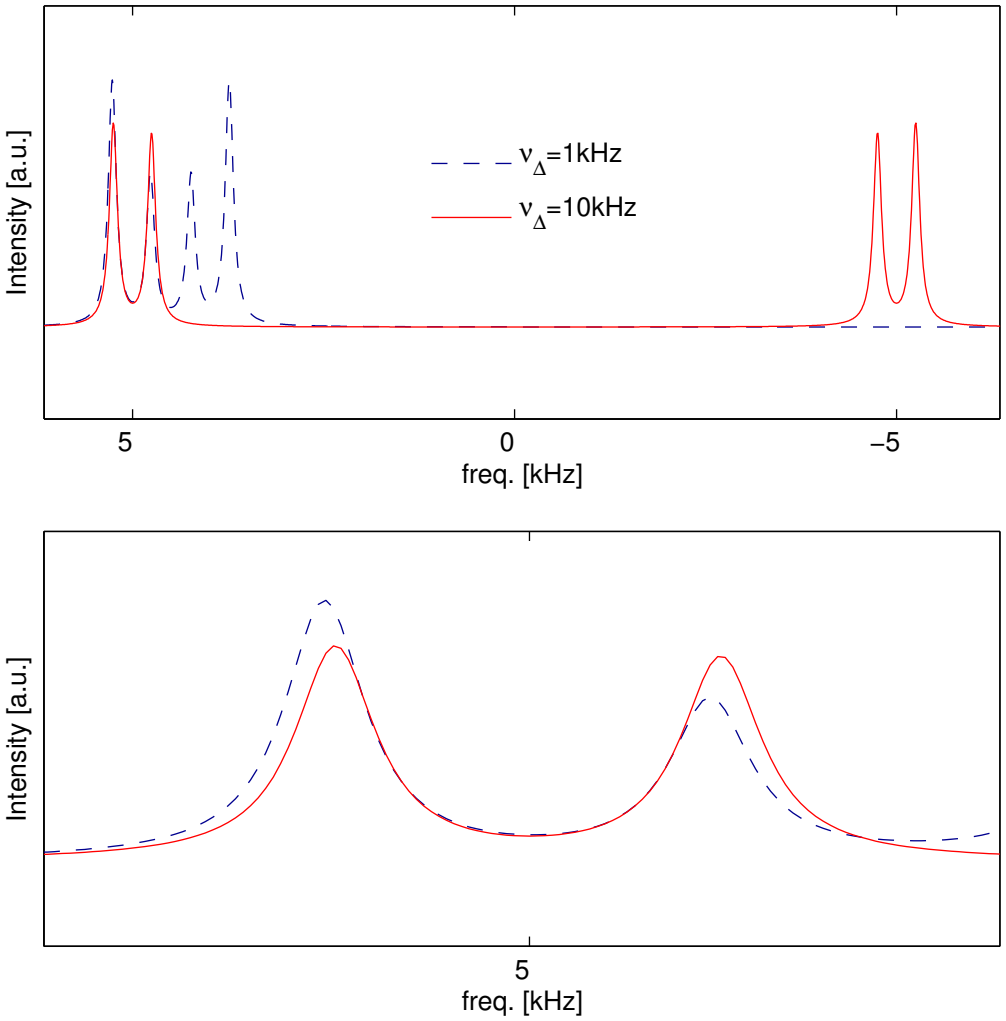

Figure A.1: Shown are the spectra of two spins interacting via a dipolar coupling of strength of 250Hz, where their chemical shift difference is 1kHz (dashed blue) and 10kHz (solid red.) The "tent" effect from strong coupling is apparent in the differential peak heights. The bottom panel zooms in on the two leftmost peaks to illustrate the second order shift due to the strong coupling – the two peaks corresponding to the situation where the spins have only 1kHz apart are shifted "outwards" towards higher frequency with respect to the weak regime situation.

Extending the above treatment to 3 spins with different chemical shifts interacting via the dipolar coupling, we find that the transitions of each spin will correspond to a quartet of peaks centered about their respective chemical shift frequencies. If the couplings vanish (i.e. non-interacting spins), we recover the three single peaks at the positions of the chemical shifts.

For the crystal described in Chapter 2, the NMR spectrum is a linear combination of the spectra described for the above two cases; the ^{13}C triply-labeled molecules would produce a spectrum with the 3 quartets, while the natural abundance ^{13}C nuclei, being dispersed in the crystal would most likely not have a ^{13}C nucleus as their neighbor on the same molecule, and therefore would produce the 3 singlets spectrum.

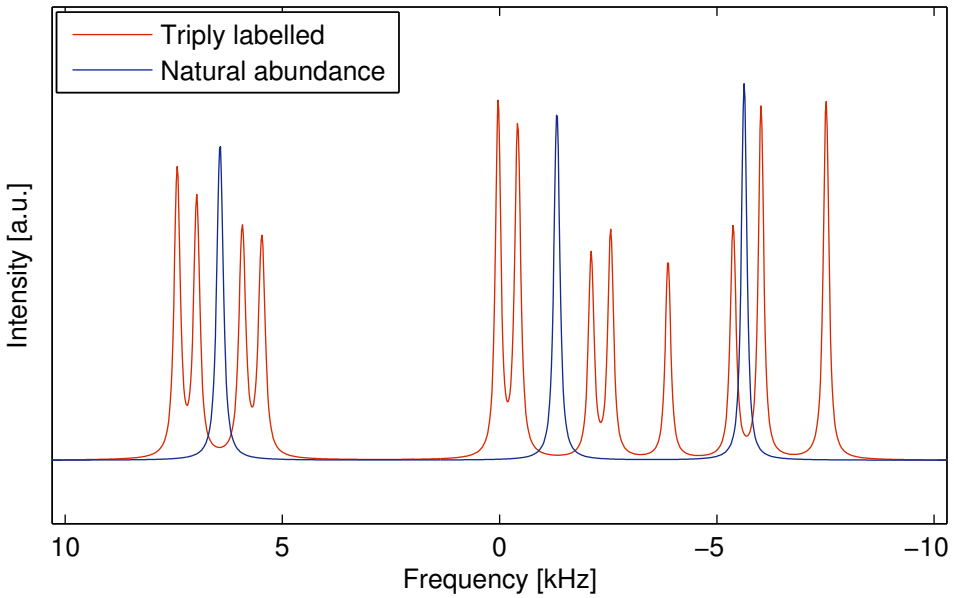

Figure A.2: The contributions to the thermal spectrum from triply labeled and natural abundance signals.

Appendix B

Molecular Orientation: a software package

The NMR Hamiltonian of a network of spins in the solid-state, as detailed in Chapter 2, is anisotropic, with chemical shifts and dipolar couplings varying up to tens of kHz over possible orientations. For small and medium sized unit cells, say containing 5, 10 or 20 spins, the number of parameters characterizing the Hamiltonian –in the absence of some simplifying symmetry, etc.– will increase dramatically. This provides a need for a tool to visualize the Hamiltonian (parameters) as the orientation varies.

In response, I have written an application with a graphical user interface (GUI) that can be employed to various ends:

- Quickly surveying the possible Hamiltonians of prospective candidate systems.
- Locating an orientation with a favorable Hamiltonian for a particular demonstration or experiment.
- Simultaneously visualizing a large number of Hamiltonian parameters, as well as tracking their changes.
- Quickly finding the Hamiltonian for given a particular orientation of the crystal, in an intuitive way.

The application is cross-platform, as it is written in Python, employing the graphical libraries PyQt4 and matplotlib, as well as numpy and scipy for numerics. A screenshot of the GUI is shown in Figure B.1. The typical format of an input file that contains the geometry is shown in Section B.2.

B.1 Graphical User Interface

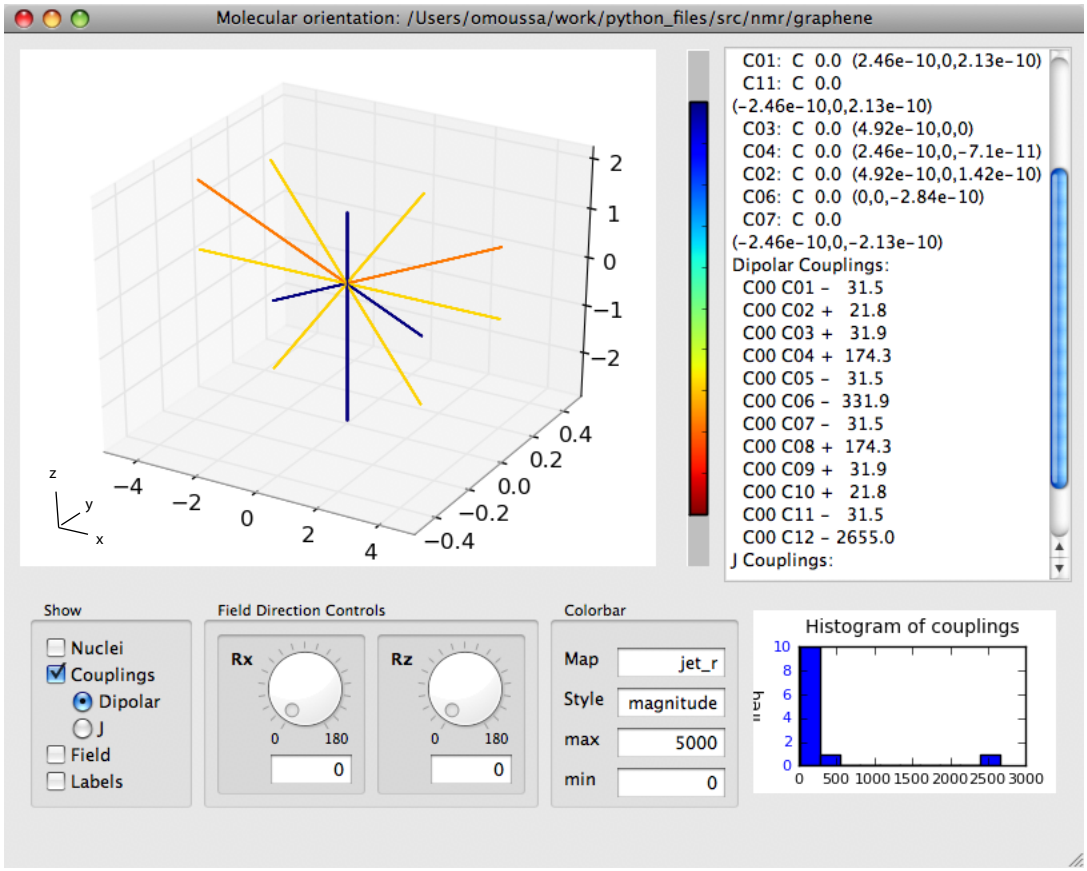

Figure B.1: Screen shot of the Graphical User Interface on Mac OS X 10.4. The knobs allow the user to rotate the field, and the 3D panel shows the chosen parameters color coded per the shown colorbar. The color-maps and the limits can be changed to reflect the choice of finer or coarser graduation. The southeast panel can show statistical information in a number of options. The text panel (northeast) shows precise computed values for the Hamiltonian parameters in the current orientation for closer inspection. The particular information shown here is for the dipolar couplings of a "unit-cell" of graphene, showing couplings between the center Carbon nucleus and the nearest 12 Carbons. The geometry is imported from (exported to) an ascii file as the one listed in Section B.2.

B.2 Geometry file for graphene

```
Nuclei:
  C10:  C  0.0  (-4.92e-10,0,1.42e-10)
  C11:  C  0.0  (-2.46e-10,0,2.13e-10)
  C08:  C  0.0  (-2.46e-10,0,-7.1e-11)
  C09:  C  0.0  (-4.92e-10,0,0)
  C12:  C  0.0  (0,0,1.42e-10)
  C00:  C  0.0  (0,0,0)
  C01:  C  0.0  (2.46e-10,0,2.13e-10)
  C02:  C  0.0  (4.92e-10,0,1.42e-10)
  C03:  C  0.0  (4.92e-10,0,0)
  C04:  C  0.0  (2.46e-10,0,-7.1e-11)
  C05:  C  0.0  (2.46e-10,0,-2.13e-10)
  C06:  C  0.0  (0,0,-2.84e-10)
  C07:  C  0.0  (-2.46e-10,0,-2.13e-10)
Dipolar Couplings:
  C00 C01 -   31.5
  C00 C02 +   21.8
  C00 C03 +   31.9
  C00 C04 +  174.3
  C00 C05 -   31.5
  C00 C06 -  331.9
  C00 C07 -   31.5
  C00 C08 +  174.3
  C00 C09 +   31.9
  C00 C10 +   21.8
  C00 C11 -   31.5
  C00 C12 - 2655.0
J Couplings:
  C00 C04 + 0.0
  C00 C08 + 0.0
  C00 C12 + 0.0
```

Appendix C

Coil Design

Motivating the need for good homogeneity of R.F. fields throughout the sample is hardly necessary – It is important for the spins throughout the sample to see approximately the same field, so they will act out the same evolution. Even though in the current pulse design tools, robustness to slight variations in the R.F. fields is built-in, it is taxing to the design resources and the range over which the pulses can be made robust is obviously finite.

One way to ensure high homogeneity is to include it as a design criterion for the coil that produces the field. Our zeroth order approach was to represent the solenoid coil by a number of current rings and simulate the field in the imagined sample space. An optimization of the *loops' locations and radii* was performed over the distribution of the fields in the sample, favouring highly modal distributions.

The code is a simple standalone MATLAB program that is quite flexible with the design and optimization parameters (and is available upon request from the author or his supervisor.) Following is a –well documented, and hence self-explanatory– sample parameter file. For the particular chosen parameters, the solution is represented in Figures C.1 and C.2 of Section C.2.

C.1 Code

```
function input_params()
%%% This function sets up the parameters needed for coil design

global mu I;
global ktw kLmin kLmax kRmin kRmax nl kpx kpr kWr kdBovB;
global bPlotHist bPlotField bPlotLoops;
global opts firstEst;

%constants
```

```
mu=1.26e-6;%H/m
I=5;%Amps-change if you want;

%coil dimensions (in m)
ktw= .5e-3;   %wire thickness (m)
kLmin= 5e-3;  %minimum length of coil (m)
kLmax= 14e-3; %maximum

kRmin= 1.5e-3; %minimum inner radius
kRmax= 2.0e-3; %maximum; set same as min if no variability desired

nl=7; %number of loops

%remember:
%loop location.. lx=ax*dx+bx*dx.^3+cx*dx.^5;
%radius distribution.. Rx=ar+br*lx.^2+cr*lx.^4;

%Initial starting point
%[first nl/2 params are for location, rest are for radii ...]
firstEst=[6 3 1 0 0 0];

%sample dimensions (in m) this is the actual volume
%over which the magnetic field is calculated.
%--radial--
rmin = 0;     %actually for r=0, the field-values sorta don't
              %matter because we weight the values by r
rmax = 1.2e-3;  %should be less than kRmin-ktw/2
rgrid= 0.025e-3; % radial grid spacing

%--axial--
xmin = -2e-3;  % should be within the coil.. take it to be ~ sample size
xmax = +2e-3;  %+/- kLmin/2
xgrid= +.025e-3; % axial grid spacing

%--grid--
kpx=xmin:xgrid:xmax;
kpr=rmin:rgrid:rmax;

%weight by r
kWr=kpr'; %transpose
for (j=2:length(kpx))
    kWr=[kWr kpr'];
end
kWr=kWr./sum(sum(kWr));

%opimization parameters
kdBovB=.01; % +/- percent of mean field to sum over

opts=optimset(optimset('fminsearch'), ...
  'MaxFunEvals', 1e9, 'TolFun', 1.0e-5, 'TolX', 1.0e-1);

%plotting options (0: don't Plot, 1: Plot, 2:special option ;) )
bPlotField=1; %3-D plot of field
bPlotHist =2; %Plot of dN vs B
bPlotLoops=1; %Plot of loop distribution
```

C.2 Results

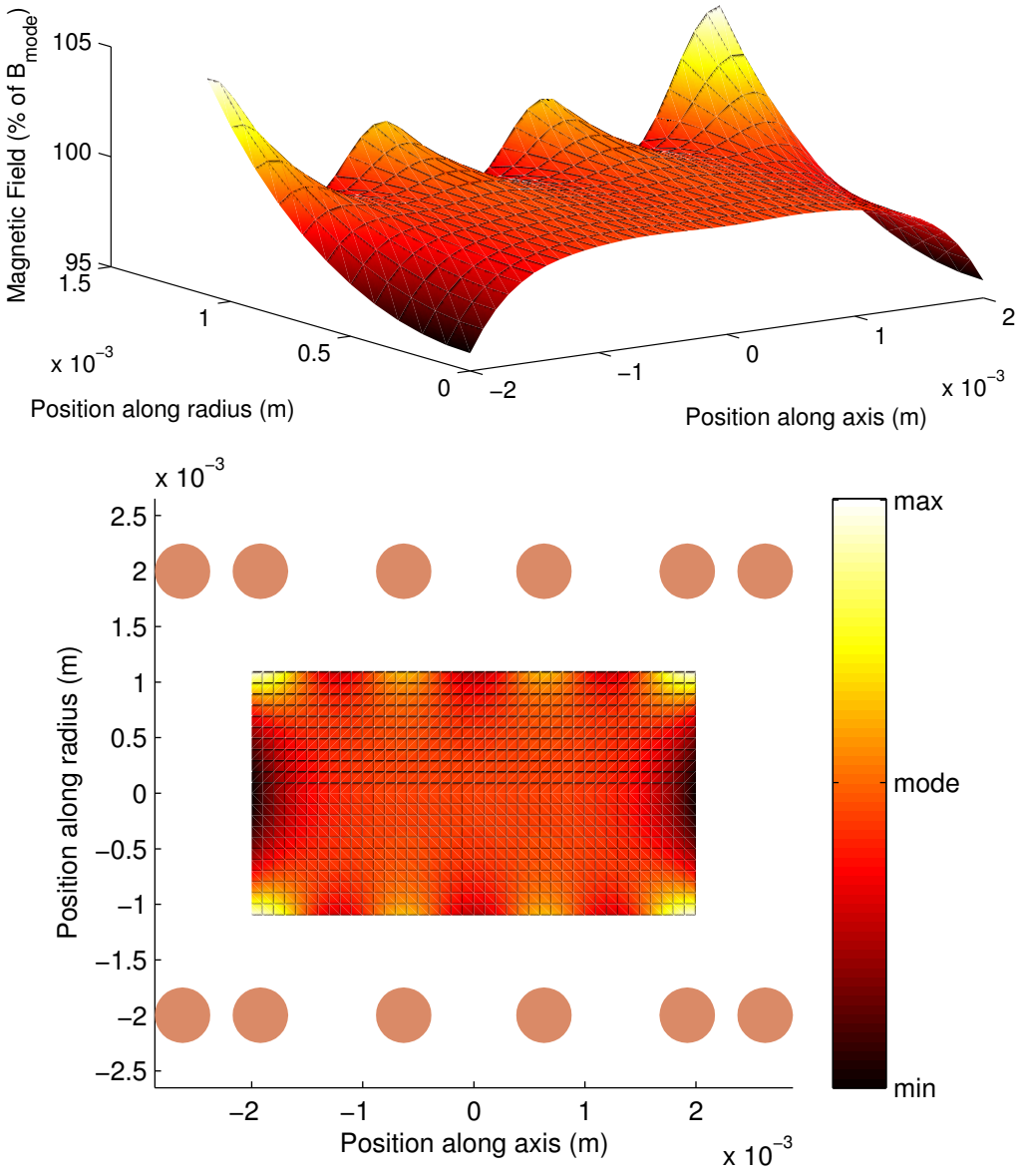

Figure C.1: Shown are the cross-sections of the wire loops (copper circles) and the spatial distribution within the sample space of the magnitude of the field produced by current passing through these loops. This solution was found starting from a uniform distribution of the loops along the axis of the coil.

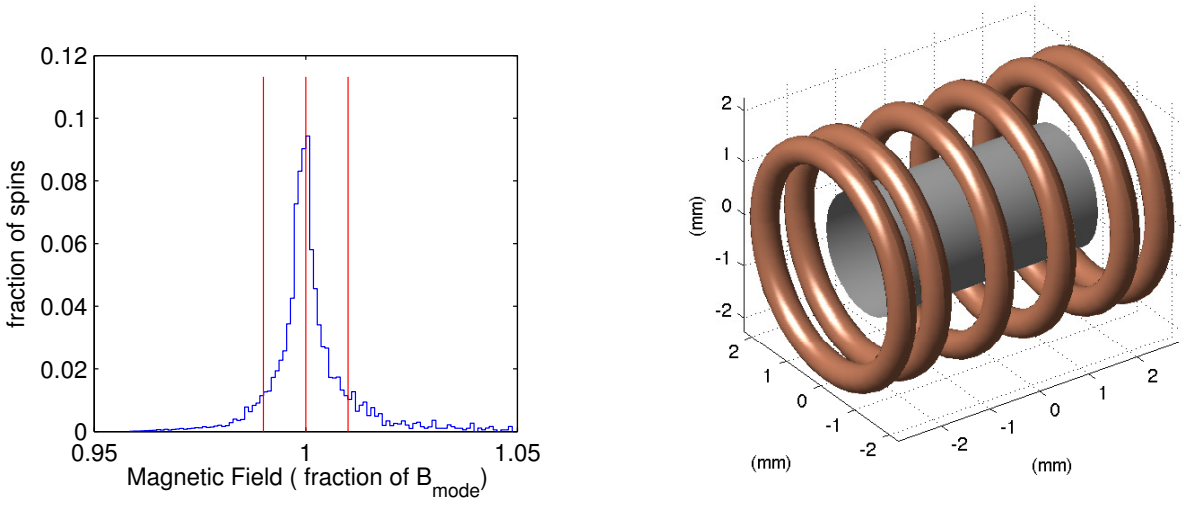

Figure C.2: A histogram of the fraction of spins whose local field has the same magnitude – 80% of the spins see a field magnitude within [0.99 B_{mode}, 1.01 $\mathrm{B}_{\mathrm{mode}}$].

At the moment, the gain expected from implementing the exact solution that was found above does not warrant the requisite precision of the coil winding – not that it is beyond today's technology. That being said, the lesson learned from this exercise is a heuristic understanding of which coil windings work better than others. And, when these lessons were applied in the winding of the coils used in current experiments, anecdotal improvements of the homogeneity were observed.

As the quality of the control improves, and every little contribution is counted, revisiting these methods would be, I suspect, highly useful.

Appendix D

Fidelity

D.1 State fidelity

For pure states, the fidelity is defined as

$$F(|\psi\rangle, |\phi\rangle) := |\langle\psi|\phi\rangle|^2 \,, \tag{D.1}$$

which can be interpreted as, for some preparation $|\phi\rangle$, the probability of measuring $|\psi\rangle$ in a measurement which distinguishes it from the orthogonal states. If one of the states is mixed, $\rho = \sum_j p_j |\phi_j\rangle$, we extend the above definition to mean the probability of measuring $|\psi\rangle$ given that the source prepares $|\phi_j\rangle$ with probabilities p_j, and the fidelity becomes

$$\begin{aligned} F(|\psi\rangle, \rho) :=& \sum_j p_j |\langle\psi|\phi_j\rangle|^2 \\ =& \sum_j \langle\psi|p_j|\phi_j\rangle\langle\phi_j||\psi\rangle \\ =& \langle\psi|\rho|\psi\rangle \,. \end{aligned} \tag{D.2}$$

This generalizes [Joz94] in the case of two mixed states to

$$F(\rho, \sigma) = \left(\mathrm{tr}\sqrt{\sqrt{\rho}\sigma\sqrt{\rho}} \right)^2 \,. \tag{D.3}$$

D.2 Process fidelity

A natural way to compare two quantum processes, $\mathcal{E}$ and $\mathcal{F}$, is the fidelity between their outputs given the same input reference state $|\psi\rangle$,

$$F_{|\psi\rangle}(\mathcal{E}, \mathcal{F}) := F(\mathcal{E}(\psi), \mathcal{F}(\psi)) \,. \tag{D.4}$$

This is known as the *gate fidelity* between $\mathcal{E}$ and $\mathcal{F}$ with respect to the state $|\psi\rangle$. Averaging over an ensemble $\rho = \sum_i p_i |\psi_i\rangle\langle\psi_i|$, gives the *ensemble average fidelity*,

$$\bar{F}_\rho(\mathcal{E}, \mathcal{F}) := \sum_i p_i F(\mathcal{E}(\psi_i), \mathcal{F}(\psi_i)) \,. \tag{D.5}$$

In the case where this ensemble is a uniform distribution of pure states, one obtains *the average fidelity*

$$\bar{F}(\mathcal{E}, \mathcal{F}) := \int d\mu(\psi) F(\mathcal{E}(\psi), \mathcal{F}(\psi)) \,, \tag{D.6}$$

where $d\mu(\psi)$ is the unitarily invariant distribution of states known as the Fubini-Study measure [EAŻ05].

In a setting where information is to be communicated across a channel, or perhaps stored faithfully in a quantum memory, one might ask how well that channel or quantum operation compare to the Identity channel. In which case, the gate fidelity simplifies to $F_{|\psi\rangle}(\mathcal{E}, \mathbb{1}) = \langle\psi|\mathcal{E}(\psi)|\psi\rangle$, and the average fidelity to

$$\bar{F}(\mathcal{E}) = \int d\mu(\psi) \langle\psi|\mathcal{E}(\psi)|\psi\rangle \,. \tag{D.7}$$

An alternative measure [Sch96] is motivated by how well a quantum operation preserves entanglement between the system of consideration, $\mathcal{H}_S$, and a reference system, $\mathcal{H}_R$. The *entanglement fidelity* of a process $\mathcal{E}$ is defined for a mixed state ρ in terms of its purification $|\psi\rangle$ over the space $\mathcal{H}_R \otimes \mathcal{H}_S$ as

$$\begin{aligned} F_e(\mathcal{E}, \rho) :=& F_{|\psi\rangle}(\mathbb{1}_R \otimes \mathcal{E}, \mathbb{1}_R \otimes \mathbb{1}_S) \\ =& \langle\psi|\mathbb{1} \otimes \mathcal{E}(|\psi\rangle\langle\psi|)|\psi\rangle \,. \end{aligned} \tag{D.8}$$

This expression can be written in terms of the reduced state and dynamics on the system alone [Sch96]. If $\mathcal{E}$ is represented by the Kraus operator sum $\mathcal{E}(\rho) = \sum_\kappa A_\kappa \rho A_\kappa^\dagger$, then (D.8) has the form

$$F_e(\mathcal{E}, \rho) = \frac{1}{d^2} \sum_\kappa |\mathrm{tr}(\rho A_\kappa)|^2 \,, \tag{D.9}$$

where d is the dimension of $\mathcal{H}_S$. The term entanglement fidelity has come to refer to the expression $F_e(\mathcal{E}, \rho)$ in the special case when ρ is taken to be the maximally mixed state, and its purification is the maximally entangled state $|\Omega\rangle = \frac{1}{d}\sum_j |j\rangle|j\rangle$,

$$F_e(\mathcal{E}) := F_e(\mathcal{E}, \tfrac{1}{d}\mathbb{1}) = \langle\Omega|\mathbb{1} \otimes \mathcal{E}(|\Omega\rangle\langle\Omega|)|\Omega\rangle \tag{D.10}$$

$$= \tfrac{1}{d^2} \sum_\kappa |\mathrm{tr}(A_\kappa)|^2 \,. \tag{D.11}$$

This is also sometimes referred to as the *channel fidelity*; and as it turns out [HHH99], the channel fidelity, $F_e(\mathcal{E})$, and the average fidelity, $\bar{F}(\mathcal{E})$, are related by the simple expression

$$\bar{F}(\mathcal{E}) = \frac{d \cdot F_e(\mathcal{E}) + 1}{d+1} \,. \tag{D.12}$$

Imagine you are given two unitary transformations – some U_g and an attempt to mimic it U_m. One way [FVH+02] to judge how well U_m mimics U_g is to compute the channel fidelity of a map that is composed of U_g followed by the reversal of U_m, using (D.11)

$$F_e(U_m^\dagger U_g) = \frac{1}{d^2} \left|\mathrm{tr}(U_m^\dagger U_g)\right|^2 = F_{HS}(U_m, U_g) \,. \tag{D.13}$$

D.3 Estimating single qubit entanglement fidelity in NMR

For a single qubit, evaluating the average fidelity reduces to [BOS+02] averaging over the pure states $\{|0\rangle, |1\rangle, |\pm\rangle = \frac{1}{\sqrt{2}}(|0\rangle \pm |1\rangle), |\pm i\rangle = \frac{1}{\sqrt{2}}(|0\rangle \pm i|1\rangle)\}$. Thus, we write

$$\bar{F}(\mathcal{E}) = \tfrac{1}{6}\left[F_{|0\rangle} + F_{|1\rangle} + F_{|+\rangle} + F_{|-\rangle} + F_{|+i\rangle} + F_{|-i\rangle}\right] \,, \tag{D.14}$$

and, using Eq. (D.12),

$$\begin{aligned} F_e(\mathcal{E}) &= \tfrac{1}{2}(3\bar{F}(\mathcal{E}) - 1) \\ &= \tfrac{1}{4}\left[F_{|0\rangle} + F_{|1\rangle} + F_{|+\rangle} + F_{|-\rangle} + F_{|+i\rangle} + F_{|-i\rangle}\right] - \tfrac{1}{2} \,. \end{aligned} \tag{D.15}$$

To experimentally estimate these terms, consider the following scheme. Say we input the state $|+\rangle\langle+| = \frac{\mathbb{1}+X}{2}$ through the *unital* channel $\mathcal{E}$, and parametrize the output state as

$$\mathcal{E}(\tfrac{\mathbb{1}+X}{2}) = \tfrac{1}{2}(\mathbb{1} + p_{xx}X + p_{xy}Y + p_{xz}Z) \,, \tag{D.16}$$

then –since $\mathcal{E}$ is unital, and above all linear– we must have

$$\mathcal{E}(\tfrac{\mathbb{1}-X}{2}) = \tfrac{1}{2}(\mathbb{1} - p_{xx}X - p_{xy}Y - p_{xz}Z) \,. \tag{D.17}$$

In which case, the fidelities $F_{|\pm\rangle}$ will evaluate to

$$\begin{aligned} F_{|\pm\rangle} &= \langle\pm|\mathcal{E}(|\pm\rangle\langle\pm|)|\pm\rangle \\ &= \tfrac{1}{4}\mathrm{tr}[(\mathbb{1} \pm X)(\mathbb{1} \pm p_{xx}X \pm p_{xy}Y \pm p_{xz}Z)] \\ &= \tfrac{1}{2}(1 + p_{xx}) \,. \end{aligned} \tag{D.18}$$

However, in NMR we have access to pseudo pure states. Consider preparing $\frac{1-\epsilon}{2}\mathbb{1} + \epsilon|\pm\rangle\langle\pm| = \frac{1}{2}\mathbb{1} \pm \frac{\epsilon}{2}X$, and applying $\mathcal{E}$ to get

$$\mathcal{E}(\tfrac{1-\epsilon}{2}\mathbb{1} + \epsilon|\pm\rangle\langle\pm|) = \tfrac{1-\epsilon}{2}\mathbb{1} + \tfrac{\epsilon}{2}(\mathbb{1} \pm p_{xx}X \pm p_{xy}Y \pm p_{xz}Z)\,. \tag{D.19}$$

If we measure the polarization in X before and after the channel $\mathcal{E}$, the fraction of polarization surviving is given by

$$\begin{aligned} f_{|\pm\rangle} &= \frac{\mathrm{tr}[\frac{1}{2}X(\mathbb{1} \pm p_{xx}\frac{\epsilon}{2}X \pm p_{xy}\frac{\epsilon}{2}Y \pm p_{xz}\frac{\epsilon}{2}Z)]}{\mathrm{tr}[\frac{1}{2}X(\frac{1}{2}\mathbb{1} \pm \frac{\epsilon}{2}X)]} \\ &= p_{xx}\,, \end{aligned} \tag{D.20}$$

which we rename as f_x. Substituting in Eqs. (D.18) and (D.15)

$$F_{|\pm\rangle} = \frac{1}{2}(1 + f_x)\,, \tag{D.21}$$

and

$$F_e(\mathcal{E}) = \frac{1}{4}\left[1 + f_x + f_y + f_z\right]\,. \tag{D.22}$$

D.4 The entanglement fidelity of the depolarizing channel

The depolarizing channel on a d-dimensional system is defined in terms of a single parameter, p, as

$$\Lambda(\rho) = p\rho + (1-p)\frac{\mathbb{1}}{d}\,, \tag{D.23}$$

which, for a single qubit, can be seen as a shrinking, or a scaling, of the Bloch sphere. First, we find an expression for the composition of depolarizing channels by induction. Noting that

$$\begin{aligned} \Lambda^2(\rho) :&= \Lambda(\Lambda(\rho)) \\ &= p\Lambda(\rho) + (1-p)\frac{\mathbb{1}}{d} \\ &= p^2\rho + p(1-p)\frac{\mathbb{1}}{d} + (1-p)\frac{\mathbb{1}}{d} \\ &= p^2\rho + (1-p^2)\frac{\mathbb{1}}{d}\,, \end{aligned} \tag{D.24}$$

we write

$$\Lambda^n(\rho) = p^n\rho + (1-p^n)\frac{\mathbb{1}}{d}\,, \tag{D.25}$$

and evaluate

$$\begin{aligned}\Lambda^{n+1}(\rho) :&= \Lambda(\Lambda^n(\rho)) \\ &= p\Lambda^n(\rho) + (1-p)\frac{\mathbb{1}}{d} \\ &= p^{n+1}\rho + p(1-p^n)\frac{\mathbb{1}}{d} + (1-p)\frac{\mathbb{1}}{d} \\ &= p^{n+1}\rho + (1-p^{n+1})\frac{\mathbb{1}}{d}\,. \quad \square\end{aligned} \tag{D.26}$$

That is to say, the decomposition of n identical deoplarizing channels is a depolarizing channel, whose parameter is the n-th power of the original channel.

The single qubit depolarizing channel can be written as

$$\Lambda_1(\rho) = p\ \mathbb{1}\rho\mathbb{1} + \frac{(1-p)}{4}(X\rho X + Y\rho Y + Z\rho Z + \mathbb{1}\rho\mathbb{1})\,, \tag{D.27}$$

which is to say that Λ_1^n can be described by the Kraus operators:

$$\{A_\kappa\}_\kappa = \left\{\frac{\sqrt{1+3p^n}}{2}\mathbb{1}, \frac{\sqrt{1-p^n}}{2}X, \frac{\sqrt{1-p^n}}{2}Y, \frac{\sqrt{1-p^n}}{2}Z\right\}\,, \tag{D.28}$$

and using Eq. (D.11), the entanglement fidelity is

$$\begin{aligned}F_e(\Lambda_1^n) &= \tfrac{1}{4}\sum_\kappa |\mathrm{tr}(A_\kappa)|^2 \\ &= \frac{1+3p^n}{4}\,.\end{aligned} \tag{D.29}$$

Appendix E

Other significant contributions

E.1 Heat-bath Algorithmic cooling

State-preparation of quantum bits in or near a known state poses a challenge to the implementation of scalable quantum computation; a challenge that is especially highlighted in the case of ensemble implementations. Such preparation is required in initializing a quantum computer for computation, and in dynamically and continually supplying fresh qubits in a low-entropy state as ancillas for error correction.

Remarkably, there exist implementation independent techniques that employ quantum logic operations to obtain a subset of highly-polarized qubits from an initial set of weakly-biased ones. The latest of these techniques, the partner pairing algorithm (PPA) introduced by Schulman *et al.* makes use of a reset bit that can be brought in thermal contact with a heat bath at appropriate times to pump entropy out of the computational bits.

My contribution was to figure out the explicit quantum network needed to implement the PPA on a three qubit system. I was also involved with pulse sequence design.

nature Vol 438|24 November 2005|doi:10.1038/nature04272

LETTERS

Experimental implementation of heat-bath algorithmic cooling using solid-state nuclear magnetic resonance

J. Baugh[1], O. Moussa[1], C. A. Ryan[1], A. Nayak[1,2,3] & R. Laflamme[1,3]

The counter-intuitive properties of quantum mechanics have the potential to revolutionize information processing by enabling the development of efficient algorithms with no known classical counterparts[1,2]. Harnessing this power requires the development of a set of building blocks[3], one of which is a method to initialize the set of quantum bits (qubits) to a known state. Additionally, fresh ancillary qubits must be available during the course of computation to achieve fault tolerance[4–7]. In any physical system used to implement quantum computation, one must therefore be able to selectively and dynamically remove entropy from the part of the system that is to be mapped to qubits. One such method is an 'open-system' cooling protocol in which a subset of qubits can be brought into contact with an external system of large heat capacity. Theoretical efforts[8–10] have led to an implementation-independent cooling procedure, namely heat-bath algorithmic cooling. These efforts have culminated with the proposal of an optimal algorithm, the partner-pairing algorithm, which was used to compute the physical limits of heat-bath algorithmic cooling[11]. Here we report the experimental realization of multi-step cooling of a quantum system via heat-bath algorithmic cooling. The experiment was carried out using nuclear magnetic resonance of a solid-state ensemble three-qubit system. We demonstrate the repeated repolarization of a particular qubit to an effective spin-bath temperature, and alternating logical operations within the three-qubit subspace to ultimately cool a second qubit below this temperature. Demonstration of the control necessary for these operations represents an important step forward in the manipulation of solid-state nuclear magnetic resonance qubits.

Nuclear magnetic resonance (NMR)-based ensemble quantum information processing (QIP) devices have provided excellent test beds for controlling non-trivial numbers of qubits[12–15]. A solid-state NMR QIP architecture builds on this success by incorporating the essential features of the liquid-state devices while offering the potential to reach unit polarization and thus control more qubits[15,16]. In this architecture, the abundant nuclear spins with polarization P form a large-heat-capacity spin-bath that can be either coupled to, or decoupled from, a dilute, embedded ensemble of spin-labelled isotopomers that comprise the qubit register. Bulk spin-cooling procedures such as dynamic nuclear polarization are well known and capable of reaching polarizations near unity[15,17]. This architecture is one realization within a large class of possible solid-state QIP systems in which coherently controlled qubits can be brought into contact with an external system that behaves as a heat bath. The principles and methods applied in solid-state NMR QIP will therefore apply to many other systems. An additional motivation is development of control techniques that future quantum devices will harness. For this experiment, we develop a novel technique to implement the controlled qubit–bath interaction, and also report the first application of strongly modulating pulses[18] to solid-state NMR for high-fidelity, coherent qubit control.

The three-qubit quantum information processor used here is formed by the three spin-1/2 ^{13}C nuclei of isotopically labelled malonic acid molecules, occupying a dilute fraction of lattice sites in an otherwise unlabelled single crystal of malonic acid (unlabelled, with the exception of naturally occurring ^{13}C isotopes at the rate of 1.1%). The concentration of labelled molecules was 3.2%. Malonic acid also contains abundant spin-1/2 ^{1}H nuclei, which comprise the heat-bath. Figure 1 shows the ^{1}H-decoupled, ^{13}C-NMR spectrum for the crystal (and crystal orientation) used in this work. The spectrum shows the NMR absorption peaks of both the qubit spins (quartets) and natural abundance ^{13}C spins (singlets), the latter being inconsequential for QIP purposes. The table in Fig. 1 lists the parameters of the ensemble qubit hamiltonian obtained from fitting the spectrum, and also includes couplings involving the methylene protons calculated for this crystal orientation from the known crystal structure[19]. Experiments were performed at room temperature at a static magnetic field strength of 7.1 T, where the thermal ^{1}H polarization is $P_{\mathrm{H}} \approx 2.4 \times 10^{-5}$.

In this orientation, the methylene carbon C_m has a dipolar coupling of 19 kHz to H_{m1} of the methylene ^{1}H pair, whereas no other ^{13}C-^{1}H dipolar coupling in the system is larger than 2 kHz (see Fig. 1 for atom nomenclature). Therefore, a spin-exchange hamiltonian of the form

$$H_{\mathrm{ex}} = \sum_{j\in C,k\in H} \frac{D_{jk}}{3} \frac{\sigma_z^j\sigma_z^k + \sigma_y^j\sigma_y^k + \sigma_x^j\sigma_x^k}{2} \qquad (1)$$

that couples the two nuclear species will generate dynamics dominated by the large C_m–H_{m1} coupling at short times (the D_{jk} are ^{13}C–^{1}H dipolar couplings, indices j,k run over ^{13}C,^{1}H nuclei, respectively, and σ_β^α is the β-axis Pauli operator for spin α). Starting from the natural coupling hamiltonian, $H_{\mathrm{nat}} = \sum_{j\in C,k\in H} D_{jk}\sigma_z^j\sigma_z^k/2$, we applied a multiple-pulse 'time-suspension' sequence[20] synchronously to both ^{13}C and ^{1}H spins to create the effective spin-exchange hamiltonian (in the toggling frame), to lowest order in the Magnus expansion of the average hamiltonian[21]. Application of the sequence for the C_m–H_{m1} exchange period $\tau = 3/(4 \times 19\,\mathrm{kHz}) \approx 40\,\mu\mathrm{s}$ results in an approximate swap gate (state exchange) between the C_m and H_{m1} spins. With an initial bulk ^{1}H polarization P_{H}, this procedure yields a selective dynamic transfer of polarization $P' = \eta P_{\mathrm{H}}$ to C_m, where $0 \le |\eta| \le 1$ and ideally $|\eta| = 1$. We define the effective spin-bath temperature to be that which corresponds to the experimentally

[1]Institute for Quantum Computing, [2]Department of Combinatorics and Optimization, University of Waterloo, Waterloo, Ontario N2L 3G1, Canada. [3]Perimeter Institute for Theoretical Physics, Waterloo, Ontario N2L 2Y5, Canada.

	C_1	C_2	C_m	H_{m1}
C_1	5.893			
C_2	0.227	1.057		
C_m	0.935	1.070	–3.445	
H_{m1}	–1.5	1.4	–18.7	
H_{m2}	2.0	1.0	–0.9	–22.0

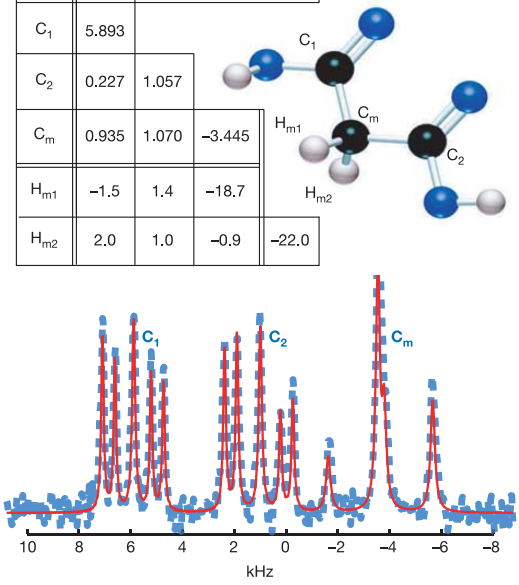

Figure 1 | Characteristics of the dilute 3-^{13}C malonic acid spin system. Bottom, ^{1}H-decoupled, ^{13}C spectrum near the [010] orientation with respect to the static magnetic field. The blue-dashed line is the experimental NMR absorption spectrum, and the solid red line is a fit. Multiplet assignments are indicated by the labels C_1, C_2 and C_m. The central peaks in each multiplet correspond to natural abundance ^{13}C in the sample, which are inconsequential for QIP purposes. The peak height differences in the 3-^{13}C molecule peaks indicate the strong coupling regime, that is, the ^{13}C–^{13}C intramolecular dipolar couplings are significant compared to the relative chemical shifts. Top, table showing the ^{13}C rotating-frame hamiltonian parameters (chemical shifts along diagonal; dipolar coupling strengths off-diagonal; all values in kHz) obtained from the spectral fit. It also includes calculated dipolar couplings involving the methylene protons based on the atomic coordinates[19] and the crystal orientation obtained from the spectral fit.

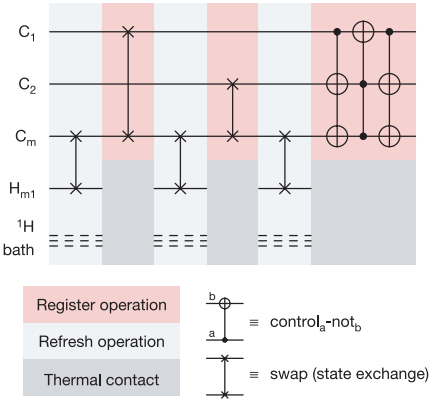

Figure 2 | Schematic quantum circuit diagram of the implemented protocol. Time flows from left to right. The three-bit compression (3BC) gate is shown here decomposed as control-not gates and a control-control-not (Toffoli) gate. The gate sequence corresponds to the first six steps of the partner-pairing algorithm[11] on three qubits. The input state is a collective polarization P_H of the bulk ^{1}H. The refresh operation is approximately 40 μs in duration, whereas the register operations are between 0.7 and 1.3 ms in duration. Thermal contact takes place during ^{1}H spin-locking pulses that begin just before the register operations, and extend an additional 12 ms after each operation. H_{m1} can be thought of as an additional 'special purpose' qubit in this experiment; despite non-selective ^{1}H control (due to bulk hydrogenation), the refresh and thermal contact operations could be performed using collective ^{1}H control. Thus, H_{m1} serves as a fast-relaxing 'qubit' and the bulk ^{1}H-bath as a thermal bath of large heat capacity.

obtained P' under this procedure, and refer to this transfer as a refresh operation. We obtained $P' \approx 0.83P_H$ experimentally, and found that repeated refresh operations showed no loss in efficiency given at least a 6 ms delay for ^{1}H–^{1}H equilibration. However, we observed a decay of P_H as a function of the number of repetitions, due to accumulated control errors, which lead to an identical loss in the refresh polarization.

The experiment consists of the first six operations of the partner-pairing algorithm (PPA) on three qubits: three refresh operations, and three permutation gates that operate on the qubit register. This is described in the quantum circuit diagram of Fig. 2. During the register operations, the ^{1}H polarization is first rotated into the transverse plane, and then 'spin-locked' by a strong, phase-matched radio frequency (r.f.) field that both preserves the bulk ^{1}H polarization and decouples the ^{1}H–^{13}C dipolar interactions. As ^{1}H–^{1}H dipolar interactions are merely scaled by a factor $-1/2$ under spin-locking, H_{m1} is allowed to equilibrate with the bulk ^{1}H nuclei via spin diffusion. This occurs on a timescale longer than the transverse dephasing time ($T_2(H_m) \approx 100\,\mu s$), but much shorter than the spin–lattice relaxation time ($T_1^H \approx 50\,s$) of H_{m1}. Hence, H_{m1} plays the role of the fast-relaxing qubit described in the protocol of ref. 11. The first two register operations are swap gates; the third is a three-bit compression (3BC) gate[8–10] that boosts the polarization of the first qubit, C_1, at the expense of the polarizations of the other two qubits.

Ideally, the protocol builds a uniform polarization on all three qubits corresponding to the bath polarization (first five steps), then selectively transfers as much entropy as possible from the first qubit to the other two (last step). The last step (3BC) leads to a polarization boost by a factor of 3/2 on the first qubit. Subsequently, the heated qubits can be re-cooled to the spin-bath temperature, and the compression step repeated, iteratively, until the asymptotic value of the first-bit polarization is reached. This limiting polarization depends only on the number of qubits and the bath polarization[11], and is ideally $P(C_1) = 2P'$ for three qubits (for n qubits it is $2^{n-2}P'$ in the regime $P' \ll 2^{-n}$, and 1.0 in the regime $P' \gg 2^{-n}$ (refs 11, 22)). The first six steps carried out here should yield a polarization of $1.5P'$ on C_1, assuming ideal operations.

The control operations performed here are quantum control operations: state-independent unitary rotations in the Hilbert space. However, it should be noted that the heat-bath algorithmic cooling gates are all permutations that map computational basis states to other computational basis states. Therefore, gate fidelities were measured with respect to correlation with these known states, rather than the manifold of generic quantum states. We took advantage of this property to further optimize the control parameters of the ^{13}C gates (register operations) for the state-specific transformations of the protocol. These operations were carried out using numerically optimized control sequences referred to as strongly modulating pulses[18]. Such pulses drive the system strongly at all times, such that the average r.f. amplitude is comparable to, or greater than, the magnitude of the internal hamiltonian. This allows inhomogeneities in the ensemble qubit hamiltonian to be efficiently refocused, so that ensemble coherence is better maintained throughout the gate operations.

In this set of experiments, the ^{13}C qubit spins are initialized to infinite temperature (a preceding broadband ^{13}C $\pi/2$ excitation pulse is followed by a dephasing period in which ^{1}H dipolar fields effectively dephase the ^{13}C polarization). Following the fifth step,

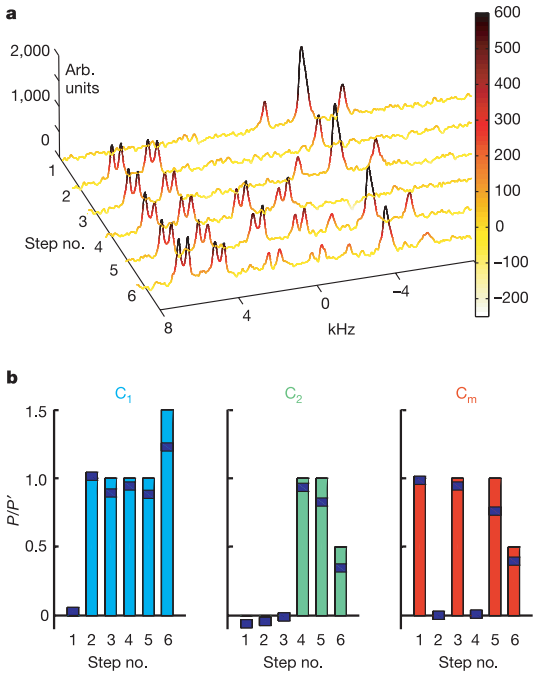

Figure 3 | Experimental results in terms of ^{13}C spectra and their integrated intensities. a, Readout spectra obtained following each of the six steps in the protocol. A colour scale indicates peak intensities, which are in arbitrary units. The integrated peak intensities for each multiplet correspond to the ensemble spin polarizations. The natural abundance C_m signal that appears at each refresh step (adding to the intensity of the central peaks) should be ignored; we are only interested in the part of the signal arising from the 3-^{13}C qubit molecules, which can be seen clearly in the C_1 and C_2 spectral regions. **b**, Bars indicate ideal qubit polarizations at each step; experimental values obtained from integration of the above spectra are shown as shaded bands, whose thickness indicates experimental uncertainty.

polarizations (in units of P') of 0.88, 0.83 and 0.76 ($\pm$0.03) are built up on C_1, C_2 and C_m, respectively. The final 3BC operation yields $P(C_1)/P' = 1.22 \pm 0.03$, an increase of 48% compared to the average polarization (0.82) following step five. Despite control imperfections that effectively heat the qubits at each step, we are able to cool the C_1 qubit ensemble well below the effective ^{1}H spin-bath temperature.

The results are summarized in Fig. 3; in Fig. 3a are shown the spectral intensities corresponding to ^{13}C spin polarizations following each of the six steps, and in Fig. 3b the integrated intensities are graphed in comparison with the ideal values. We note that the overall fidelity of the experiment, $F = 1.22/1.50 = 0.81$, implies an error per step of 3.7%. This error rate is only about a factor of two larger than the average error per two-qubit gate obtained in a benchmark liquid-state NMR QIP experiment[12]. Furthermore, the state-correlation fidelity of the 3BC gate over the polarizations on all three qubits is 0.96 ± 0.03. From Fig. 3b, it can be seen that the fidelity of the refresh operation drops off roughly quadratically in the number of steps; this is consistent with the loss of bulk ^{1}H polarization due to pulse imperfections both in the multiple-pulse refresh operations and in the spin-locking sequence. As the broadband pulses have been optimized for flip-angle in these sequences, we suspect that the remaining errors are mainly due to switching transients that occur in the tuned r.f. circuitry of the NMR probe head, and to a lesser extent off-resonance and finite pulse-width effects that modify the average hamiltonian[20]. Similar effects lead to imperfect fidelity of the ^{13}C control. With suitable improvements to the resonant circuit response and by incorporating numerical optimization of the multiple-pulse refresh operations, we expect that several iterations of the protocol could be carried out and that the limiting polarization of $2P'$ could be approached in this system. The same methodologies should also be applicable in larger qubit systems with similar architecture. For a six-qubit system using the PPA, a bath polarization $P' > 0.2$ would be sufficient, in principle, to reach a pure state on one qubit[22]. Such bulk nuclear polarizations are well within reach via well-known dynamic nuclear polarization techniques[17]; for example, unpaired electron spins at defects (g-factor = 2) in a field of 3.4 T and at temperature 4.2 K are polarized to 0.5.

This work demonstrates that solid-state NMR QIP devices could be used to implement active error correction. Given a bath polarization near unity, the refresh operation implemented here would constitute the dynamic resetting of a chosen qubit. This would allow a new NMR-based test bed for the ideas of quantum error correction and for controlled open-system quantum dynamics in the regime of high state purity and up to approximately 20 qubits.

METHODS

NMR experiments were carried out at room temperature on a Bruker Avance solid-state spectrometer operating at a field of 7.1 T, and a purpose-built dual channel r.f. probe. The sample coil had an inner diameter of 3 mm, and the employed $\pi/2$ broadband pulse lengths were 1.25 μs and 0.75 μs for ^{13}C and ^{1}H, respectively. The sample was a $4 \times 1.5 \times 1.5$ mm^3 single crystal of malonic acid grown from aqueous solution with a 3.2% molecular fraction of 3-^{13}C labelled molecules. Spectra were obtained by signal averaging for 80 scans. The proton spin–lattice relaxation time was $T_1^H = 50$ s, so the delay between scans was set to $6T_1^H = 300$ s. The average ^{13}C free-induction dephasing rate (with ^{1}H decoupling) was $1/T_2^* = (2\,\mathrm{ms})^{-1}$ in our sample. This rate is dominated by the ensemble dispersion of chemical shifts, much of which is effectively removed by the control operations. Design of the strongly modulating ^{13}C pulses followed very closely the methodology described in ref. 18, and penalty functions were adjusted to favour average r.f. amplitudes comparable to or greater than the magnitude of the ^{13}C rotating-frame hamiltonian. These pulses were optimized and simulated over a five-point distribution of r.f. amplitude corresponding to the measured distribution over the spin ensemble ($\sigma = 6.2\%$ in r.f. amplitude). The 'time-suspension' sequence applied synchronously to ^{13}C and ^{1}H was a 12-pulse subsequence of the Cory 48-pulse sequence[20]. The delays between pulses were adjusted so that the total length of the sequence was 40 μs. ^{1}H spin-locking/decoupling was carried out at an r.f. amplitude of 250 kHz. The spectra in Fig. 3 were obtained by applying a $\pi/2$ broadband pulse to read out the spin polarizations. The absolute value of the refresh polarization P' was determined by comparing the initial refresh polarization on C_m and the thermal equilibrium ^{13}C polarization P_C measured in a separate experiment. These yield the ratio of P' to P_C, and P' to P_H using the fact that $P_H = 3.98P_C$.

Received 14 July; accepted 22 September 2005.

1. Nielsen, M. A. & Chuang, I. L. *Quantum Computation and Quantum Information* (Cambridge Univ. Press, Cambridge, 2000).
2. Everitt, H., Havel, T. F. & Cory, D. G. (eds) Experimental aspects of quantum computing. *Quant. Inform. Process.* **3**(1–5; special issue), 1–308 (2004).
3. DiVincenzo, D. P. The physical implementation of quantum computation. *Fortschr. Phys.* **48**, 771–793 (2000).
4. Knill, E., Laflamme, R. & Zurek, W. H. Resilient quantum computation. *Science* **279**, 342–345 (1998).
5. Kitaev, A. Y. in *Quantum Communication and Computing and Measurement* (eds Holevo, A. S., Hirota, O. & Caves, C. M.) 181–188 (Plenum, New York, 1997).
6. Aharonov, D. & Ben-Or, M. in *Proc. 29th Annual ACM Symp. on Theory of Computing* (eds Leighton, F. T. & Shor, P.) 176–188 (ACM Press, New York, 1997).
7. Preskill, J. Reliable quantum computers. *Proc. R. Soc. Lond. A* **454**, 385–410 (1998).
8. Schulman, L. J. & Vazirani, U. V. in *Proc. 31st Annual ACM Symp. on Theory of Computing* (eds Vitter, J. S., Larmore, L. & Leighton, T.) 322–329 (ACM Press, New York, 1999).
9. Boykin, P. O., Mor, T., Roychowdhury, V., Vatan, F. & Vrijen, R. Algorithmic cooling and scalable NMR quantum computers. *Proc. Natl Acad. Sci. USA* **99**, 3388–3393 (2002).
10. Fernandez, J. M., Lloyd, S., Mor, T. & Roychowdhury, V. Algorithmic cooling of spins: a practicable method for increasing polarization. *Int. J. Quant. Inform.* **2**, 461–467 (2004).

11. Schulman, L. J., Mor, T. & Weinstein, Y. Physical limits of heat-bath algorithmic cooling. *Phys. Rev. Lett.* **94,** 120501 (2005).
12. Knill, E., Laflamme, R., Martinez, R. & Tseng, C.-H. An algorithmic benchmark for quantum information processing. *Nature* **404,** 368–370 (2000).
13. Gershenfeld, N. & Chuang, I. L. Bulk spin-resonance quantum computation. *Science* **275,** 350–356 (1997).
14. Cory, D. G., Price, M. D. & Havel, T. F. Nuclear magnetic resonance spectroscopy: An experimentally accessible paradigm for quantum computing. *Physica D* **120,** 82–101 (1998).
15. Cory, D. G. *et al.* NMR based quantum information processing: achievements and prospects. *Fortschr. Phys.* **48,** 875–907 (2000).
16. Leskowitz, G. M., Ghaderi, N., Olsen, R. A. & Mueller, L. J. Three-qubit nuclear magnetic resonance quantum information processing with a single-crystal solid. *J. Chem. Phys.* **119,** 1643–1649 (2003).
17. Abragam, A. & Goldman, M. *Nuclear Magnetism: Order and Disorder* 339–393 (Clarendon, Oxford, 1982).
18. Fortunato, E. M. *et al.* Design of strongly modulating pulses to implement precise effective Hamiltonians for quantum information processing. *J. Chem. Phys.* **116,** 7599–7606 (2002).
19. Jagannathan, N. R., Rajan, S. S. & Subramanian, E. Refinement of the crystal structure of malonic acid, $C_3H_4O_4$. *J. Chem. Crystallogr.* **24,** 75–78 (1994).
20. Cory, D. G., Miller, J. B. & Garroway, A. N. Time-suspension multiple-pulse sequences: applications to solid-state imaging. *J. Magn. Res.* **90,** 205–213 (1990).
21. Haeberlen, U. *High Resolution NMR in Solids: Selective Averaging* Suppl. 1, *Advances in Magnetic Resonance* 64–69 (Academic, New York, 1976).
22. Moussa, O. *On Heat-bath Algorithmic Cooling and its Implementation in Solid-state NMR*. Page 20, M.Sc. thesis, Univ. Waterloo (2005); available at ⟨http://www.iqc.ca/~omoussa/work/thesis/⟩.

Acknowledgements We thank D. G. Cory, T. F. Havel and C. Ramanathan for discussions and use of NMR simulation code; W. P. Power, M. J. Ditty and N. J. Taylor for facility use and experimental assistance; CIAR, ARDA and NSERC for support. O.M. acknowledges the Ontario Ministry of Training, Colleges and Universities for support.

Author Information Reprints and permissions information is available at npg.nature.com/reprintsandpermissions. The authors declare no competing financial interests. Correspondence and requests for materials should be addressed to J.B. (baugh@iqc.ca).

Spin Based Heat Engine: Demonstration of Multiple Rounds of Algorithmic Cooling

C. A. Ryan,[1] O. Moussa,[1] J. Baugh,[1] and R. Laflamme[1,2]

[1]*Institute for Quantum Computing and Department of Physics, University of Waterloo, Waterloo, Ontario, N2L 3G1, Canada*
[2]*Perimeter Institute for Theoretical Physics, Waterloo, Ontario, N2J 2W9, Canada*

(Received 19 June 2007; published 9 April 2008)

We experimentally demonstrate multiple rounds of heat-bath algorithmic cooling in a 3 qubit solid-state nuclear magnetic resonance quantum information processor. By pumping entropy into a heat bath, we are able to surpass the closed system limit of the Shannon bound and purify a single qubit to 1.69 times the heat-bath polarization. The algorithm combines both high fidelity coherent control and a deliberate interaction with the environment. Given this level of quantum control in systems with larger reset polarizations, nearly pure qubits should be achievable.

DOI: 10.1103/PhysRevLett.100.140501 PACS numbers: 03.67.Lx, 05.70.−a, 76.60.−k

Using quantum mechanics to process information promises the possibility to dramatically speed up certain computations and simulations [1]. Many experimental paths are being pursued in the goal of coherently manipulating quantum systems [2]. The standard circuit based model has certain experimental criteria [3], one of which is the ability to initialize pure fiducial quantum states. This is needed not only to create the initial state for many quantum algorithms, but it is also necessary to have pure qubits on demand throughout the computation in order to compute fault-tolerantly in the presence of errors [4]. However, many physical implementations are able to initialize only mixed states with a certain bias towards the desired state. In these cases it will almost certainly be necessary to run some protocol to purify the qubits. Aside from quantum information purposes, the ability to increase the bias of nuclear spins is fundamentally important in nuclear magnetic resonance (NMR) where small signal to noise ratios are usually overcome with signal averaging. A boost in the initial bias by a factor b would reduce the experiment time by b^2.

A potential solution is algorithmic cooling which is essentially classical and based on early work from von Neumann [5]. If the bits start with some bias ϵ, so the probability of being in the state 0 or spin up is $P_\uparrow = \frac{1+\epsilon}{2}$ and $P_\downarrow = \frac{1-\epsilon}{2}$, then the application of a logic gate can compress the uncertainty into some fraction of the qubits and increase the bias on the rest, cooling them below their thermal polarization. Using these ideas it was shown that by starting with a sufficient number of qubits it is possible to initialize a small number of qubits to a fiducial state with near certainty [6,7]. However, for the starting biases typical of room temperature NMR, that sufficient number is an impractically large number; e.g., to purify only one qubit requires $\approx 10^{12}$ spins. In a closed system, the compression step is limited by the Shannon bound (the total entropy of the system is conserved) and usually the Sorensen bound [8] (unitary transformations) as well. As a relevant example, with three qubits, each starting with the same polarization ϵ, it is not possible to amplify the bias of one qubit to more than 1.5ϵ.

If we consider an open system, and allow the ability to pump entropy through a qubit reset step, then we can surpass the Shannon bound. Every compression step cools some subset of qubits and heats up the remainder of the qubits above the heat-bath temperature. If these heated qubits are cooled back to the heat-bath temperature, the total entropy of the qubit system has decreased. The cooling algorithm then consists of alternating rounds of cooling and compression [9–12]. Recently Schulman *et al.* [13] have shown an optimal algorithm, the partner pairing algorithm (PPA), for the scenario of having one special purpose reset qubit. They also showed a crucially important threshold: given n qubits and a heat-bath bias of $\epsilon \gg 2^{-n}$ then it is possible to almost perfectly purify the system with resources growing polynomially in n; whereas, if $\epsilon \ll 2^{-n}$, the maximum bias achievable on one qubit is $\epsilon 2^{n-2}$ [14]. A similar system with differential relaxation rates has been considered for error correction purposes and could also be used for purification [15]. Several parts of the cooling algorithms, including both the compression step [16] and the reset [17], have been experimentally demonstrated using NMR quantum information processors (QIP). These were combined by Baugh *et al.* [18] to show one round of cooling three qubits and the compression step. However, sufficient control was lacking to demonstrate multiple rounds of cooling and compression. Here, we present experimental results showing multiple rounds of resetting and compression steps allowing us to go beyond the Shannon bound for the first time.

NMR offers one of the most advanced implementations of a QIP with high fidelity control and several qubits [19]. The qubits are nuclear spins in a bulk ensemble sample where many, ideally identical, copies of the processor are manipulated in parallel. Readout consists of measuring the expectation value of operators averaged over the sample. A large static magnetic field provides the quantization axis and for spin 1/2 nuclei, two Zeeman energy levels. The majority of previous work in NMR QIP has focused on liquid state systems that have a simple Hamiltonian and good coherence properties. Solid-state systems are more difficult to control in practice but offer intrinsically longer

coherence times, the ability to pump entropy out of the system of interest into a spin bath, and the potential for much higher initial polarizations. The specific system used here is a three qubit processor molecule, malonic acid [20]. The sample is a macroscopic single crystal, where a small fraction ($\approx 3\%$) of the molecules are triply labeled with ^{13}C to form the processor molecules. The 100% abundant protons in the crystal form the heat bath. A proton-decoupled ^{13}C spectrum is shown in Fig. 1. An accurate natural Hamiltonian is necessary for high fidelity control and is obtained from precise spectral fitting. The spectrum is simulated from the evolution of the natural Hamiltonian, and the Hamiltonian parameters (chemical shifts, dipolar couplings, and the much weaker J couplings, which are usually ignored in the solid state) are then varied to optimize the fit through a least squares minimization. The control pulses are designed to be robust to the large uncertainty (≈ 150 Hz) in chemical shift and are fortuitously robust to the much smaller uncertainties (<10 Hz) in the coupling constants.

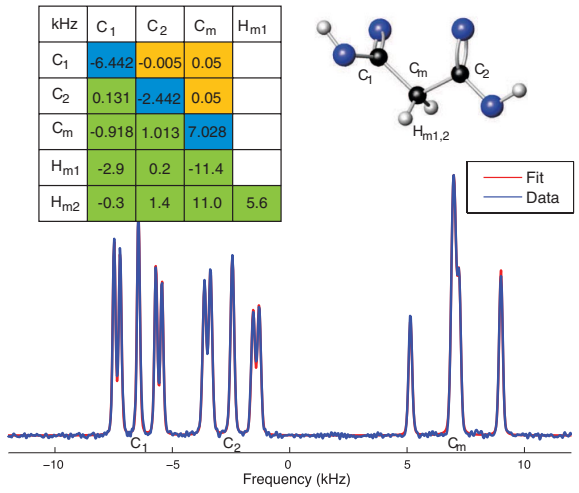

FIG. 1 (color online). The proton-decoupled ^{13}C spectrum of malonic acid in the orientation used in the experiments. The experiments were performed in a static field of 7.1 T using a purpose-built probe. Also shown is the molecule and a table of the Hamiltonian parameters (kHz). Diagonal elements give chemical shifts with respect to the transmitter frequency (Hamiltonian $\sum_i \pi\omega_i\sigma_z^i$). Below the diagonal are dipolar couplings ($\sum_{i<j} \frac{\pi}{2} D_{ij}(2\sigma_z^i\sigma_z^j - \sigma_x^i\sigma_x^j - \sigma_y^i\sigma_y^j)$) and above are J coupling constants ($\sum_{i<j} \frac{\pi}{2} J_{ij}(\sigma_z^i\sigma_z^j + \sigma_x^i\sigma_x^j + \sigma_y^i\sigma_y^j)$). ^{13}C–^{13}C Hamiltonian values are obtained from the spectral fit. The peak heights give information about the relative strengths of the dipolar and the indirect J couplings. The three central peaks of each multiplet are from the natural abundance of ^{13}C present in the molecule at $\approx 1\%$. Combining the fitting information with crystal structure data from neutron scattering experiments [31] gives the orientation of the molecule with respect to the static magnetic field and from that the proton-carbon dipolar couplings.

The experiment consisted of four rounds of cooling and compression. The quantum circuit implemented is shown in Fig. 2. The carbon register is initialized to infinite temperature by dephasing the thermal polarization. The bulk ^1H polarization was then rotated into the plane and held with a rf spin-locking pulse. Selective transfer of the polarization from $H_{m1,2}$ to C_m served as the refresh step (see below). During the spin-locking periods, which also serve to decouple the protons during the logic gates, the proton dipolar coupling network allows for spin diffusion. Thus, $H_{m1,2}$ are cooled by the rest of the proton bath and return to the heat-bath temperature prior to the next refresh step. The polarization on C_m is swapped to C_1 or C_2 with a carbon control sequence. Once the heat-bath polarization is built up on all three spins, the polarization is then compressed onto C_2. C_2 has the smallest proton-carbon coupling and so is least affected by errors due to incomplete decoupling and imperfect refresh steps. Ideally, this first compression step should boost the polarization of C_2 to $1.5\times$ the heat-bath polarization (end of step 1 in Fig. 2). Subsequent steps involve returning C_m and C_1 to the heat-bath temperature and repeating the compression step. In this limit of the heat-bath polarization $\epsilon \ll 2^{-n}$, the polarization on C_2 will asymptotically approach 2ϵ [14].

The refresh step is achieved by selectively transferring polarization from the methylene protons $H_{m1,2}$ to the adjacent carbon C_m. Heteronuclear polarization transfer can be achieved through multiple pulse techniques or cross polarization (CP); we found CP better preserved the heat-bath polarization. Radio frequency fields drive two spin species at the same nutation frequency (Hartman-Hahn matching condition) which allows them to exchange polarization and their spin temperatures to equalize. During initial contact the polarization may coherently oscillate between strongly coupled proton and carbon spins [21] because, for the relevant input states, the CP condition gives an exchange Hamiltonian. Thus, a very short CP pulse can selectively swap the polarization from $H_{m1/m2}$ to C_m while negligibly affecting the much more weakly coupled C_1 and C_2. When a refresh step was required, the proton spin-locking power was smoothly reduced over 10 μs to the Hartman-Hahn matching condition for 25 μs and then smoothly returned to high power. Experimentally we found we could increase the polarization on C_m by $3.3\times$, similar to the enhancement from conventional CP (the theoretical maximum is $3.98\times$). It should be noted that although CP is the most common method for polarization enhancement of rare spins, it is not the most efficient. In certain cases, adiabatic demagnetization may be able to boost the polarization of the rare spins above the heat-bath bias [22].

The carbon control pulses are optimal control sequences implementing unitary quantum gates even though the PPA requires only classical gates that permute the diagonal elements of the density matrix. The pulses (see Fig. 2) are numerically optimized using the GRAPE algorithm

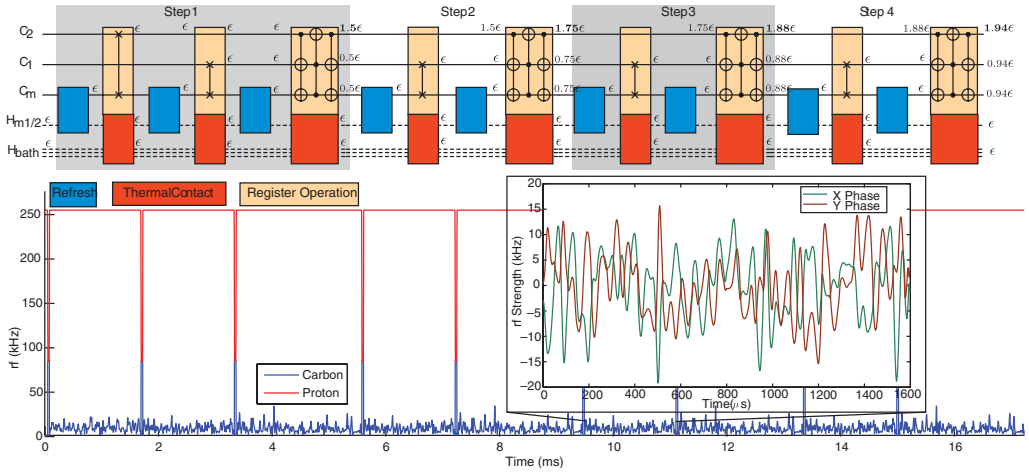

FIG. 2 (color online). The quantum circuit implemented (see text) with the ideal polarizations noted in terms of the heat-bath polarization ϵ. Each set of swap and compression gate is considered a step and the ideal polarization on the target qubit C_2 should increase as 1.5, 1.75, 1.88, 1.94 in steps 1 through 4. The refresh operations swap polarization from $H_{m1,2}$ to C_m with a short contact CP. The thermal contact between $H_{m1,2}$ and the rest of the proton bath takes place during the spin-locking decoupling pulse for the duration of the carbon register operations. The swap gates are 1.6 ms and the compression gate 2.2 ms. The compression gate is equivalent to a permutation of the diagonal elements of the density matrix, and one possible implementation is shown decomposed as C-NOT-NOT and Toffoli gates [14]; however, it was implemented as a single GRAPE pulse. The bottom trace shows the amplitude of the radio frequency control fields for the pulse sequence. The inset shows in detail the two quadrature components of one of the GRAPE control pulses which implements a unitary swap gate between qubits 1 and 3.

[23]—starting from a random guess the pulse is iteratively improved through a gradient ascent search. In bulk ensembles there are inevitable distributions of control parameters across the sample. In the current case these cause incoherent loss ($T_2^* \approx 2$ ms) at a much faster rate than the intrinsic $T_2 \approx 100$ ms [20]. In the present work the most important distributions are the static magnetic field and the rf control field. In order to obtain high experimental fidelities, it was important to demand that the pulses apply the same unitary gate across a range of static fields and pulsing powers. The GRAPE pulses were numerically optimized to have a fidelity $(|\mathrm{tr}(U_{\mathrm{goal}}^{\dagger} U_{\mathrm{sim}})|^2/2^{2n})$ of above 0.9975 averaged over a distribution of $\pm 5\%$ in rf amplitude and ± 150 Hz in static field. Although the inhomogeneities here are specific to ensemble systems, the utility of robust control will be applicable in single quantum systems for miscalibration, and uncertainty or slow drift in the Hamiltonian. The pulses were corrected for nonlinearities in the pulse generation and transmission to the sample through the use of a simple feedback circuit which measured the rf field at the sample and corrected the pulse accordingly. The most important element for achieving high fidelity control was to ensure that the control fields were within the bandwidth of the hardware. The finite bandwidth of the circuitry produces pulse distortions at switching points [24]. A solution is to use only smoothly varying control fields. Although limiting the bandwidth of the optimal control pulses may lead to longer than time-optimal pulses, incoherent sources of decoherence can still be refocused and higher experimental fidelities result.

With these improvements in control we were able to implement repeated rounds of cooling and compression. The polarization is increased for up to four compression steps as shown in Fig. 3. At that point, the polarization of C_2 is 1.69ϵ which is well above the Shannon bound of 1.5ϵ. Furthermore, we have built up a non-negligible polarization on the other two qubits of 0.84ϵ and 0.79ϵ increasing the total information content [17] of the system (see [25]). Our control is now limited by two factors. During the carbon control sequences, the protons are decoupled by the spin-locking pulse. This is equivalent to cw decoupling which gives poor decoupling bandwidth as a function of the decoupling power (limited by hardware constraints), particularly if the decoupled spins have strong dipolar couplings as in this case. Unfortunately, more efficient decoupling techniques such as SPINAL64 [26] do not preserve the magnetization of the decoupled spins, a necessity for this experiment. We are also limited by the nonideality of the heat bath: the proton system is a finite size and so every refresh step heats the bath. This amount is roughly calculated as the ratio of the number of carbons to protons. Given our 3% labeling ($^{13}C_3H_4O_4$) this is $\sim 0.5\%$. Furthermore, there is relaxation during the spin-locking pulses (T_1 in the rotating frame, $T_{1\rho}$) gradually warming the heat bath during the experiment.

This experiment represents a step towards creating pure qubits in systems where we have imperfect initialization.

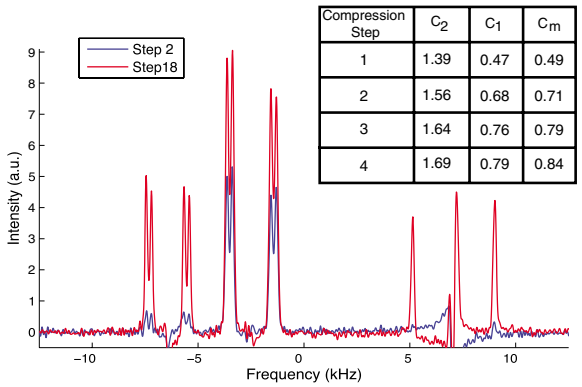

Compression Step	C_2	C_1	C_m
1	1.39	0.47	0.49
2	1.56	0.68	0.71
3	1.64	0.76	0.79
4	1.69	0.79	0.84

FIG. 3 (color online). Table of the measured polarization (with respect to the initial refresh step) of each spin after the compression gates (steps 6, 10, 14, 18 in the PPA). All results are ± 0.02. For the final compression step the heat-bath polarization is no longer needed which allows a switch from the spin-locking cw decoupling to the more efficient SPINAL64 [26] (without the switch the enhancement is $1.67\times$). The spectra show a comparison of the first refresh step (swapped to C_2) and the final signal after four compression steps. There is a clear boost of signal on C_2, and also substantial polarization on C_1 and C_m. The distortions in the spectrum evident for C_1 and C_m are due to residual natural abundance ^{13}C signal.

We have demonstrated that with sufficient control multiple rounds of cooling and compression can be achieved and the optimal control applied here should be applicable in other QIP systems. Future work will concentrate on starting with a reset step that has a sufficiently high polarization. Once errors are considered, perfectly pure qubits are no longer possible. These experiments, together with our recent work on error characterization [27], suggest an error per gate of approximately 1%. As noted above, this is largely limited by incomplete proton decoupling, a problem specific to this system, and not the control techniques themselves or decoherence. Even with an error model of a depolarizing rate of 1% per gate, simulations suggest that with 3/5 qubits, close to pure qubits with polarizations above 97% are possible with reset polarizations of only 87%/81%. Complete plots of the above threshold scaling behavior are available in Ref. [25]. These polarizations and number of controllable qubits are within reach in a variety of electron-nuclear systems [28,29]. For example, nitrogen vacancy electronic centers in diamond can be optically pumped to $\sim$80% [30], or the thermal bias of electron spins ($g \approx 2$) at cryogenic temperatures and typical fields of a few Tesla provides sufficient polarization.

C. R. would like to thank M. Ditty for his technical expertise with the spectrometer. This work was funded by NSERC, CFI, CIFAR, QuantumWorks, and DTO.

[1] M. A. Nielsen and I. L. Chuang, *Quantum Computation and Quantum Information* (Cambridge University Press, Cambridge, England, 2000).
[2] Special Issue on Experimental Aspects of Quantum Computing, edited by Henry Everitt, Quant. Info. Proc. **3**, 1 (2004).
[3] D. DiVincenzo, Fortschr. Phys. **48**, 771 (2000).
[4] J. Preskill, Proc. R. Soc. A **454**, 385 (1998).
[5] J. von Neumann, *Automata Studies* (Princeton University, Princeton, NJ, 1956), pp. 43–98.
[6] L. J. Schulman and U. V. Vazirani, arXiv:quant-ph/9804060v1.
[7] L. J. Schulman and U. V. Vazirani, in *Proceedings of the Symposium on Theory Of Computing (STOC '99), Atlanta, 1999* (ACM, New York, 1999), pp. 322–329.
[8] O. Sorensen, Prog. Nucl. Magn. Reson. Spectrosc. **21**, 503 (1989).
[9] P. O. Boykin *et al.*, Proc. Natl. Acad. Sci. U.S.A. **99**, 3388 (2002).
[10] J. M. Fernandez *et al.*, Int. J. Quantum. Inform. **2**, 461 (2004).
[11] F. Rempp, M. Michel, and G. Mahler, Phys. Rev. A **76**, 032325 (2007).
[12] P. Kaye, arXiv:quant-ph/0703194v3.
[13] L. J. Schulman, T. Mor, and Y. Weinstein, Phys. Rev. Lett. **94**, 120501 (2005).
[14] O. Moussa, Master's thesis, University of Waterloo, 2005.
[15] M. Sarovar and G. J. Milburn, Phys. Rev. A **72**, 012306 (2005).
[16] D. E. Chang, L. M. K. Vandersypen, and M. Steffen, Chem. Phys. Lett. **338**, 337 (2001).
[17] G. Brassard *et al.*, arXiv:quant-ph/0511156v1.
[18] J. Baugh *et al.*, Nature (London) **438**, 470 (2005).
[19] L. M. K. Vandersypen and I. L. Chuang, Rev. Mod. Phys. **76**, 1037 (2005).
[20] J. Baugh *et al.*, Phys. Rev. A **73**, 022305 (2006).
[21] L. Müller *et al.*, Phys. Rev. Lett. **32**, 1402 (1974).
[22] J.-S. Lee and A. Khitrin, J. Magn. Reson. **177**, 152 (2005).
[23] N. Khaneja *et al.*, J. Magn. Reson. **172**, 296 (2005).
[24] T. M. Barbara, J. F. Martin, and J. G. Wurl, J. Magn. Reson. **93**, 497 (1991).
[25] See EPAPS Document No. E-PRLTAO-100-060814 for a figure showing the information content of each step of the algorightm and a one-page pdf showing plots of the total information content of the system as it is purified and the behavior of the above threshold scaling of the purification protocol. For more information on EPAPS, see http://www.aip.org/pubservs/epaps.html.
[26] B. M. Fung, A. K. Khitrin, and K. Ermolaev, J. Magn. Reson. **142**, 97 (2000).
[27] J. Emerson *et al.*, Science **317**, 1893 (2007).
[28] C. Negrevergne *et al.*, Phys. Rev. Lett. **96**, 170501 (2006).
[29] J. S. Hodges *et al.*, arXiv:quant-ph/0707.2956.
[30] J. Harrison, M. J. Sellars, and N. B. Manson, Diam. Relat. Mater. **15**, 586 (2006).
[31] R. McCalley and A. L. Kwiram, J. Phys. Chem. **97**, 2888 (1993).

E.2 Symmetrized characterization of noisy quantum processes

Fully characterizing quantum processes is a very daunting task as the number of parameters describing a process grows doubly exponential. One is left to wonder if it is worth it to go through the effort of acquiring all the information about a process – to what end? If one wishes to extract a certain piece of information about a process –like whether it can be described by a Markovian master equation, or what the probabilities of one or two qubit errors are– then why not measure it directly. This work about finding an efficient way to access relevant partial information about a quantum process.

The idea was J.Emerson's brainchild, and he came up with the first algorithm. R.Laflamme adapted the algorithm to the NMR setting for the special case of two qubits. My first contribution was to generalize the NMR version to an arbitrary number of qubits, and figure out how to extract the relevant information from the NMR experiments. I also helped in designing the test cases for the experimental demonstration in liquid state and solid state. I analysed the data using a maximum likelihood algorithm to extract the relevant information from the data.

I am also very proud of the figures in this paper – I designed and produced them all save for Figure 2 in the supplementary material.

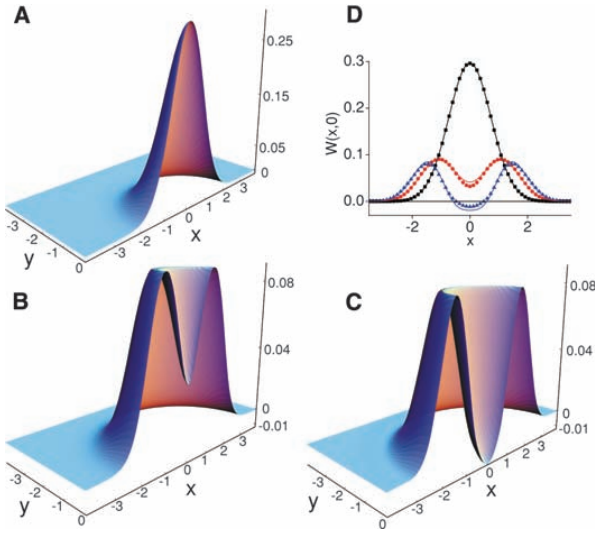

Fig. 4. Experimental WFs (corrected for detection inefficiency) for (**A**) the original thermal state; (**B**) the photon-added-then-subtracted state; (**C**) the photon-subtracted-then-added state. (**D**) presents sections of the above Wigner functions (black squares correspond to the thermal field; red circles and blue triangles correspond to the photon-added-then-subtracted and the photon-subtracted-then-added states, respectively), together with the corresponding theoretical predictions (solid curves) (*2*).

verse order, as in this case, is the real essence of the Heisenberg uncertainty principle. Besides its fundamental importance, the experimental implementation of such a sequence of basic quantum operations is an essential tool for the full-scale engineering of a quantum light state optimized for a multitude of different tasks (*15*), including robust quantum communication. As any quantum operation, including non-Gaussian operations, is composed of photon additions and subtractions (i.e, it can be expressed as $f(\hat{a},\hat{a}^{\dagger})$), our experimental results constitute a step toward the full quantum control of a field and the generation of highly entangled states (*16*).

References and Notes

1. P. A. M. Dirac, *The Principles of Quantum Mechanics* (Oxford Press, 1954).
2. Materials and methods are available as supporting material on *Science* Online.
3. A. Zavatta, S. Viciani, M. Bellini, *Science* **306**, 660 (2004).
4. A. Zavatta, S. Viciani, M. Bellini, *Phys. Rev. A* **72**, 023820 (2005).
5. A. Zavatta, V. Parigi, M. Bellini, *Phys. Rev. A* **75**, 052106 (2007).
6. C. T. Lee, *Phys. Rev. A* **52**, 3374 (1995).
7. J. Wenger, R. Tualle-Brouri, P. Grangier, *Phys. Rev. Lett.* **92**, 153601 (2004).
8. M. S. Kim, E. Park, P. L. Knight, H. Jeong, *Phys. Rev. A* **71**, 043805 (2005).
9. A. Zavatta, M. Bellini, P. L. Ramazza, F. Marin, F. T. Arecchi, *J. Opt. Soc. Am. B* **19**, 1189 (2002).
10. K. Banaszek, G. M. D'Ariano, M. G. A. Paris, M. F. Sacchi, *Phys. Rev. A* **61**, 010304(R) (1999).
11. A. I. Lvovsky, *J. Opt. B: Quantum Semiclassical Opt.* **6**, S556 (2004).
12. Z. Hradil, D. Mogilevtsev, J. Rehacek, *Phys. Rev. Lett.* **96**, 230401 (2006).
13. U. Leonhardt, *Measuring the Quantum State of Light* (Cambridge University Press, Cambridge, 1997).
14. Note that the positivity of the WF in the case of the add-then-subtract sequence is not due to experimental imperfections. As for squeezed states, the resulting state can be shown to be nonclassical (with a negative P function), although possessing a positive WF.
15. F. Dell'Anno, S. De Siena, F. Illuminati, *Phys. Rep.* **428**, 53 (2006).
16. J. Eisert, S. Scheel, M. B. Plenio, *Phys. Rev. Lett.* **89**, 137903 (2002).

17. We thank F. T. Arecchi, A. Montina, and E. Park for helpful comments and for a critical reading of the manuscript, and P. Poggi for the improvement of detection electronics. This work was partially supported by Ente Cassa di Risparmio di Firenze and by the Italian Ministry of University and Scientific Research, under the PRIN 2005 initiative. M.S.K. acknowledges financial support from the UK Engineering and Physical Science Research Council (EPSRC) and Quantum Information Processing Interdisciplinary Research Centre (QIPIRC).

Supporting Online Material

www.sciencemag.org/cgi/content/full/317/5846/1890/DC1
Materials and Methods
References and Notes

7 June 2007; accepted 10 August 2007
10.1126/science.1146204

Symmetrized Characterization of Noisy Quantum Processes

Joseph Emerson,[1,2] Marcus Silva,[2,3] Osama Moussa,[2,3] Colm Ryan,[2,3] Martin Laforest,[2,3] Jonathan Baugh,[2] David G. Cory,[4] Raymond Laflamme[2,3,5]

A major goal of developing high-precision control of many-body quantum systems is to realize their potential as quantum computers. A substantial obstacle to this is the extreme fragility of quantum systems to "decoherence" from environmental noise and other control limitations. Although quantum computation is possible if the noise affecting the quantum system satisfies certain conditions, existing methods for noise characterization are intractable for present multibody systems. We introduce a technique based on symmetrization that enables direct experimental measurement of some key properties of the decoherence affecting a quantum system. Our method reduces the number of experiments required from exponential to polynomial in the number of subsystems. The technique is demonstrated for the optimization of control over nuclear spins in the solid state.

Quantum information enables efficient solutions to certain tasks that have no known efficient solution in the classical world, and it has reshaped our understanding of computational complexity. Harnessing the advantages of the quantum world requires the ability to robustly control quantum systems and, in particular, counteract the noise and decoherence affecting any physical realization of quantum information processors (QIPs). A pivotal step in this direction came with the discovery of quantum error correction codes (QECCs) (*1*, *2*) and the threshold theorem for fault-tolerant (FT) quantum computation (*3*–*6*). To make use of quantum error correction and produce fault-tolerant protocols, we need to understand the nature of the noise affecting the system at hand. There is a direct way to fully characterize the noise using a procedure known as process tomography (*7*–*9*). However, this procedure requires resources that grow exponentially with the number of subsystems (usually two-level systems called "qubits") and is intractable for characterizing the multi-qubit quantum systems that are presently realized

[1]Department of Applied Math, University of Waterloo, Waterloo, ON N2L 3G1, Canada. [2]Institute for Quantum Computing, University of Waterloo, Waterloo, ON N2L 3G1, Canada. [3]Department of Physics and Astronomy, University of Waterloo, Waterloo, ON N2L 3G1, Canada. [4]Department of Nuclear Science and Engineering, Massachusetts Institute of Technology, Cambridge, MA 02139, USA. [5]Perimeter Institute for Theoretical Physics, Waterloo, ON N2L 2Y5, Canada.

(*10*–*12*). We introduce a general symmetrization method that allows for direct experimental characterization of some physically relevant features of the decoherence and apply it to develop an efficient experimental protocol for measuring multiqubit correlations and memory effects in the noise. Compared with existing methods (*13*), the protocol yields an exponential savings in the number of experiments required to obtain such information. In the context of applications, this information enables optimization of error-correction strategy and tests of some assumptions underlying estimates of the FT threshold. Moreover, the estimated parameters are immediately relevant for optimizing experimental control methods.

Focusing on a system of n qubits, a complete description of a general noise model Λ requires $O(2^{4n})$ parameters. Clearly an appropriate coarse-graining of this information is required; the challenge is to identify efficient methods for estimating the features of practical interest. The method we propose is based on identifying a symmetry associated with a property of interest, and then operationally symmetrizing the noise to yield an effective map $\overline{\Lambda}$, with a reduced number of independent parameters reflecting these properties (Fig. 1). This symmetrization is achieved by conjugating the noise (Fig. 2) with a unitary operator drawn randomly from the relevant symmetry group and then averaging over these random trials (*14*–*18*). We show below that rigorous statistical bounds guarantee that the number of experimental trials required is independent of the dimension of the group. Hence, our randomization method leads to efficient partial characterization of the map Λ whenever the group elements admit efficient circuit decompositions.

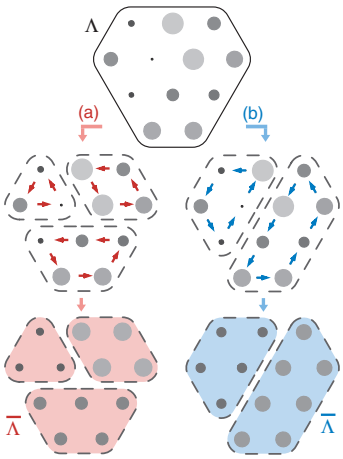

Fig. 1. Schematic of coarse-graining by symmetrization. Averaging the noise Λ by twirling under a symmetry group yields an effective noise process that has a reduced number of independent parameters. Distinct symmetrization groups [represented by (a) red and (b) blue] uniformize different subsets of parameters.

We apply this general idea to the important problem of estimating the noise parameters that determine the performance of a broad class of QECCs and the applicability of certain assumptions underlying FT thresholds. In general, QECCs protect quantum information only against certain types of noise. A distance-$(2t + 1)$ code refers to codes that correct all errors simultaneously, affecting up to t qubits. Hence, the distance of a QECC determines which terms in the noise will be corrected and which will remain uncorrected. The latter contribute to the overall failure probability. To estimate the failure probability, many fault-tolerance theorems assume that the noise is independent from qubit to qubit or between blocks of qubits. Another common assumption is that the noise is memoryless and hence Markovian in time. Our protocol enables measurements of these noise correlations under a given experimental arrangement without the exponential overhead of process tomography. This protocol is efficient also in the context of an ensemble QIP with highly mixed states (*19*).

We start by expanding the noise operators in the basis $P_i \in \mathcal{P}_n$, consisting of n-fold tensor product of the usual single-qubit Pauli operators $\{1, X, Y, Z\}$ satisfying the orthogonality relation $\mathrm{Tr}[P_i\ P_j] = 2^n\ \delta_{ij}$. The Clifford group $\mathcal{C}_n$ is defined as the normalizer of the Pauli group $\mathcal{P}_n$: it consists of all elements U_i of the unitary group $U(2^n)$ satisfying $U_i P_j U_i^\dagger \in \mathcal{P}_n$ for every $P_j \in \mathcal{P}_n$. The protocol requires symmetrizing the channel $\Lambda \rightarrow \overline{\Lambda}$ by averaging over trials in which the channel is conjugated by the elements of $\mathcal{C}_1$ applied independently to each qubit (Fig. 2). An average over conjugations is known as a "twirl" (*20*), and we call the above a $\mathcal{C}_1^{\otimes n}$-twirl.

Separating out terms according to their Pauli weight w, where $w \in \{0,...,n\}$ is the number of nonidentity factors in P_l, letting the index $\mathrm{v}_w \in \{1, ..., \binom{n}{w}\}$ count the number of distinct ways that w nonidentity Pauli operators can be distributed over the n factor spaces, and the index $\mathbf{i}_w = \{i_1, ..., i_w\}$ with $i_j \in \{1, 2, 3\}$ denote which of the nonidentity Pauli operators occupies the j^{th} occupied site, we obtain (see SOM text)

$$\overline{\Lambda(\rho)} = \sum_{w=0}^{n} \sum_{\mathrm{v}_w=1}^{\binom{n}{w}} r_{w,\mathrm{v}_w} \sum_{\mathbf{i}_w} P_{w,\mathrm{v}_w,\mathbf{i}_w} \rho P_{w,\mathrm{v}_w,\mathbf{i}_w} \quad (1)$$

where the reduced parameters $r_{w,\mathrm{v}w}$ are fixed by Λ and $p_w = 3^w \sum_{\mathrm{v}_w=1}^{\binom{n}{w}} r_{w,\mathrm{v}w}$ are the probabilities of w simultaneous qubit errors in the noise. Some intuition about how a $\mathcal{C}_1^{\otimes n}$-twirl simplifies the task of noise characterization is obtained by analyzing the case of a single qubit (SOM text).

To measure these probabilities, we probe $\overline{\Lambda}$ with input state $|0\rangle \equiv |\ 0\rangle^{\otimes n}$, followed by a projective measurement of the output state in the basis $|l\rangle$. This yields an n-bit string $l \in \{0, 1\}^n$. Let q_w denote the probability that a random subset of w bits of the binary string l has even parity. This gives the eigenvalues of $\overline{\Lambda}$ as $c_w \equiv \langle \overline{Z^{\otimes w}} \rangle = 2q_w - 1$, and we obtain $p_{w'} = \sum_w \Omega^{-1}_{w',w} c_w$,

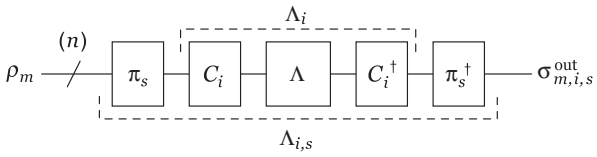

Fig. 2. Quantum circuit. One experimental run consists of a conjugation of the noise process Λ. The standard protocol requires conjugation only by an element C_i, whereas the ensemble protocol requires conjugating Λ also by a permutation π_s of the qubits. The standard protocol requires only one input state $|\ 0\rangle^{\otimes n}$, whereas the ensemble protocol requires n distinct input operators ρ_w.

Table 1. Summary of experimental results. The first four sets of experiments (three sets on the two-qubit liquid-state system and one on the three-qubit solid-state system) were designed to characterize the performance of the protocol under engineered noise. The final two sets demonstrate characterization of the (unknown) natural noise affecting the quantum memory created by multiple-pulse time-suspension sequences with different pulse spacings.

No.	System	Map description	Kraus operators (A_k)	k	p_0	p_1	p_2	p_3
1	$CHCl_3$	Engineered: $\mathbf{p}$ = [0,1,0].	$\frac{1}{\sqrt{2}}\{Z_1, Z_2\}$	288	$0.000^{+0.004}$	$0.991^{+0.009}_{-0.015}$	$0.009^{+0.017}_{-0.009}$	-
2	$CHCl_3$	Engineered: $\mathbf{p}$ = [0,0,1].	$\{Z_1\ Z_2\}$	288	$0.001^{+0.006}_{-0.001}$	$0.004^{+0.011}_{-0.004}$	$0.996^{+0.004}_{-0.011}$	-
3	$CHCl_3$	Engineered: $\mathbf{p} = [\frac{1}{4}, \frac{1}{2}, \frac{1}{4}]$.	$\{\exp[i\frac{\pi}{4}(Z_1 + Z_2)]\}$	288	$0.254^{+0.010}_{-0.010}$	$0.495^{+0.021}_{-0.020}$	$0.250^{+0.019}_{-0.019}$	-
4	$C_3H_4O_4$	Engineered: $\mathbf{p}$ = [0,1,0,0].	$\frac{1}{\sqrt{3}}\{Z_1, Z_2, Z_3\}$	432	$0.01^{+0.01}_{-0.01}$	$0.99^{+0.01}_{-0.03}$	$0.01^{+0.02}_{-0.01}$	$0.00^{+0.01}$
5	$C_3H_4O_4$	Natural Noise (i)	unknown	432	$0.44^{+0.01}_{-0.02}$	$0.45^{+0.03}_{-0.03}$	$0.10^{+0.04}_{-0.08}$	$0.01^{+0.03}_{-0.01}$
6	$C_3H_4O_4$	Natural Noise (ii)	unknown	432	$0.84^{+0.01}_{-0.01}$	$0.15^{+0.02}_{-0.03}$	$0.01^{+0.03}_{-0.01}$	$0.00^{+0.02}$

where the matrix $\Omega^{-1}_{w',w}$ is a matrix of combinatorial factors (SOM text). If in each single-shot experiment, the Clifford operators are chosen uniformly at random, then with $K = O[\log(2n)/\delta^2]$ experiments we can estimate each of the coefficients c_w to precision δ with constant probability. All imperfections in the protocol contribute to the total probabilities of error. The protocol can be made robust against imperfections in the input state preparation, measurement, and twirling by factoring out the values $c_w(0)$ measured when the protocol is performed without the noisy channel: $c_w \rightarrow \tilde{c}_w = c_w/c_w(0)$.

The c_w can be applied directly to test some of the assumptions that affect estimates of the fault-tolerance threshold (*21*, *22*). In particular, a noisy channel with an uncorrelated distribution of error locations, but with arbitrary correlations in the error type, is mapped under our symmetrization to a channel that is a tensor product of n single-qubit depolarizing channels. A channel satisfying this property will exhibit the scaling $c_w = c_1^w$. Hence, observed deviations from this scaling imply a violation of the above assumption. However, there are correlated error models that also give rise to this scaling, so the converse implication does not hold.

Furthermore, we can test for non-Markovian properties by repeating the above scheme for distinct time intervals $m\tau$ with increasing m. If, over the time scale τ, the noise satisfies the Markovian semigroup property $\Lambda_\tau \circ \Lambda_\tau = \Lambda_{2\tau}$ (*23*), then so will the twirled map $\overline{\Lambda}_\tau \circ \overline{\Lambda}_\tau = \overline{\Lambda}_{2\tau}$. Consequently, the coefficients $c_w(m\tau)$ measured over the time-scale $m\tau$ will satisfy $c_w(m\tau) = c_w(\tau)^m$. Observed deviations from this scaling imply non-Markovian effects in the untwirled noise. However, again the converse does not hold; consistency with this scaling does not guarantee that the untwirled noise obeys the Markovian semigroup property.

When applying $\{c_w\}$ to estimate $\{p_w\}$, the statistical uncertainty for p_w grows exponentially with w (SOM text). This still allows for characterization of other important features of the noise. Specifically, the probability p_0 is directly related to the entanglement fidelity of the channel, so this protocol provides an exponential savings over recently proposed methods for estimating this single figure of merit (*16*, *24*, *25*). [For another approach, see (*17*)]. Hence, by actually implementing any given code, we can bound the failure probability of that code with only $O[\log(2n)/\delta^2]$ experiments and without making any theoretical assumptions about the noise. Moreover, on physical grounds, we may expect the noise to become independent between qubits outside some fixed (but unknown) scale b, after which the p_w decreases exponentially with w. The scale b can be determined efficiently with $O(n^b)$ experiments.

Although a characterization of the twirled channel is useful given the relevance of twirled channels in some fault-tolerant protocols (*22*), the failure probability of the twirled channel gives an upper bound to the failure probability of the original untwirled channel whenever the performance of the code has some bound that is invariant under the symmetry associated with the twirl. This holds quite generally in the context of the symmetry considered above because the failure probability of a generic distance-$(2t + 1)$ code is bounded above by the total probability of error terms with Pauli weight greater than t, and this weight remains invariant under conjugation by any $C_i \in \mathcal{C}_1^{\otimes n}$.

Our protocol is efficient also in the context of an ensemble QIP (*19*). We prepare deviations from the identity state of the form $\rho_w = Z^{\otimes w} \otimes 1^{\otimes(n-w)}$, with $w \in \{1, \ldots n\}$; hence, the (non-scalable) preparation of pseudo-pure states is avoided. As illustrated in Fig. 2, the ensemble protocol consists of conjugating the process $\Lambda \rightarrow \Lambda_{i,s}$ with a randomly chosen pair (C_i, π_s) in each run, where π_s is a random permutation of the qubits. For input operator ρ_w, the output is $\sigma^{out}_{w,i,s} = \Lambda_{i,s}(\rho_w)$. Averaging the output operators $\sigma^{out}_{w,i,s}$ over i and s returns the input operator scaled by c_w.

We performed an implementation of the above protocol on both a two-qubit (chloroform $CHCl_3$) liquid-state and a three-qubit (single-crystal Malonic acid $C_3H_4O_4$) solid-state nuclear magnetic resonance QIP (*26*). The results of these experiments are summarized in Table 1. Statistical analysis for one liquid-state set is shown in fig. S1 and for the final two solid-state sets in Fig. 3. The final two sets of (solid-state) experiments were performed to characterize the unknown residual noise occurring under (i) one cycle of a C48 pulse sequence (*27*) with 10 μs pulse spacing, and (ii) two cycles of C48 with 5 μs pulse spacing. The C48 sequence is designed to suppress the dynamics due to the system's internal Hamiltonian and could be used, for example, for quantum memory. The evolution of the system under this pulse sequence can be evaluated theoretically by calculating the Magnus expansion (*28*) of the associated effective Hamiltonian, under which the residual effects appear as a sum of terms associated with the Zeeman and dipolar parts of the Hamiltonian, including cross terms. Roughly speaking, effective suppression of the k^{th} term of the Hamiltonian takes places when $\gamma_k \tau_k << 1$, where γ_k is the strength of the term and τ_k^{-1} is the rate at which it is modulated by the pulse sequence. Generally, shorter delays lead to improved performance unless there is a competing process at the shorter time scale. Although two repetitions of the sequence with the pulse spacing of 5 μs has twice as many pulses as the single sequence with the 10 μs spacing, the probabilities of one-, two-, and three-body noise terms all decrease substantially (Table 1). However, the averaging under the 5 μs falls short of ideal performance as a result of incomplete (heteronuclear) decoupling of the qubits (three carbon nuclei) from the envi-

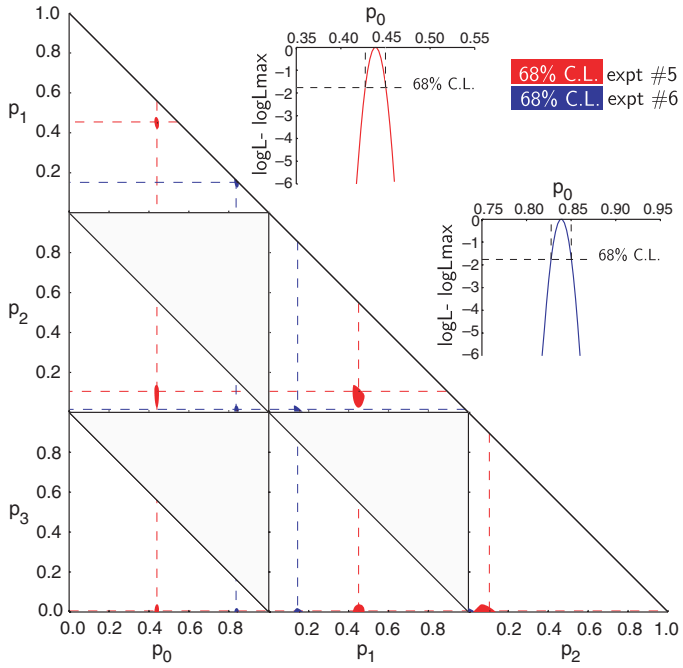

Fig. 3. Results for p_w from experiments 5 and 6 in Table 1. Shown are projections of the four-dimensional likelihood function onto various probability planes. The asymmetry seen in some of the confidence areas is a result of this projection. The results for one cycle with 10 μs pulse spacing (experiment 5) are in red, and the results for two cycles with 5 μs spacing (experiment 6) are in blue.

ronment (nearby hydrogen nuclei) (SOM text). For both sequences, the noise coefficients c_w do not statistically deviate from the scaling implied by uncorrelated errors (fig. S3), although, as noted above, this does not guarantee that the errors are uncorrelated.

Our method provides an efficient protocol for the characterization of noise in contexts where the target transformation is the identity operator, for example, a quantum communication channel or quantum memory. However, the protocol also provides an efficient means for characterizing the noise under the action of a nonidentity unitary transformation. One approach is to decompose the unitary transformation into a product of basic quantum gates drawn from a universal gate set, where each gate in the set acts on at most 2 qubits simultaneously. Hence, the noise map acting on all n qubits associated with any two-qubit gate can be determined by applying the above protocol to other $n-2$ qubits while applying process tomography to the two qubits in the quantum gate. Another approach is to estimate the average error per gate for a sequence of m gates, such that the composition gives the identity operator. Such a sequence can be generated by making use of the cyclic property $U^m = 1$ of any gate in a universal gate set or by choosing a sequence of $m-1$ random gates followed by an m^{th} gate chosen such that the composition gives the identity transformation.

References and Notes

1. P. W. Shor, *Phys. Rev. A* **52**, R2493 (1995).
2. A. M. Steane, *Phys. Rev. Lett.* **77**, 793 (1996).
3. P. W. Shor, *Proceedings of the Symposium on the Foundations of Computer Science,* 56 (IEEE press, Los Alamitos, California, 1996).
4. D. Aharonov, M. Ben-Or, *Proceedings of the 29th Annual ACM Symposium on the Theory of Computing,* 176 (ACM Press, New York, 1996).
5. A. Y. Kitaev, *Uspekhi Mat. Nauk.* **52**, 53 (1997).
6. E. Knill, R. Laflamme, W. Zurek, *Science* **279**, 342 (1998).
7. I. Chuang, M. Nielsen, *J. Mod. Opt.* **44**, 2455 (1997).
8. G. M. D'Ariano, P. Lo Presti, *Phys. Rev. Lett.* **86**, 4195 (2001).
9. M. Mohseni, D. Lidar, *Phys. Rev. Lett.* **97**, 170501 (2006).
10. H. Haffner *et al.*, *Nature* **438**, 643 (2005).
11. D. Leibfried *et al.*, *Nature* **438**, 639 (2005).
12. C. Negrevergne *et al.*, *Phys. Rev. Lett.* **96**, 170501 (2006).
13. A. Childs, I. Chuang, D. Leung, *Phys. Rev. A* **64**, 012314 (2001).
14. J. Emerson, Y. Weinstein, M. Saraceno, S. Lloyd, D. Cory, *Science* **302**, 2098 (2003).
15. B. Levi, C. Lopez, J. Emerson, D. G. Cory, *Phys. Rev. A* **75**, 022314 (2007).
16. J. Emerson, R. Alicki, K. Zyczkowski, *J. Opt. B: Quantum and Semiclassical Optics* **7**, S347 (2005).
17. C. Dankert, R. Cleve, J. Emerson, E. Livine, quant-ph/0606161 (2006).
18. W. Dur, M. Hein, J. Cirac, H.-J. Briegel, *Phys. Rev. A* **72**, 052326 (2005).
19. D. G. Cory *et al.*, *Fortschr. Phys.* **48**, 875 (2000).
20. C. Bennett, D. DiVincenzo, J. Smolin, W. Wootters, *Phys. Rev. A* **54**, 3824 (1996).
21. P. Aliferis, D. Gottesman, J. Preskill, *Quant. Inf. Comp* **6**, 97 (2006).
22. E. Knill, *Nature* **434**, 39 (2005).
23. R. Alicki, K. Lendi, *Quantum Dynamical Semigroups and Applications*, Lecture Notes in Physics **286**, 12 (1987).
24. E. Fortunato *et al.*, *J. Chem. Phys.* **116**, 7599 (2002).
25. M. Nielson, *Phys. Lett. A* **303**, 249 (2002).
26. Materials and methods are available as supporting material on *Science* Online.
27. D. G. Cory, J. B. Miller, A. N. Garroway, *J. Magn. Reson.* **90**, 205 (1990).
28. U. Haeberlen, *Advances in Magnetic Resonance*, Ed. J. Waugh, Academic Press, New York (1976).

29. This work benefited from discussions with R. Blume-Kohout, R. Cleve, M. Ditty, D. Gottesman, E. Knill, B. Levi, and A. Nayak and was supported by the National Science and Engineering Research Council of Canada (NSERC) grants 250673 and 327778, Ontario Research Development Challenge Fund (ORDCF) grant 3232301-05, Army Research Office/Laboratory for Physical Sciences (ARO/LPS) grant W911NF-05-1-0469, and Army Research Office/Mathematics of Information Technology and Complex Systems (ARO/MITACS) grant W911NF-05-1-0298.

Supporting Online Material

www.sciencemag.org/cgi/content/full/317/5846/1893/DC1
Materials and Methods
SOM Text
Figs. S1 to S3
References

25 May 2007; accepted 29 August 2007
10.1126/science.1145699

Nuclei-Induced Frequency Focusing of Electron Spin Coherence

A. Greilich,[1]* A. Shabaev,[2,3]* D. R. Yakovlev,[1,4] Al. L. Efros,[2]† I. A. Yugova,[1,5] D. Reuter,[6] A. D. Wieck,[6] M. Bayer[1]†

The hyperfine interaction of an electron with the nuclei is considered as the primary obstacle to coherent control of the electron spin in semiconductor quantum dots. We show, however, that the nuclei in singly charged quantum dots act constructively by focusing the electron spin precession about a magnetic field into well-defined modes synchronized with a laser pulse protocol. In a dot with a synchronized electron, the light-stimulated fluctuations of the hyperfine nuclear field acting on the electron are suppressed. The information about electron spin precession is imprinted in the nuclei and thereby can be stored for tens of minutes in darkness. The frequency focusing drives an electron spin ensemble into dephasing-free subspaces with the potential to realize single frequency precession of the entire ensemble.

The possibility of encoding quantum information in the spins of quantum dot (QD) electrons has attracted considerable attention (*1*, *2*). The spatial confinement protects the spins against the primary relaxation mechanisms in bulk, all of which arise from coupling of spin and orbital momenta. However, the electron hyperfine interaction with the lattice nuclei is enhanced by confinement, leading to spin decoherence and dephasing (*3*–*10*) and thus posing severe difficulties for processing quantum information. General schemes for suppressing decoherence have been discussed already (*11*). Electron spin relaxation in QDs may be overcome by polarizing the nuclear spins (*12*, *13*), but the high degree of polarization required, close to 100% (*12*), has not been achieved yet (*14*–*16*).

We find that the hyperfine interaction, rather than being detrimental, can be used as a precision tool by demonstrating that it modifies the continuous mode spectrum of the electron spin precession in a QD ensemble into a few discrete modes. The information on this digital spectrum can be stored in the nuclear spin system for tens of minutes because of the long nuclear memory times (*17*, *18*).

In a QD ensemble, fast electron spin dephasing arises not only from nuclear field fluctuations but also from variations of the electron g factor, leading to different spin precession frequencies. The dephasing due to these unavoidable variations can be partly overcome by mode-locking (*19*), which synchronizes the precession of specific electron spin modes in the ensemble with the clocking rate of a periodic pulsed laser. Still, it leaves a substantial fraction of dephased electron spins, whose precession frequencies do not satisfy the mode locking conditions. We demonstrate that the nuclear spin polarization adjusts the electron spin precession frequency in each quantum dot such that the whole ensemble becomes locked on very few frequencies.

The experiments were done on an ensemble of self-assembled (In,Ga)As/GaAs QDs (*19*, *20*), each dot containing on average a single electron (*21*). The electron spin precession about a perpendicular magnetic field was studied by a pump-probe Faraday rotation (FR) technique with ps time resolution (*22*). Spin coherence is generated

[1]Experimentelle Physik II, Universität Dortmund, D-44221 Dortmund, Germany. [2]Naval Research Laboratory, Washington, DC 20375, USA. [3]School of Computational Sciences, George Mason University, Fairfax, VA 22030, USA. [4]A. F. Ioffe Physico-Technical Institute, 194021 St. Petersburg, Russia. [5]Institute of Physics, St. Petersburg State University, 1908504 St. Petersburg, Russia. [6]Angewandte Festkörperphysik, Ruhr-Universität Bochum, D-44780 Bochum, Germany.

*These authors contributed equally to this work.
†To whom correspondence should be addressed. E-mail: efros@dave.nrl.navy.mil; manfred.bayer@physik.uni-dortmund.de

Symmetrised Characterisation of Noisy Quantum Processes

Joseph Emerson,[1,2] Marcus Silva,[3,2] Osama Moussa,[3,2] Colm Ryan,[3,2] Martin Laforest,[3,2] Jonathan Baugh,[2] David G. Cory,[4] and Raymond Laflamme[3,2]

[1]*Department of Applied Mathematics, University of Waterloo, Waterloo, ON N2L 3G1, Canada*
[2]*Institute for Quantum Computing, University of Waterloo, Waterloo, ON N2L 3G1, Canada*
[3]*Department of Physics and Astronomy, University of Waterloo, Waterloo, ON N2L 3G1, Canada*
[4]*Department of Nuclear Science and Engineering, Massachusetts Institute of Technology, Cambridge, MA 02139, USA*

Supporting Online Material

Materials and Methods

The two-qubit liquid-state experiments were performed on a sample made from 10mg of ^{13}C labeled chloroform (Cambridge Isotopes) dissolved in 0.51ml of deuterated acetone. The experiment was performed on a 700MHz Bruker Avance spectrometer using a dual inverse cryoprobe. The pulse programs were optimized on a home-built pulse sequence compiler which pre-simulates the pulses in an efficient pairwise manner and takes into account first order phase and coupling errors during a pulse by modifications of the refocussing scheme and pulse phases [1]. The solid-state experiments were performed on a single crystal of malonic acid which contained ≈7% triply labeled ^{13}C molecules [2]. The experiments were performed at room temperature with a home-built probe. Apart from an initial polarization transfer, the protons were decoupled using the SPINAL64 sequence [3]. The required control fields that implemented the unitary propagators and state-to-state transformations were found using the GRAPE optimal control method [4] and made robust to inhomogeneities in both the r.f. and static fields. The implemented versions of the pulses were corrected for non-linearities in the signal generation and amplification process through a pickup coil to measure the r.f. field at the sample and a simple feedback loop.

The error probabilities for each experiment were calculated using a constrained maximum likelihood function. The results of this analysis for one of the liquid-state experiments are shown in Fig. S1.

Supporting Text

Effect of Clifford Twirling on a Single Qubit

We can give some intuitive idea of how twirling leads to a reduction of the number of independent parameters by considering the case of a noisy channel for a single qubit. To demonstrate the main idea most directly, we consider a simple stochastic noise model of the form

$$\Lambda(\rho) = p_o 1\rho 1 + p_x X\rho X + p_y Y\rho Y + p_z Z\rho Z$$

which has three independent parameters (where $p_o + p_x + p_y + p_z = 1$). Under conjugation, the Clifford operators map each non-identity Pauli operator to another Pauli operator [5]. For example, conjugation of the Pauli operators under the Hadamard gate H, which is an element of the Clifford group, has the following effect: $HXH^\dagger = HXH = Z$, $HYH = -Y$, and $HZH = X$. Hence the H-conjugated noise model takes the form

$$H\Lambda(H\rho H)H = p_o 1\rho 1 + p_x Z\rho Z + p_y Y\rho Y + p_z X\rho X.$$

More generally, the 12 elements of the Clifford group for a single qubit divide into subsets of operators, where the elements of each subset map each non-identity Pauli to one of the three possible non-identity Pauli's. By averaging over each possible conjugation (operationally defined by the circuit given in Fig. 2), each of the possible Pauli errors becomes equiprobable, and the noise model transforms to the twirled form

$$\Lambda(\rho) \to \overline{\Lambda}(\rho) = p_o\rho + (p_1/3)(X\rho X + Y\rho Y + Z\rho Z),$$

where $p_1 = p_x + p_y + p_z$. As a result, we only need to estimate the probability of any one Pauli error in the twirled channel, and from that we can estimate the total probability of all 3 distinct single qubit Pauli errors in the un-twirled channel. The general analysis of a $\mathcal{C}_1^{\otimes n}$-twirl is described in detail below.

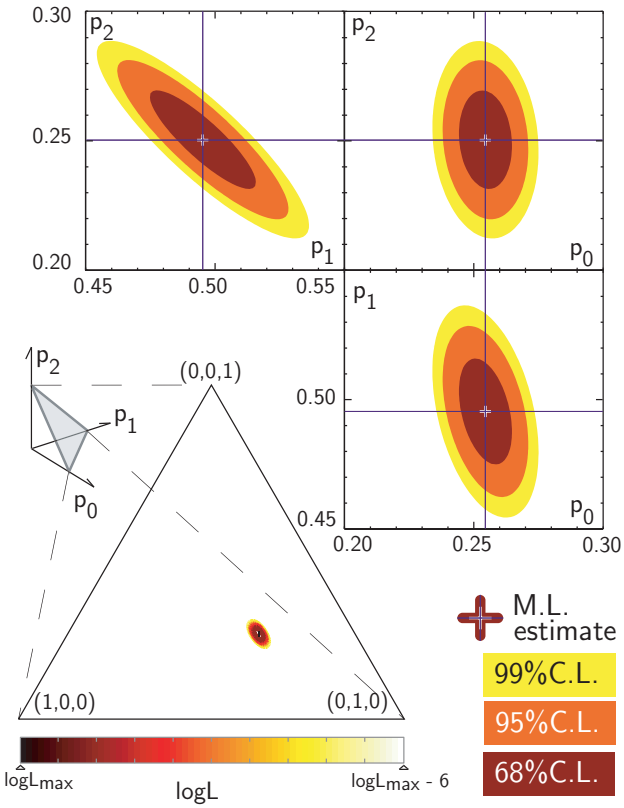

FIG. 1: **Results for Experiment #3 in Table 1.** Shown is the Maximum Likelihood (ML) estimate, $\mathbf{p}_{exp} = [0.254^{+0.010}_{-0.010}, 0.495^{+0.021}_{-0.020}, 0.250^{+0.019}_{-0.019}]$, for the error probabilities of the engineered noise, $A_1 = \{\exp[-i\pi(Z_1 + Z_2)/4]\}$, for which the calculated values are $\mathbf{p} = [1/4, 1/2, 1/4]$. Also shown are the confidence regions for the 68%, 95%, and 99% confidence levels (C.L.), which can be determined from the log of a likelihood function, $\log L$. The experiment was performed on a 2-qubit liquid-state NMR processor, and the noise was implemented by appropriately phase-shifting the pulses. These experiments illustrate the precision with which the protocol can be implemented under conditions of well-developed quantum control.

The other main ingredient of our analysis is the use of statistical bounds to prove that the set of all possible conjugations (which is exponentially large in the number of qubits) need not be performed to estimate the average. Specifically, the set of conjugations needs to be sampled a number of times that grows only logarithmically with the number of qubits. The details of this statistical analysis are provided further below.

General Analysis of the Symmetrisation

More generally, the generic noise affecting a quantum state ρ (a positive matrix of dimension $D \times D$) can be represented by a completely positive map of the form $\Lambda(\rho) = \sum_{k=1}^{D^2} A_k \rho A_k^\dagger$, which is normally subject to a trace-preserving condition $\sum_k A_k^\dagger A_k = 1$. We focus here on systems of n qubits so that $D = 2^n$.

We start by expanding the noise operators in a basis of Pauli operators $P_i \in \mathcal{P}_n$ consists of n-fold tensor product of the usual single-qubit Pauli operators $\{1, X, Y, Z\}$, giving $A_k = \sum_{i=1}^{D^2} \alpha_i^{(k)} P_i/\sqrt{D}$, where $\alpha_i^{(k)} = \mathrm{Tr}[A_k P_i]/\sqrt{D}$, and the Pauli's satisfy the orthogonality relation $\mathrm{Tr}[P_i P_j] = D\delta_{ij}$. The Clifford group $\mathcal{C}_n$ is defined as the normalizer of the Pauli group $\mathcal{P}_n$: it consists of all elements U_i of the unitary group $U(D)$ satisfying $U_i P_j U_i^\dagger \in \mathcal{P}_n$ for every $P_j \in \mathcal{P}_n$. For further details of the Clifford group see [5].

We can analyze the effect of the twirl $\mathcal{C}_1^{\otimes n}$ by noting that any element $C_i \in \mathcal{C}_1^{\otimes n}$ can be expressed as $C_i = P_j Y_l$, where $P_j \in \mathcal{P}_n$ and $Y_l \in \mathcal{Y}_1^{\otimes n}$, and where we consider as equivalent elements of each group that differ only by a phase.

Hence, the $\mathcal{C}_1^{\otimes n}$-twirl of an arbitrary channel Λ consists of the action

$$\Lambda(\rho) \to \overline{\Lambda(\rho)} = \frac{1}{|\mathcal{C}_1^{\otimes n}|} \sum_{j=1}^{|\mathcal{S}_1^{\otimes n}|} \sum_{l=1}^{|\mathcal{P}_n|} \sum_k S_j^\dagger P_l^\dagger A_k P_l S_j \rho S_j^\dagger P_l^\dagger A_k^\dagger P_l S_j. \tag{1}$$

where $|\mathcal{C}_1^{\otimes n}| = |\mathcal{S}_1^{\otimes n}|\,|\mathcal{P}_n|$. The effect of the Pauli-twirl is to create the channel $\sum_i a_i P_i \rho P_i$, where $a_i = \sum_k |\alpha_i^{(k)}|^2/D$ are probabilities, known as a Pauli channel. The effect of the symplectic-twirl on the Pauli channel is to map each of the non-identity Pauli operators to a uniform sum over the 3 non-identity Pauli operators. To express this we separate out terms according to their Pauli weight w, where $w \in \{0, \ldots, n\}$ is the number of non-identity factors in P_l. We let the index $\nu_w \in \{1, \ldots, \binom{n}{w}\}$ count the number of distinct ways that w non-identity Pauli operators can be distributed over the n factor spaces, and the index $\mathbf{i}_w = \{i_1, \ldots, i_w\}$ with $i_j \in \{1, 2, 3\}$ denote which of the non-identity Pauli operators occupies the j'th occupied site. Hence we have,

$$\overline{\Lambda(\rho)} = \frac{1}{|\mathcal{S}_1^{\otimes n}|} \sum_{j=1}^{|\mathcal{S}_1^{\otimes n}|} \sum_{w=0}^{n} \sum_{\nu_w=1}^{\binom{n}{w}} \sum_{\mathbf{i}_w=1}^{3^w} a_{w,\nu_w,\mathbf{i}_w} S_j^\dagger P_{w,\nu_w,\mathbf{i}_w} S_j \rho S_j^\dagger P_{w,\nu_w,\mathbf{i}_w} S_j. \tag{2}$$

For any term with arbitrary but fixed w and ν_w the effect of symplectic-twirl is

$$\frac{1}{|\mathcal{S}_1^{\otimes n}|} \sum_{\mathbf{i}_w=1}^{3^w} a_{w,\nu_w,\mathbf{i}_w} \sum_{j=1}^{|\mathcal{S}_1^{\otimes n}|} S_j^\dagger P_{w,\nu_w,\mathbf{i}_w} S_j \rho S_j^\dagger P_{w,\nu_w,\mathbf{i}_w} S_j = \left(\frac{1}{3^w} \sum_{\mathbf{i}_w}^{3^w} a_{w,\nu_w,\mathbf{i}_w} \right) \sum_{\mathbf{j}_w=1}^{3^w} P_{w,\nu_w,\mathbf{j}_w} \rho P_{w,\nu_w,\mathbf{j}_w}. \tag{3}$$

Consequently we obtain,

$$\overline{\Lambda(\rho)} = \sum_{w=0}^{n} \sum_{\nu_w=1}^{\binom{n}{w}} r_{w,\nu_w} \sum_{\mathbf{i}_w=1}^{3^w} P_{w,\nu_w,\mathbf{i}_w} \rho P_{w,\nu_w,\mathbf{i}_w} \tag{4}$$

where $r_{w,\nu_w} = \frac{1}{3^w} \sum_{\mathbf{i}_w=1}^{3^w} a_{w,\nu_w,\mathbf{i}_w}$.

The effect of actual or virtual permutations of the qubits chosen uniformly at random is to produce the effective channel

$$\overline{\Lambda}^{\Pi}(\rho) = \sum_{w=0}^{n} p_w \sum_{\nu_w=1}^{\binom{n}{w}} \sum_{\mathbf{i}_w=1}^{3^w} \frac{1}{3^w \binom{n}{w}} P_{w,\nu_w,\mathbf{i}_w} \rho P_{w,\nu_w,\mathbf{i}_w}, \tag{5}$$

where

$$p_w = 3^w \sum_{\nu_w=1}^{\binom{n}{w}} r_{w,\nu_w}. \tag{6}$$

This symmetrized channel can now be probed experimentally by inputting the initial state $|0\rangle \equiv |0\rangle^{\otimes n}$ and performing a projective measurement in the computational basis $|l\rangle$, where $l \in \{0,1\}^n$. If we distinguish outcome bit strings only according to their Hamming weight $h \in 0, \ldots, n$, the effect is equivalent to a random permutation of the qubits. Observe that only Pauli X and Y errors will affect the Hamming weight because Pauli Z errors commute with the input state. Hence the probability of measuring an outcome with Hamming weight h is

$$u_h = \sum_{w=0}^{n} R_{hw} p_w$$

where $R_{hw} = \binom{w}{h} 2^h/3^w$ gives the number of Pauli operators of weight w of which exactly h are either X or Y, and where

$$p_w = 3^w \sum_{\nu_w=1}^{\binom{n}{w}} r_{w,\nu_w} = \sum_{\nu_w=1}^{\binom{n}{w}} \sum_{\mathbf{i}_w}^{3^w} p_{w,\nu_w,\mathbf{i}_w} \tag{7}$$

is a quantity of interest, i.e., the total probability of all Pauli errors with weight w. Noting that the $n \times n$ matrix R_{hw} satisfies $R_{hw} = 0$ when $h > w$ and hence is upper triangular, estimates of the p_w can be recovered trivially from the measured probabilities u_h after n back-substitutions.

Furthermore, we can determine more direct information about the noise map if we instead distinguish outcome bit strings only by the parity of a random subset of w qubits. The effect of this is also equivalent to a random permutation of the qubits. Thus, we experimentally implement the $\mathcal{C}_1^{\otimes n}$-twirl $\overline{\Lambda(\rho)}$, and virtually implement the permutation-twirl $\overline{\Lambda}^{\Pi}(\rho)$ by averaging over random choices of subsets of w qubits. The probability q_w that the parity of random subset of w qubits is even is related to $\langle \overline{Z^{\otimes w}} \rangle$, the average of all permutations of Pauli operators with w factors of Z and $n - w$ identity factors, according to

$$c_w \equiv \langle \overline{Z^{\otimes w}} \rangle = q_w - (1 - q_w) = 2q_w - 1, \tag{8}$$

where the c_w correspond to the eigenvalues of the twirled map. In order to clarify the information content of the c_w and their relation to the error probabilities p_w we will make use of the Liouville representation of the twirled channel which is described in the following subsection.

Liouville Representation of the Twirled Channel

Because any two operators $P_{m,\nu_m,\mathbf{i}_m} \in \mathcal{P}_n$ either commute or anti-commute, it follows that

$$\overline{\Lambda}^{\Pi}\left(P_{m,\nu_m,\mathbf{i}_m}\right) = \left(\Pr(\text{comm}) - \Pr(\text{anti-comm})\right) P_{m,\nu_m,\mathbf{i}_m} = c_m P_{m,\nu_m,\mathbf{i}_m}, \tag{9}$$

where Pr(comm) (Pr(anti-comm)) is the probability of the channel $\overline{\Lambda}^{\Pi}$ acting with a noise operators $P_{w,\nu_w,\mathbf{i}_w}$ which commutes (anti-commutes) with $P_{m,\nu_m,\mathbf{i}_m}$. Thus, the Pauli operators $P_{m,\nu_m,\mathbf{i}_m}$ are the eigenoperators of the channel with corresponding eigenvalues c_m. The eigendecomposition of $\overline{\Lambda}^{\Pi}$ is given by

$$\overline{\Lambda}^{\Pi}(\rho) = \sum_{w=0}^{n} c_w M_w^c(\rho), \tag{10}$$

where M_w^c are the superoperators

$$M_w^c(\rho) = \frac{1}{2^n} \sum_{\nu_w=0}^{\binom{n}{w}} \sum_{\mathbf{i}_w=0}^{3^w} P_{w,\nu_w,\mathbf{i}_w} \operatorname{tr}(P_{w,\nu_w,\mathbf{i}_w} \rho). \tag{11}$$

We can also rewrite the usual parameterisation of $\overline{\Lambda}^{\Pi}$ as

$$\overline{\Lambda}^{\Pi}(\rho) = \sum_{w=0}^{n} p_w M_w^p(\rho), \tag{12}$$

where M_w^p are the superoperators

$$M_w^p(\rho) = \frac{1}{3^w \binom{n}{w}} \sum_{\nu_w=0}^{\binom{n}{w}} \sum_{\mathbf{i}_w=0}^{3^w} P_{w,\nu_w,\mathbf{i}_w} \rho P_{w,\nu_w,\mathbf{i}_w}. \tag{13}$$

By considering the Liouville representation of these superoperators it is easy to show that the M_w^c are orthogonal and that the M_w^p are orthogonal. Thus, $\{c_w\}_{w=0}^n$ parameterizes the channel $\overline{\Lambda}^{\Pi}$ uniquely, and $\{p_w\}_{w=0}^n$ also parameterizes the same channel uniquely. Using the Liouville representation it follows that these parameterizations are related by a $(n+1) \times (n+1)$ matrix Ω such that

$$c_w = \sum_{w'=0}^{n} p_{w'} \Omega_{w,w'}, \tag{14}$$

$$p_w = \sum_{w'=0}^{n} c_{w'} \Omega^{-1}_{w,w'} \tag{15}$$

with Ω defined by

$$\Omega_{w,w'} = \frac{4^n}{3^{w+w'}\binom{n}{w}\binom{n}{w'}}\langle M_w^c, M_{w'}^p\rangle \tag{16}$$

$$\Omega^{-1}_{w,w'} = \langle M_w^p, M_{w'}^c\rangle, \tag{17}$$

where $\langle\cdot,\cdot\rangle$ is the Hilbert-Schmidt inner product of superoperators acting on Liouville space defining the notion of orthogonality discussed above. To obtain an explicit expression for $\Omega_{w,w'}$, we start from (9) and observe that a Pauli operator of weight w is scaled by a channel of the form

$$\mathcal{N}_{w'}(\rho) = \frac{1}{3^{w'}\binom{n}{w'}}\sum_{\nu_{w'}=0}^{\binom{n}{w'}}\sum_{\mathbf{i}_{w'}=0}^{3^{w'}} P_{w',\nu_{w'},\mathbf{i}_{w'}}\rho P_{w',\nu_{w'},\mathbf{i}_{w'}}. \tag{18}$$

This implies

$$\Omega_{m,w} = -1 + \sum_{L=\max(0,w+m-n)}^{\min(m,w)} \frac{\binom{n-m}{w-L}\binom{m}{L}}{\binom{n}{w}}\frac{3^L+(-1)^L}{3^L}, \tag{19}$$

and, using (16) and (17), it follows that

$$\Omega^{-1}_{m,w} = \frac{3^{m+w}\binom{n}{m}\binom{n}{w}}{4^n}\Omega_{m,w}. \tag{20}$$

For the case of two-qubit channels, this matrix is given by

$$\Omega = \begin{pmatrix} 1 & 1 & 1 \\ 1 & \frac{1}{3} & -\frac{1}{3} \\ 1 & -\frac{1}{3} & \frac{1}{9} \end{pmatrix} \tag{21}$$

$$\Omega^{-1} = \frac{1}{16}\begin{pmatrix} 1 & 6 & 9 \\ 6 & 12 & -18 \\ 9 & -18 & 9 \end{pmatrix}, \tag{22}$$

and for the case of three-qubit channels, it is given by

$$\Omega = \begin{pmatrix} 1 & 1 & 1 & 1 \\ 1 & \frac{5}{9} & \frac{1}{9} & -\frac{1}{3} \\ 1 & \frac{1}{9} & -\frac{5}{27} & \frac{1}{9} \\ 1 & -\frac{1}{3} & \frac{1}{9} & -\frac{1}{27} \end{pmatrix} \tag{23}$$

$$\Omega^{-1} = \frac{1}{64}\begin{pmatrix} 1 & 9 & 27 & 27 \\ 9 & 45 & 27 & -81 \\ 27 & 27 & -135 & 81 \\ 27 & -81 & 81 & -27 \end{pmatrix} \tag{24}$$

Uncorrelated Noise Locations

A noise channel over n qubits that has a distribution of error locations which is uncorrelated, but otherwise arbitrary, is mapped under twirling and random permutations to a channel which is a tensor product of n single-qubit depolarizing channels. Each of these single-qubit channels has the form

$$\mathcal{D}(\rho) = (1-p)\rho + \frac{p}{3}(X\rho X + Y\rho Y + Z\rho Z) \tag{25}$$

and scales a single-qubit Pauli operator by $c_1 = 1 - \frac{4}{3}p$. Thus, the n qubit channel will scale a Pauli operator with weight w by $c_w = c_1^w$.

This is only a necessary condition for the independence of the distribution of error locations because there are correlated error models which can also give rise to this exponential scaling law. Hence, statistical disagreement with the exponential scaling law implies that the distribution of the error locations is (statistically unlikely) to be uncorrelated, although statistical agreement with the scaling law does not guarantee that the errors are uncorrelated.

Circuit Complexity and Statistical Analysis

The circuit complexity is depth 2 with only $2n$ single-qubit gates required for the protocol. The outcome from any single experiment is just a binary string. The number of such trials required to estimate the probability q_w of even parity for a random subset of w bits to within a given precision δ is clearly independent of the number of qubits because the problem is reduced to the simple task of estimating the probability of a 2-outcome classical statistical test. More precisely from the Chernoff inequality, any estimate of the exact average $\mathbb{E}[X] = q_w$ after K *independent trials* satisfies,

$$\Pr(|\frac{1}{K}\sum_{i=1}^{K} X_i - \mathbb{E}[X]| > \delta) \leq 2\exp(-\delta^2 K). \tag{26}$$

We see that the number of experiments required to estimate q_w to precision δ with constant probability is at most,

$$K = \log(2)\delta^{-2},$$

where each experiment is an *independent trial* consisting of a single shot experiment in which the Clifford gates are chosen uniformly at random. The number of experimental trials required to estimate the complete set of probabilities $\{q_1, \ldots, q_w, \ldots q_n\}$ can be obtained from the union bound,

$$\Pr(\cup_w \mathcal{E}_w) \leq \sum_w \Pr(\mathcal{E}_w) \tag{27}$$

which applies for arbitrary events $\mathcal{E}_w$. In our case each $\mathcal{E}_w$ is associated with the event that $|\frac{1}{K}\sum_{k=1}^{K} X_k - \mathbb{E}[X]| > \delta$ and similarly $\cup_w \mathcal{E}_w$ is the probability that at least one of the n estimated probabilities q_w satisfies this property (i.e., is an unacceptable estimate) after K trials. Whence, the probability that at least one of the n estimated probabilities is outside precision δ of the exact probability is bounded above by,

$$\Pr(\cup_w \mathcal{E}_w) \leq 2n\exp(-\delta^2 K).$$

This implies that at most $K = \mathcal{O}(\delta^{-2}\log(2n))$ experimental trials are required to estimate each of the components of the (probability) vector $(q_1, \ldots, q_n)$ to within precision δ with constant probability.

Similarly, for the ensemble QIP scheme, in which n distinct input states must be prepared, the protocol requires $k = \mathcal{O}(\log(2n)/\delta^2)$ runs for each input state in order to estimate the n output parameters c_w to precision δ with constant probability.

Statistical Uncertainty for the p_w Estimates

Given an estimate of the $c_w = \langle Z^{\otimes w}\rangle$ with some variance σ^2, the variance of the estimate of a particular p_w is given by

$$\sigma_w^2 = \sum_{i=0}^{n}\sum_{j=0}^{n} \Omega_{w,i}^{-1}\Omega_{w,j}^{-1}\mathrm{Cov}(c_i, c_j) \tag{28}$$

Assuming the estimates for all c_w have the same variance, the positivity constraint on the covariance matrix of the c_w estimates requires that $|\mathrm{Cov}(c_i, c_j)| \leq \sigma^2$, yielding the upper bound

$$\sigma_w^2 \leq \sigma^2 \sum_i \sum_j \left|\Omega_{w,i}^{-1}\Omega_{w,j}^{-1}\right|. \tag{29}$$

From (9), it is clear that

$$|\Omega_{w,w'}| \leq 1, \tag{30}$$

so the from (20) we have

$$\sigma_w \leq \sigma 3^w \binom{n}{w}. \tag{31}$$

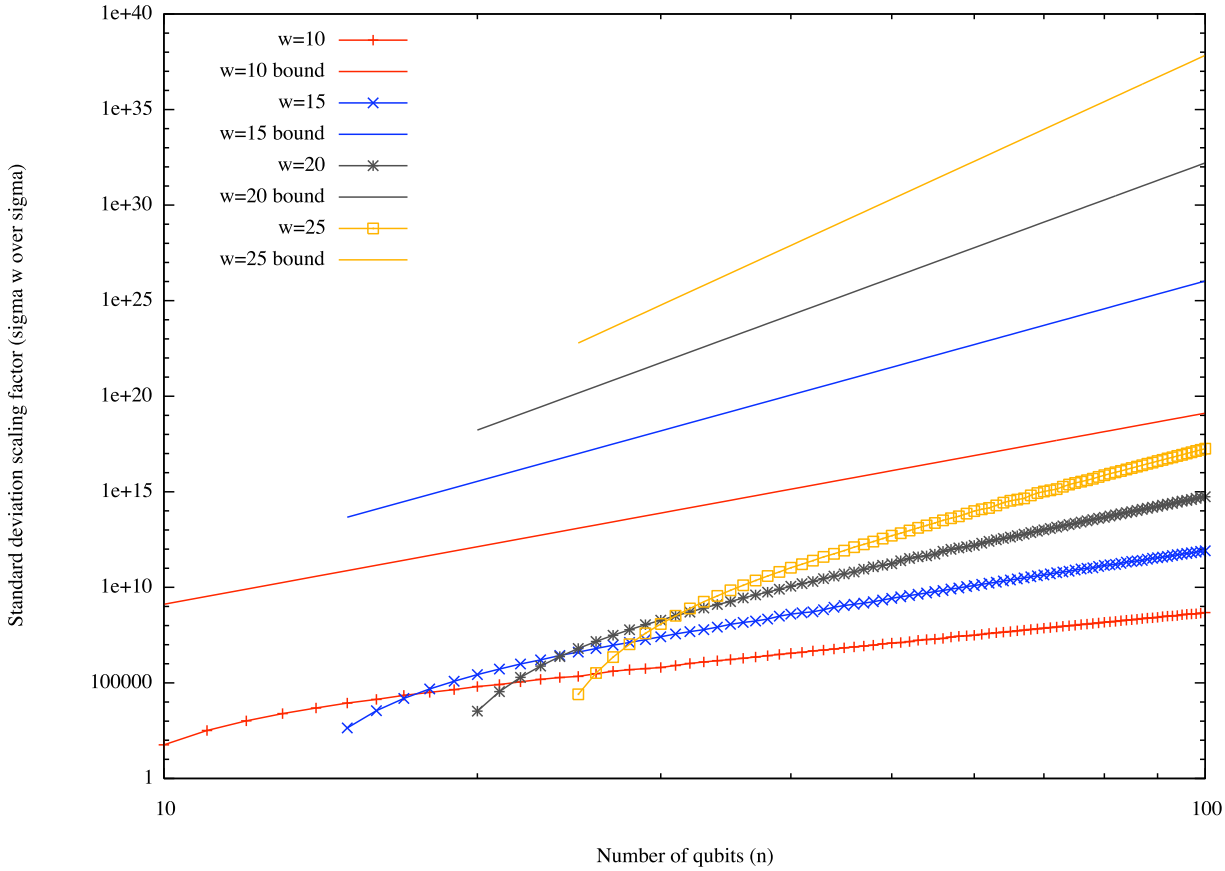

FIG. 2: **Bounds on Standard Deviation for Statistical Estimates of p_w.** Analytic upper bound on standard deviation scaling factor, and numerical calculations for scaling factor with worst case correlations.

Using the fact that

$$\binom{n}{w} \leq \frac{n^w \mathrm{e}^w}{w^w}, \tag{32}$$

we can rigorously show that the uncertainty σ_w on the estimate of p_w is bounded by

$$\sigma_w \leq \sigma \left(\frac{3}{w}\right)^w n^w \mathrm{e}^w. \tag{33}$$

Exact numerical computation of the uncertainty scaling factor $\frac{\sigma_w}{\sigma}$, depicted in Fig. S2, indicates that for fixed w the uncertainty grows as a polynomial in n, but the degree of that polynomial depends linearly on w. For large n, we find that

$$\frac{\sigma_w}{\sigma} \approx \mathrm{e}^{kw+a} n^{mw+b}, \tag{34}$$

where $k = -1.6 \pm 0.1$, $a = 11.8 \pm 1.8$, $m = 0.639 \pm 0.009$, and $b = -0.98 \pm 0.16$.

These numerical results support our analytic bound indicating that applying the c_w estimates to estimate the multi-body noise probabilities p'_w to within a fixed precision, for $0 \leq w' \leq b < n$ with b a constant, requires $O(n^b)$ experiments.

Generalization: the Pauli-twirl

We expect that the $\mathcal{C}_1^{\otimes n}$-twirl is a first step in a hierarchy of tests available under the general symmetrization approach, with each test giving more fine-grained information. One obvious example of a more fine-grained test is a variation of the protocol in which only a Pauli-twirl is applied enables a estimation of the $\mathcal{O}(n^3)$ relative probabilities of Pauli X, Y and Z errors. The full scope of information that can be estimated efficiently via the symmetrisation approach is an important topic for further research.

Solid-state NMR Experimental Results

The results of the solid-state experiments are calculated after factoring out the effect of decoherence occurring during the twirling operations, as described in the main text, in order to isolate the noise associated with the time-suspension sequence. It should be noted that this was a small effect: the twirling operations accounted for only $\simeq 1\%$ fidelity loss per gate.

As noted in the main text, shorter pulse-spacing should lead to improved performance unless there is a competing process at the faster time-scale. Although we see improved performance in the averaging of the homonuclear dipolar Hamiltonian (as evident from experiments #5 and #6 in Table 1), the performance falls short of that expected from numerical simulations of the homonuclear 3-qubit system. In particular, the 5μs pulse-sequence is still limited by decoherence from incomplete (heteronuclear) decoupling of the qubits (carbon nuclei) from the environment (nearby hydrogen nuclei). At the 5μs pulse-spacing the carbon nuclei are being modulated on a time-scale close to the proton decoupling frequency, suggesting that the decoupling sequence may no longer be averaging the heteronuclear coupling to zero. The simple modification of the twirling protocol (in which the permutations are not performed on the weight $w = 1$ input states) allows for determining which qubit accrues the greatest single-qubit errors. The results were consistent with identifying the primary source of single-qubit errors as the qubit whose (heteronuclear) coupling to the hydrogen is an order of magnitude larger than that of the other two qubits.

We have applied the test for the presence of correlations to the experimental results for the c_w from experiments #5 and #6 in Table 1. The results are shown in Fig. S3. For both experiments the results are statistically consistent with the uncorrelated scaling law, though, as already noted, this does not imply that the un-twirled noise consists of uncorrelated errors.

Supporting References and Notes

[1] E. Knill *et al.*, *Nature* **404**, 368 (2000).
[2] J. Baugh *et al.*, *Phys. Rev. A* **73**, 022305 (2006).
[3] B.M. Fung, A.K. Khitrin, K. Ermolaev, *Journal of Magnetic Resonance* **142**, 97 (2000).
[4] N. Khaneja, T. Reiss, C. Kehlet, T.S. Herbruggen, S.J. Glaser, *Journal of Magnetic Resonance* **172**, 296 (2005).
[5] D. Gottesman, Ph.D. Thesis, quant-ph/9705052 (1997).

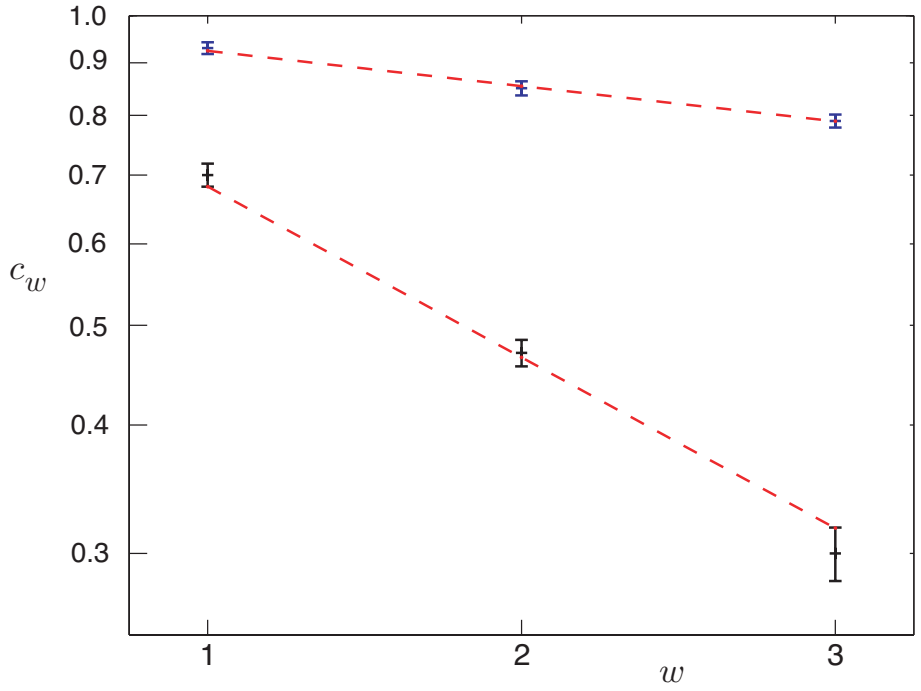

FIG. 3: **Test for Correlations in the Solid-state Experiments.** Experimental values for the c_w for the 5μs (blue) and 10μs (black) pulse-sequences, plotted against the uncorrelated scaling law obtained by a least-squares fit (dashed red) with c_1 as free parameter. Error-bars correspond to statistical (standard deviation) and experimental errors added in quadrature. The goodness-of-fit for the 5μs and 10μs pulse-spacing sequences is $\chi^2 = 0.32$ and $\chi^2 = 1.98$, respectively, for $n_d = 2$.

E.3 Approximating the Jones Polynomial

In this work, we experimentally implement a DQC1 algorithm to evaluate a *knot invariant* known as the Jones polynomial. This problem is complete for the complexity class DQC1 and is the first experimental implementation of such a problem. Implemented on the four carbon nuclei in crotonic acid the experiment distinguished between all knots whose braid representations have three strands and four crossings. The experiment showed that with current control available in liquid state NMR, we were able to correctly distinguish topologically distinct knots 91% of the time.

G. Passante and I modified the original algorithm by Shor and Jordan to be suitable for implementation in NMR. This required a modification of the encoding of the braid representation. The algorithm calls for an estimation of a weighted trace of the implemented unitary. To accomplish that, we introduced an extra ancilla, and rotated its state such that the measurement readily revealed the weighted trace.

Experimental Approximation of the Jones Polynomial with One Quantum Bit

G. Passante,[1] O. Moussa,[1] C. A. Ryan,[1] and R. Laflamme[1,2]

[1]*Institute for Quantum Computing and Department of Physics, University of Waterloo, Waterloo, Ontario, N2L 3G1, Canada*
[2]*Perimeter Institute for Theoretical Physics, Waterloo, Ontario, N2J 2W9, Canada*

(Received 17 September 2009; published 18 December 2009)

We present experimental results approximating the Jones polynomial using 4 qubits in a liquid state nuclear magnetic resonance quantum information processor. This is the first experimental implementation of a complete problem for the deterministic quantum computation with one quantum bit model of quantum computation, which uses a single qubit accompanied by a register of completely random states. The Jones polynomial is a knot invariant that is important not only to knot theory, but also to statistical mechanics and quantum field theory. The implemented algorithm is a modification of the algorithm developed by Shor and Jordan suitable for implementation in NMR. These experimental results show that for the restricted case of knots whose braid representations have four strands and exactly three crossings, identifying distinct knots is possible 91% of the time.

DOI: 10.1103/PhysRevLett.103.250501 PACS numbers: 03.67.Lx, 03.67.Ac, 76.60.−k

Quantum information processors have the potential to solve some problems exponentially faster than current classical methods [1]. While much effort has been concentrated on the most conventional circuit model of computation which involves preparation of pure fiducial quantum states, other models of computation, where only one pure quantum bit is required, still offer efficient solutions to classically intractable problems. Deterministic quantum computation with one quantum bit (DQC1) is such a model [2]. It extracts the power of 1 bit of quantum information alongside a register of many qubits in a completely random state. Study of DQC1 was originally motivated by liquid state nuclear magnetic resonance (NMR), which is a high temperature ensemble model of quantum computation. Although this model of computation is weaker than conventional models with many pure qubits, it has been shown to have several important applications where classical methods are inefficient: simulating quantum systems [2], estimating the average fidelity decay under quantum maps [3], and quadratically signed weight enumerators [4]. Additionally, the approximation of the Jones polynomial at the fifth root of unity has recently been shown to completely encapsulate the power of DQC1 [5]. DQC1 algorithms have been experimentally implemented in optics [6] and liquid and solid state NMR [7–9]—none of which has been shown to be DQC1 complete. In [8], the authors implement a DQC1 algorithm on two qubits to evaluate the Jones polynomial at various points for specific knots. This Letter describes the implementation of an instance of a DQC1-complete algorithm [5], which scales for any size knot.

Unlike its name suggests, DQC1 does not require a completely pure qubit to provide an advantage over known classical methods, but rather a small fraction of a pure qubit. This pseudopure state is almost completely mixed with a small bias towards the ground state, and is used as the control qubit in the DQC1 algorithm. A unitary is performed on the qubits in the completely mixed state and is controlled by the pseudopure qubit (Fig. 1).

Measurements of $\langle\sigma_x\rangle$ and $\langle\sigma_y\rangle$ yield the real and imaginary parts of the trace of the unitary, normalized by the amount of polarization on the pure qubit.

Applications for the Jones polynomial are extensive in physics; for example, the fields of statistical mechanics, quantum field theory, and quantum gravity would benefit from an efficient method for approximating this polynomial [10]. Knot invariants help to solve a fundamental problem in knot theory: determining if two knots, defined as the embedding of the circle in $\mathbb{R}^3$, are topologically different, up to ambient isotopy. Two knots can only be confirmed identical if one can be maneuvered into the other by a sequence of Reidemeister moves, which keep the topological properties of knots intact. This process is very tedious as often the sequence of Reidemeister moves requires an increase in the number of crossings in the knot. Even the simplest such problem of identifying the unknot, a circle with no crossings, has been shown to be contained in the complexity class NP [11]. Knot invariants, such as the Jones polynomial, have the same value for different representations of the same knot. In other words, if a knot invariant evaluates to different values for two knots, they are guaranteed to be distinct. This makes them a welcome alternative to sequences of Reidemeister moves.

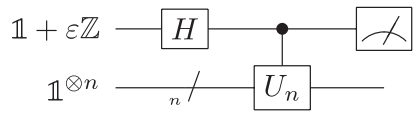

FIG. 1. The DQC1 circuit where the pure qubit has a bias of ε towards the ground state. Measurements of $\langle\sigma_x\rangle$ and $\langle\sigma_y\rangle$ will yield the real and imaginary parts of $\varepsilon\mathrm{Tr}(U_n)/2^n$, respectively.

Unfortunately, exact evaluation of the Jones polynomial at all but a few points is hard for the complexity class #P [12]. Several efforts for finding quantum algorithms for the Jones polynomial have been attempted and approximations at several special points have been shown to be complete for the complexity class BQP [13,14]. Largely building on this work it was then shown that approximations of the Jones polynomial for trace or plat closures at principal roots of unity can be computed on a quantum computer in polynomial time [15]. Later it was shown that for the plat closure the problem is BQP complete [16,17]. The algorithm developed by Shor and Jordan shows that approximating the Jones polynomial at the fifth root of unity for any knot is a complete problem for DQC1.

For the purposes of this algorithm, knots are described in the discrete language of braid groups. Every knot can be written as a braid, which is a series of strands crossings over and under each other with loose ends at both the top and bottom. Braids can then be converted into a knot by the trace closure which connects the top and bottom ends of the braid in sequential order. The braid group for m strands B_m is generated by $s_1 \ldots s_{m-1}$ that denote elementary crossings where s_i indicates the ith strand crossing over the $(i+1)$th strand and s_i^{-1} indicates strand $(i+1)$ crossing over strand i. These elementary crossings satisfy the relations: $s_i s_j = s_j s_i$ for $|j-i| > 1$ and $s_{i+1} s_i s_{i+1} = s_i s_{i+1} s_i$.

The implemented algorithm utilizes the Fibonacci representation of the braid group B_n, which is described in the context of the Temperley-Lieb recoupling theory [18]. In this theory there are two particles p and $*$, which exhibit the following properties: p interacts with another p to create a p or a $*$ particle, $*$ interacts with a p to always create a p particle, and two $*$'s never interact. Strings of these particles create a basis in a complex vector space. More details of this representation can be found in [18], but for our purposes it suffices to state that for a braid with m strands the basis vectors contain $m+1$ elements of p's and $*$'s with the restriction that no two $*$ particles be beside one another. These basis vectors are then transformed into the computational basis and unitary matrices σ_i, which represent each elementary crossing in the braid group, are constructed. For the particular form of these unitaries, please refer to [5].

The algorithm developed by Shor and Jordan approximates the Jones polynomial at the single point $t = e^{2i\pi/5}$ by finding the weighted trace of a unitary that describes the braid representation of the knot. The algorithm is modified for this implementation and the varied portions are described below. The primary difference is in the encoding of the basis states. The Fibonacci basis vectors consist of four distinct subspaces, only two of which are relevant for the algorithm: the f_m vectors of the form $*\ldots p$ and f_{m-1} of the form $*\ldots *$, where $f_n = [1, 1, 2, 3, \ldots]$ is the Fibonacci sequence. These are the only two subspaces that are encoded in this implementation. The Zeckendorf representation, $z' = 2^{n-1}s_1 + \sum_{i=2}^{m-1} s_{i+s_1} f_i$ converts the Fibonacci basis vectors into integers that are then converted to a nonsaturated computational basis. The second notable difference is the method used to calculate the weighted trace, defined as

$$\begin{aligned} \mathrm{WTr} &= 1 \times (\text{trace of subspace} * \ldots *) + \phi \\ &\quad \times (\text{trace of subspace} * \ldots p), \end{aligned} \tag{1}$$

where $\phi = (1+\sqrt{5})/2$ is the golden ratio. Implementing these weights for our encoding is achieved by purifying the second qubit, then applying a rotation taking $|0\rangle$ to $(\sqrt{\phi}|0\rangle + |1\rangle)/\sqrt{1+\phi}$, which ensures that each subspace receives the desired weight. The computational model now contains two initialized qubits; however, this modification does not change the computational power as DQC(k) is known to have the same computational power as DQC1 for k that can grow logarithmically with the total number of qubits [5]. The extra basis states are accounted for in the final calculation of the Jones polynomial. The circuit for our evaluation of the Jones polynomial for braids with four strands can be seen in Fig. 2. It is worthwhile to note that the off-diagonal elements in the rotated pure qubit do not contribute to the algorithm as the unitary matrices U_n are always block diagonal, thereby eliminating the off-diagonal elements in the calculation of the trace. The state of the top qubit at the completion of the algorithm is

$$\rho = \frac{1}{2^{n-1}(1+\phi)} \begin{pmatrix} 1 & \mathrm{WTr}(U_n^\dagger) \\ \mathrm{WTr}(U_n) & 1 \end{pmatrix},$$

which upon measurement of $\langle\sigma_x\rangle$ and $\langle\sigma_y\rangle$ yields the real and imaginary parts of $\mathcal{M} = \mathrm{WTr}(U_n)/[2^{n-1}(1+\phi)]$ respectively, where n is the number of qubits in the bottom register. The measured quantity $\mathcal{M}$ is then used to calculate the approximation of the Jones polynomial $V(t)$, corresponding to the trace closure of the given braid at $t = e^{i2\pi/5}$,

$$V(e^{i2\pi/5}) = [-(e^{i2\pi/5})^4]^{3w} \phi^{-1} [2^{n-1}(1+\phi)\mathcal{M} - \kappa],$$

where $\kappa = (2^{n-1} - f_m)\phi + (2^{n-1} - f_{m-1})$ and w is the writhe of the braid, defined as the number of positive crossings minus the number of negative crossings.

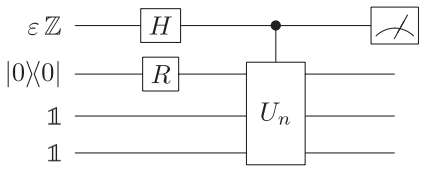

FIG. 2. Circuit diagram for the approximation of the Jones polynomial for the knots whose braid representations consist of four strands. The initial state given is the traceless deviation matrix. The single qubit gates are the Hadamard and the rotation for implementing the weights of the trace. The measurements performed on the top qubit are expectation values of the Pauli x and y operators.

Liquid state NMR offers one of the most advanced implementations of quantum information processors with high fidelity control of multiple qubits [19]. The qubits are a bulk ensemble of identical spin-1/2 nuclei that exhibit a two-level energy structure in the presence of a strong magnetic field. The ensemble of approximately 10^{20} molecules is manipulated in parallel and an ensemble measurement is performed using quadrature detection of the free induction decay to give $\langle\sigma_x\rangle$ and $\langle\sigma_y\rangle$. The algorithm described above was demonstrated in liquid state NMR for the set of knots whose braid representations have four strands and three crossings. There are six distinct knots in this set and hence, six distinct Jones polynomials. The goal of the experiment is to distinguish between two distinct knots given their braid representations. The subspaces of interest have $f_4 = 3$ and $f_{4-1} = 2$ basis states, respectively; thus, the encoding of the basis states requires 3 qubits in the bottom register and a fourth as the control qubit.

The experiment was implemented on a Bruker Avance 700 MHz spectrometer using the molecule transcrotonic acid (shown in Fig. 3). The four qubits are experimentally realized by the four carbon nuclei, synthesized to be carbon-13, while the hydrogen are decoupled using the WALTZ-16 [20] composite pulse sequence. C_1 is our readout qubit whose initial state is the thermal state of $\rho = \mathbb{1} + \varepsilon\mathbb{Z}$, C_2 is purified to the pseudopure state $|0\rangle\langle 0|$, and the remaining C_3 and C_4 are initialized to the completely mixed state. The radio frequency (rf) pulses that implement the unitary transformations are numerically generated using the GRAPE algorithm [21,22] which starts from a random guess and is then iteratively improved through a gradient ascent search. The GRAPE pulses are optimized to produce a fidelity $|\mathrm{tr}(U_{\mathrm{goal}}^{\dagger}U_{\mathrm{sim}})|^2/d^2$, where d is the dimension of the Hilbert space of U_{goal}, of no less than 0.998 and are designed to be robust to small inhomogeneities ($\pm 3\%$) in the rf control field. Each controlled-σ_i unitary transformation is designed as a single pulse of 60 ms. The pulses are corrected for nonlinearities in the pulse generation and transmission to the sample by measuring the rf signal at the position of the sample using a feedback loop and iteratively modifying the pulse accordingly. Through the feedback loop the implemented pulse can be measured and was found to have a simulated fidelity of 0.99 after correction.

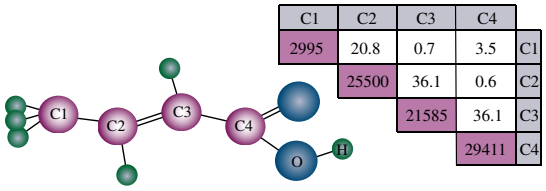

	C1	C2	C3	C4	
C1	2995	20.8	0.7	3.5	C1
C2		25500	36.1	0.6	C2
C3			21585	36.1	C3
C4				29411	C4

FIG. 3 (color online). The molecule transcrotonic acid and a table with the parameters of the Hamiltonian given in Hz. The shaded diagonal elements represent the chemical shifts ω_i with the Hamiltonian $\Sigma_i \pi\omega_i\sigma_z^i$. The remaining elements indicate the scalar coupling constants J_{ij} with the Hamiltonian $\Sigma_{i<j}\pi J_{ij}\sigma_z^i\sigma_z^j$.

The resulting spectrum is fit and compared to a reference spectrum, traditionally of the initial state, to give the expectation value results. In this experiment, pulses whose propagator was designed to be the identity were generated using GRAPE to have the same length and the same average power and fidelity as the controlled σ_i. These pulses were implemented and used to create a reference spectrum in an attempt to normalize some decoherence effects. The state measured after three successive identity pulses, totaling 180 ms had only 60% of the original signal (see Fig. 4), indicating this as a crucial step in the experimental procedure.

The algorithm was implemented for 18 different braids, which correspond to 6 distinct Jones polynomials. The results are displayed in Fig. 5. Systematic errors from imperfect initial state preparation and decoherence not captured by the reference state result in the offsets from the theoretical values. The main contribution to the spreading of the experimental points is the finite fidelity of the optimal control pulses.

Two values of the Jones polynomial at best can distinguish between two knots if they are sufficiently far apart, and at worst, give no information, as even evaluations of the Jones polynomial that are identical would not be suffi-

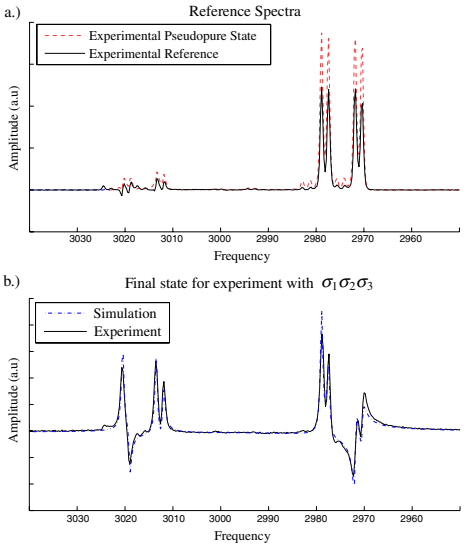

FIG. 4 (color online). The dashed (red) spectrum represents the pseudopure state immediately after creation in the top (a) graph. The solid (black) spectrum is the same pseudopure state after 180 ms of pulses designed to perform the identity. In the bottom graph (b), the solid spectrum (black) indicates the final state of the experiment and it is compared to simulation [dashed (blue)]. This particular experiment is for the knot whose braid representation has crossings $s_1 s_2 s_3$.

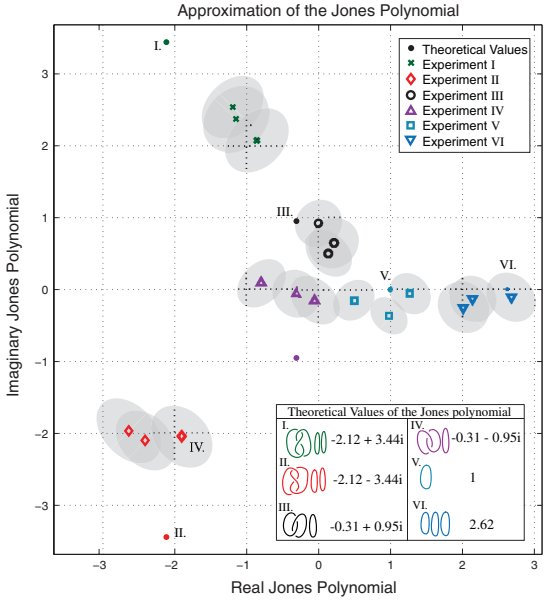

FIG. 5 (color). The results for the approximation of the Jones polynomial for knots whose braid representations have 4 strands and 3 crossings. There are six unique knots of this kind and their theoretical values of the Jones polynomial are plotted for the six experiments. The corresponding experimental data points of three braid representations for each experiment are plotted along with error ellipses demonstrating the statistical error (with 86.5% confidence levels or 2σ). The distribution is generated by simulating each experiment 200 times with single pulse fidelities of 0.99 which is the implemented pulse fidelity. Using the error ellipses as discriminators, these results yields a 91% success rate for distinguishing distinct knots.

cient information to conclude the two knots are identical. This leads to two types of errors when interpreting the data: *passive* and *fatal* errors. Passive errors occur when two distinct knots are impossible to distinguish because of their relatively close distance to one another, while fatal errors occur when two identical knots are determined to be distinct. The success rate for determining whether knots are distinct is calculated as the average of the percent of distinct knots correctly identified and the percent of identical knots correctly indistinguishable. The error ellipses give a direct method for determining if two knots are distinct. If the error ellipses for a pair of knots do not overlap then it is inferred that the knots are distinct, whereas if the two ellipses overlap no information is gained. For the confidence region plotted in Fig. 5, 134 of the possible 135 pairs of distinct knots are correctly distinguished with 3 fatal errors of a possible 18, corresponding to a success rate of 91%.

Approximation of the Jones polynomial is an example of a classical problem that appears intractable, but that can be solved using a one clean qubit quantum computer. This is the first experimental implementation of a DQC1-complete problem, and is performed in liquid state NMR with four qubits, resulting in a 91% success rate for braids with four strands and a total of three crossings. In future work it will be interesting to see how the values of the Jones polynomial spread as you scale to larger knots and what size knot can be experimentally implemented before noise and control errors destroy the quantum advantage.

G. P. would like to thank M. Ditty for his technical expertise with the spectrometer. This work was funded by NSERC, QuantumWorks, and CIFAR.

[1] M. Nielsen and I. Chuang, *Quantum Computation and Quantum Information* (Cambridge University Press, Cambridge, U.K., 2000).
[2] E. Knill and R. Laflamme, Phys. Rev. Lett. **81**, 5672 (1998).
[3] D. Poulin, R. Blume-Kohout, R. Laflamme, and H. Ollivier, Phys. Rev. Lett. **92**, 177906 (2004).
[4] E. Knill and R. Laflamme, Inf. Proc. Lett. **79**, 173 (2001).
[5] P. W. Shor and S. P. Jordan, Quantum Inf. Comput. **8**, 681 (2008).
[6] B. P. Lanyon, M. Barbieri, M. P. Almeida, and A. G. White, Phys. Rev. Lett. **101**, 200501 (2008).
[7] C. A. Ryan, J. Emerson, D. Poulin, C. Negrevergne, and R. Laflamme, Phys. Rev. Lett. **95**, 250502 (2005).
[8] R. Marx, A. Fahmy, L. Kauffman, S. Lomonaco, A. Spörl, N. Pomplun, T. Schulte-Herbrüggen, J. Myers, and S. Glaser, arXiv:0909.1080.
[9] O. Moussa, C. A. Ryan, D. G. Cory, and R. Laflamme (to be published).
[10] L. Kauffman, *Knots and Physics* (World Scientific, Singapore, 1991).
[11] J. Hass, J. Lagarias, and N. Pippenger, J. AMC **46**, 185 (1999).
[12] F. Jaeger, D. L. Vertigan, and D. J. A. Welsh, Math. Proc. Cambridge Philos. Soc. **108**, 35 (1990).
[13] M. H. Freedman, A. Kitaev, and Z. Wang, Commun. Math. Phys. **227**, 587 (2002).
[14] M. H. Freedman, M. Larsen, and Z. Wang, Commun. Math. Phys. **227**, 605 (2002).
[15] D. Aharonov, V. Jones, and Z. Landau, arXiv:0511096.
[16] D. Aharonov and I. Arad, arXiv:0605181.
[17] P. Wocjan and J. Yard, arXiv:0603069.
[18] L. Kauffman and S. Lomonaco, Jr., arXiv:0606114.
[19] L. M. K. Vandersypen and I. L. Chuang, Rev. Mod. Phys. **76**, 1037 (2005).
[20] A. J. Shaka, J. Keeler, and R. Freedman, J. Magn. Reson. **53**, 313 (1983).
[21] N. Khaneja, T. Reiss, C. Kehlet, T. Schulte-Herbruggen, and S. Glaser, J. Magn. Reson. **172**, 296 (2005).
[22] C. A. Ryan, C. Negrevergne, M. Laforest, E. Knill, and R. Laflamme, Phys. Rev. A **78**, 012328 (2008).

References

[Aha03] D. Aharonov. A simple proof that toffoli and hadamard are quantum universal. *Arxiv preprint quant-ph/0301040*, 2003. 22

[ARBC09] E. Amselem, M. Rådmark, M. Bourennane, and A. Cabello. State-independent quantum contextuality with single photons. *Physical Review Letters*, 103(16):160405, 2009. 36

[BBCP09] Piotr Badziag, Ingemar Bengtsson, Adán Cabello, and Itamar Pitowsky. Universality of state-independent violation of correlation inequalities for noncontextual theories. *Phys. Rev. Lett.*, 103(5):050401, Jul 2009. 36

[BCC+07] J. Baugh, J. Chamilliard, C. M. Chandrashekar, M. Ditty, A. Hubbard, R. Laflamme, M. Laforest, D. Maslov, O. Moussa, C. Negrevergne, M. Silva, S. Simmons, C. A. Ryan, D. G. Cory, J. S. Hodges, and C. Ramanathan. Quantum information processing using nuclear and electron magnetic resonance: review and prospects. *Physics in Canada - Quantum Information and Quantum Computing Edition*, 63(4), 2007. 2

[BDSW96] C.H. Bennett, D.P. DiVincenzo, J.A. Smolin, and W.K. Wootters. Mixed-state entanglement and quantum error correction. *Physical Review A*, 54(5):3824–3851, 1996. 22

[Bel66] J.S. Bell. On the problem of hidden variables in quantum mechanics. *Reviews of Modern Physics*, 38(3):447–452, 1966. 36

[BKS+09] H. Bartosik, J. Klepp, C. Schmitzer, S. Sponar, A. Cabello, H. Rauch, and Y. Hasegawa. Experimental test of quantum contextuality in neutron interferometry. *Phys. Rev. Lett.*, 103(4):040403, Jul 2009. 36

[BMR+05] J. Baugh, O. Moussa, C. A. Ryan, A. Nayak, and R. Laflamme. Experimental implementation of heat-bath algorithmic cooling using solid-state nuclear magnetic resonance. *Nature*, 438:470–473, November 2005. 14

[BMR+06] Jonathan Baugh, Osama Moussa, Colm A. Ryan, Raymond Laflamme, Chandrasekhar Ramanathan, Timothy F. Havel, and David G. Cory. Solid-state NMR three-qubit homonuclear system for quantum-information processing: Control and characterization. *Physical Review A (Atomic, Molecular, and Optical Physics)*, 73(2):022305–10, February 2006. 12, 14, 45, 47

[BOS+02] M.D. Bowdrey, D.K.L. Oi, A.J. Short, K. Banaszek, and J.A. Jones. Fidelity of single qubit maps. *Physics Letters A*, 294(5-6):258–260, 2002. 69

[Bra96] S.L. Braunstein. Quantum error correction of dephasing in 3 qubits. *Arxiv preprint quant-ph/9603024*, 1996. 23, 24

[BVFC05] N. Boulant, L. Viola, E. M. Forunato, and D. G. Cory. Experimental implementation of a concatenated quantum error-correcting code. *Physical Review Letters*, 94:130501, 2005. 2

[Cab02] Adán Cabello. Finite-precision measurement does not nullify the kochen-specker theorem. *Phys. Rev. A*, 65(5):052101, Apr 2002. 36

[Cab08] A. Cabello. Experimentally testable state-independent quantum contextuality. *Physical review letters*, 101(21):210401, 2008. 36, 37

[CFH97] D. G. Cory, A. F. Fahmy, and T. F. Havel. Ensemble quantum computing by NMR spectroscopy. *Proceedings of the National Academy of Sciences*, 94(5):1634–1639, MAR 4 1997. 2

[CLK+00] D.G. Cory, R. Laflamme, E. Knill, L. Viola, T.F. Havel, N. Boulant, G. Boutis, E. Fortunato, S. Lloyd, R. Martinez, C. Negrevergne, M. Pravia, Y. Sharf, G. Teklemariam, Y.S. Weinstein, and W.H. Zurek. NMR based quantum information processing: Achievements and prospects. *Fortschritte der Physik*, 48(9-11):875–907, 2000. 2, 4

[CLS+04] J. Chiaverini, D. Leibfried, T. Schaetz, MD Barrett, RB Blakestad, J. Britton, WM Itano, JD Jost, E. Knill, C. Langer, et al. Realization of quantum error correction. *Nature*, 432(7017):602–605, 2004. 22

[CPH98] D. G. Cory, M. D. Price, and T. F. Havel. Nuclear magnetic resonance spectroscopy: An experimentally accessible paradigm for quantum computing. *Physica D*, 120(1-2):82–101, SEP 1 1998. 2

[CPM+98] DG Cory, MD Price, W. Maas, E. Knill, R. Laflamme, WH Zurek, TF Havel, and SS Somaroo. Experimental quantum error correction. *Physical Review Letters*, 81(10):2152–2155, 1998. 2, 22

[CS96] A. R. Calderbank and P. W. Shor. Good quantum error-correcting codes exist. *Phys. Rev. A; Physical Review A"*, 54(2):1098–1105, 1996. 21

[CVZ+98] I. L. Chuang, L. M. K. Vandersypen, X. Zhou, D. W. Leung, and S. Lloyd. Experimental realization of a quantum algorithm. *Nature*, 393:143–146, 1998. 2

[CYC06] Zhiying Chen, Jeffrey Yepez, and David G. Cory. Simulation of the Burgers equation by NMR quantum-information processing. *Physical Review A*, 74(4), OCT 2006. 2

[DiV00] D.P. DiVincenzo. The physical implementation of quantum computation. *Fortschritte der Physik*, 48(9-11):771–783, 2000. 1, 21

[DNBT02] J.L. Dodd, M.A. Nielsen, M.J. Bremner, and R.T. Thew. Universal quantum computation and simulation using any entangling hamiltonian and local unitaries. *Physical Review A*, 65(4):40301, 2002. 12

[DS96] D.P. DiVincenzo and P.W. Shor. Fault-tolerant error correction with efficient quantum codes. *Physical review letters*, 77(15):3260–3263, 1996. 22, 39

[EAŻ05] J. Emerson, R. Alicki, and K. Życzkowski. Scalable noise estimation with random unitary operators. *Journal of Optics B: Quantum and Semiclassical Optics*, 7:S347–S352, 2005. 68

[Fey82] R. P. Feynman. Simulating physics with computers. *International Journal of Theoretical Physics*, 21:467, 1982. 1

[FKE00] BM Fung, AK Khitrin, and K. Ermolaev. An improved broadband decoupling sequence for liquid crystals and solids. *Journal of Magnetic Resonance*, 142(1):97–101, 2000. 11, 30

[FPB+02] E.M. Fortunato, M.A. Pravia, N. Boulant, G. Teklemariam, T.F. Havel, and D.G. Cory. Design of strongly modulating pulses to implement precise effective hamiltonians for quantum information processing. *The Journal of Chemical Physics*, 116:7599, 2002. 13

[FVH+02] E.M. Fortunato, L. Viola, J. Hodges, G. Teklemariam, and D.G. Cory. Implementation of universal control on a decoherence-free qubit. *New Journal of Physics*, 4:5, 2002. 69

[FXBJ07] J. Fitzsimons, L. Xiao, S.C. Benjamin, and J.A. Jones. Quantum information processing with delocalized qubits under global control. *Physical review letters*, 99(3):30501, 2007. 50

[GC97] N. Gershenfeld and I. L. Chuang. Bulk spin-resonance quantum computation. *Science*, 275(5298):350–356, 1997. 2

[Got97] D. Gottesman. *Stabilizer codes and quantum error correction*. PhD thesis, California Institute of Technology, 1997. 21, 22, 23

[HHH99] M. Horodecki, P. Horodecki, and R. Horodecki. General teleportation channel, singlet fraction, and quasidistillation. *Physical Review A*, 60(3):1888–1898, 1999. 69

[HLZ+03] Y.F. Huang, C.F. Li, Y.S. Zhang, J.W. Pan, and G.C. Guo. Experimental test of the kochen-specker theorem with single photons. *Physical review letters*, 90(25):250401, 2003. 36

[JM98] J. A. Jones and M. Mosca. Implementation of a quantum algorithm to solve Deutsch's problem on a Nuclear Magnetic Resonance quantum computer. *Journal of Chemical Physics*, 109:1648–1653, 1998. 2

[Joz94] R. Jozsa. Fidelity for mixed quantum states. *Journal of Modern Optics*, 41(12):2315–2323, 1994. 67

[JRS94] NR Jagannathan, SS Rajan, and E. Subramanian. Refinement of the crystal structure of malonic acid, c3h4o4. *Journal of chemical crystallography*, 24(1):75–78, 1994. 10

[KL97] E. Knill and R. Laflamme. Theory of quantum error-correcting codes. *Physical Review A*, 55(2):900–911, 1997. 22

[KL98] E. Knill and R. Laflamme. Power of one bit of quantum information. *Physical Review Letters*, 81(25):5672–5675, 1998. 41

[KLMN01] E. Knill, R. Laflamme, R. Martinez, and C. Negrevergne. Benchmarking quantum computers: The five-qubit error correcting code. *Physical Review Letters*, 86(25):5811–5814, 2001. 2, 22

[KLP05] D. Kribs, R. Laflamme, and D. Poulin. Unified and generalized approach to quantum error correction. *Physical review letters*, 94(18):180501, 2005. 21

[KRK+05] N. Khaneja, T. Reiss, C. Kehlet, T. Schulte-Herbr
"uggen, and S.J. Glaser. Optimal control of coupled spin dynamics: design of nmr pulse sequences by gradient ascent algorithms. *Journal of Magnetic Resonance*, 172(2):296–305, 2005. 13, 14

[KS67] S. Kochen and E.P. Specker. The problem of hidden variables in quantum mechanics. *Journal of Mathematics and Mechanics*, 17(1):59–87, 1967. 36

[KZG+09] G. Kirchmair, F. Zähringer, R. Gerritsma, M. Kleinmann, O. Gühne, A. Cabello, R. Blatt, and CF Roos. State-independent experimental test of quantum contextuality. *Nature*, 460(7254):494–497, 2009. 36

[Laf08] M. Laforest. *Error characterization and quantum control benchmarking in liquid state NMR using quantum information processing techniques*. PhD thesis, University of Waterloo, 2008. 14

[LBF98] N. Linden, H. Barjat, and R. Freeman. An implementation of the Deutsch-Jozsa algorithm on a three-qubit NMR quantum computer. *Chemical Physics Letters*, 296(1-2):61–67, OCT 30 1998. 2

[LCNV01] R. Laflamme, D.G. Cory, C. Negrevergne, and L. Viola. Nmr quantum information processing and entanglement. *Arxiv preprint quant-ph/0110029*, 2001. 1

[Lev01] M. H. Levitt. *Spin Dynamics: Basics of Nuclear Magnetic Resonance*. John Wiley and Sons Ltd, New-York, 2001. 6

[LKC+02] R. Laflamme, E. Knill, DG Cory, EM Fortunato, T. Havel, C. Miquel, R. Martinez, C. Negrevergne, G. Ortiz, MA Pravia, et al. Introduction to nmr quantum information processing. *Arxiv preprint quant-ph/0207172*, 2002. 2

[LSB+07] M. Laforest, D. Simon, J. Baugh, M. Ditty, and R. Laflamme. Using error correction to determine the noise model. *Physical Review A*, 75(012331), 2007. 2

[LVZ+99] D. Leung, L. Vandersypen, X. Zhou, M. Sherwood, C. Yannoni, M. Kubinec, and I. Chuang. Experimental realization of a two-bit phase damping quantum code. *Physical Review A*, 60(3):1924–1943, 1999. 2, 22

[Mer90] N.D. Mermin. Simple unified form for the major no-hidden-variables theorems. *Physical Review Letters*, 65(27):3373–3376, 1990. 38

[Mer93] N. David Mermin. Hidden variables and the two theorems of john bell. *Reviews of Modern Physics*, 65(3):803, July 1993. Copyright (C) 2008 The American Physical Society; Please report any problems to prola@aps.org. 36

[Mer99] N.D. Mermin. A kochen-specker theorem for imprecisely specified measurement. 1999. 36

[Mey99] D.A. Meyer. Finite precision measurement nullifies the kochen-specker theorem. *Physical Review Letters*, 83(19):3751–3754, 1999. 36

[MK93] RC McCalley and AL Kwiram. Endor studies at 4. 2 k of the radicals in malonic acid single crystals. *Journal of physical chemistry*, 97(12):2888–2903, 1993. 10

[NBD+02] M.A. Nielsen, M.J. Bremner, J.L. Dodd, A.M. Childs, and C.M. Dawson. Universal simulation of hamiltonian dynamics for quantum systems with finite-dimensional state spaces. *Physical Review A*, 66(2):22317, 2002. 12

[NC00] M. A. Nielsen and I. L. Chuang. *Quantum Computation and Quantum Information*. Cambridge University Press, Cambridge, UK, 2000. 21

[NMR+06] C. Negrevergne, TS Mahesh, C. A. Ryan, M. Ditty, F. Cyr-Racine, W. Power, N. Boulant, T. F. Havel, D. G. Cory, and R. Laflamme. Benchmarking quantum control methods on a 12-qubit system. *Physical Review Letters*, 96(17), MAY 5 2006. 2

[NSO+05] C. Negrevergne, R. Somma, G. Ortiz, E. Knill, and R. Laflamme. Liquid-state NMR simulations of quantum many-body problems. *Physical Review A*, 71(3, Part A), MAR 2005. 2

[Per90] A. Peres. Incompatible results of quantum measurements. *Physics Letters A*, 151:107–108, 1990. 38

[Pou05] D. Poulin. Stabilizer formalism for operator quantum error correction. *Physical review letters*, 95(23):230504, 2005. 23

[RLBL05] C. A. Ryan, M. Laforest, J.-C. Boileau, and R. Laflamme. Experimental implementation of discrete time quantum random walk on an nmr quantum information processor. *Physical Review A*, 72:062312, 2005. 2

[RNL+08] CA Ryan, C. Negrevergne, M. Laforest, E. Knill, and R. Laflamme. Liquid-state nuclear magnetic resonance as a testbed for developing quantum control methods. *Physical Review A*, 78(1):12328, 2008. 50

[Rya09] C. A. Ryan. *Characterization and Control in Large Hilbert Spaces*. PhD thesis, University of Waterloo, 2009. 14, 17, 50

[Sch96] Benjamin Schumacher. Sending entanglement through noisy quantum channels. *Physical Review A*, 54(4):2614–2628, Oct 1996. 68

[SCS+00] Y. Sharf, D. G. Cory, S. S. Somaroo, T. F. Havel, E. Knill, R. Laflamme, and W. H. Zurek. A study of quantum error correction by geometric algebra and liquid-state NMR spectroscopy. *Molecular Physics*, 98(17):1347–1363, SEP 2000. 2

[Shi02] Y. Shi. Both toffoli and controlled-not need little help to do universal quantum computation. *Arxiv preprint quant-ph/0205115*, 2002. 22

[Sho94] P. W. Shor. Algorithms for quantum computation: Discrete logarithms and factoring. In *Proceedings of the 35th Annual Symposium on the Foundations of Computer Science*, pages 124–134, Los Alamitos, CA, 1994. IEEE Computer Society. 1

[Sho95] P.W. Shor. Scheme for reducing decoherence in quantum computer memory. *Physical review A*, 52(4):2493–2496, 1995. 21, 22, 23

[Sil08] M. Silva. *Suppression and characterization of decoherence in practical quantum information processing devices*. PhD thesis, University of Waterloo, 2008. 16

[Spe60] E. Specker. Die logik nicht gleichzeitig entscheidbarer aussagen. *Dialectica*, 14(2-3):239–246, 1960. 36

[Ste96] A. M. Steane. Error correcting codes in quantum theory. *Physical Review Letters*, 77:793, 1996. 21

[STH+99] S. Somaroo, C.-H. Tseng, T. F. Havel, R. Laflamme, and D. G. Cory. Quantum simulations on a quantum computer. *Physical Review Letters*, 82:5381–5384, 1999. 2

[SŻWZ00] C. Simon, M. Żukowski, H. Weinfurter, and A. Zeilinger. Feasible "kochen-specker" experiment with single particles. *Physical Review Letters*, 85(9):1783–1786, 2000. 36

[TFRH80] J. Tegenfeldt, H. Feucht, G. Ruschitzka, and U. Haeberlen. 1h and 13c nuclear magnetic shielding tensors in solid pyromellitic acid dihydrate and malonic acid. *Journal of Magnetic Resonance*, 39(3):509–520, 1980. 8, 10

[TSS+00] C.-H. Tseng, S. Somaroo, Y. Sharf, E. Knill, R. Laflamme, T. F. Havel, and D. G. Cory. Quantum simulation of a three-body interaction Hamiltonian on an NMR quantum computer. *Physical Review A*, 61:012302, 2000. 2

[VC05] LMK Vandersypen and IL Chuang. Nmr techniques for quantum control and computation. *Reviews of Modern Physics*, 76(4):1037–1069, 2005. 2

[Vee84] W. S. Veeman. Carbon-13 chemical shift anisotropy. *Progress in Nuclear Magnetic Resonance Spectroscopy*, 16:193–235, 1984. 7, 8, 10

[VSB+01] L. M. K. Vandersypen, M. Steffen, G. Breyta, C. S. Yannoni, M. H. Sherwood, and I. L. Chuang. Experimental realization of Shor's quantum factoring algorithm using nuclear magnetic resonance. *Nature*, 414(6866):883–887, DEC 20 2001. 2

[WLC01] Y. S. Weinstein, S. Lloyd, and D. G. Cory. Implementation of the quantum fourier transform. *Physical Review Letters*, 86:1889, 2001. 2

[ZLD+04] J. F. Zhang, G. L. Long, Z. W. Deng, W. Z. Liu, and Z. H. Lu. Nuclear magnetic resonance implementation of a quantum clock synchronization algorithm. *Physical Review A*, 70(6), DEC 2004. 2

[ZLSD02] J. F. Zhang, Z. H. Lu, L. Shan, and Z. W. Deng. Realization of generalized quantum searching using nuclear magnetic resonance. *Physical Review A*, 65(3), MAR 2002. 2